STUDY OF OXIDE SURFACES USING TIME OF FLIGHT POSITRON ANNIHILATION INDUCED AUGER ELECTRON SPECTROSCOPY

by

MANORI PRASADIKA NADESALINGAM

Presented to the Faculty of the Graduate School of

The University of Texas at Arlington in Partial Fulfillment

of the Requirements

for the Degree of

DOCTOR OF PHILOSOPHY

THE UNIVERSITY OF TEXAS AT ARLINGTON

May 2007

ACKNOWLEDGEMENTS

I would like to express my deepest gratitude to those who have helped and encouraged me to complete work that described in this dissertation.

First and foremost, I would like to convey my sincere gratitude and appreciation to my research supervisor Dr. Alex H. Weiss for giving me the guidance, understanding patience and most importantly friendship during my graduate studies at the University of Texas at Arlington. He has helped to shape who I am as a researcher and a teacher.

My sincere gratitude goes to Dr. John H. Fry for offering me unfailing support to continue my studies. I also thank Dr. James Horwitz, Dr. Ali Koymen, Dr. Nail Fazleev and Dr. Qiming Zhang and all the faculty members for their comments and suggestions. They helped me to shape up my knowledge in various ways.

I am truly thankful to our collaborator Dr. Krishnan Rajeshwar for his advice, unconditional support and encouragement during this research work. I also appreciate Dr. C. Chenthamarakshan and Dr. Norma Tacconi for their comments, suggestion and guiding me through the rough periods.

Surviving this experience without my colleagues would have been impossible. I greatly appreciate Shuping Xie, Jinggang Zhu, Saurabh Mukherjee, Brian Davis R. Sundaramoorthy and my friends. The moment we shared together, laughter we had, I will definitely remember them as some of the most beautiful times in my life.

Much of construction and maintenance of the electronic and mechanical equipments used in this research work were the result of hard work performed by Doug Coyne, Wallace Luttes, and Jimmy Hanhart. I appreciate their tremendous support. I owe a special note of gratitude to Margie Jackymack, Jean Hanlon Amy Osborne, Victor Reece and Fran Smith for their supports and encouragement during my life at UTA.

Finally I would like to thank my family. I wish to express my sincere gratitude to my parents for giving me the spirit of never quitting or giving up, to see things through regardless of the obstacle. I am grateful to my three sisters who made all the difference even though I am so far away from home.

I hope this dissertation reflects the best of knowledge, support, courage and love you all have given me.

April 12, 2007

ABSTRACT

STUDY OF OXIDE SURFACES USING TIME OF FLIGH POSITRON ANNIHILATION INDUCED AUGER ELECTRON SPECTROSCOPY

Publication No. _____

Manori Prasadika Nadesalingam, PhD.

The University of Texas at Arlington, 2007

Supervising Professor: Alex H. Weiss

Transition metal oxides (TMOs) exhibit a rich collection of interesting and intriguing properties which can be used for wide variety of applications. In this dissertation, I will discuss the first PAES measurements on vacuum anneal induced changes in the surface layers of Cu_2O/ Ta, Cu_2O/TCO and oxidized Cu(100) prepared by spray coated, electrochemically deposition and thermal oxidation techniques respectively. PAES measurements on Cu_2O/TCO shows that the a very large increase in the intensity of the Cu ($M_{2,3}$ VV) Auger peak after annealing at 250 ^{0}C. Similar but significantly smaller changes were observed in the EAES spectra consistent with the fact that PAES is primarily sensitive to the top-most atomic layer due to the fact that the

positrons are trapped just outside the surface prior to annihilation while EAES samples several atomic layers. While PAES measurements on oxidized Cu(100) show a large monotonic increase in the intensity of the annihilation induced Cu ($M_{2,3}$ VV) Auger peak as the sample is subjected to a series of isochronal anneals in vacuum up to annealing temperature 300 ^{0}C. The intensity then decreases monotonically as the annealing temperature is increase to ~500 ^{0}C. These results provide a clear demonstration of the thermal reduction of the copper oxide surface after annealing at 300 ^{0}C followed by re-oxidation of the copper surface at the higher annealing temperatures presumably due to the diffusion of subsurface oxygen to the surface.

TABLE OF CONTENTS

LIST OF ILLUSTRATIONS

LIST OF TABLES

CHAPTER 1

INTRODUCTION

1.1 Overview

An increasing amount of attention has been paid to the metal oxides due to their many current and possible future applications. Most of the transition metal oxides are being used in the industry of microelectronic applications, solar cell energy production and photodiodes [1-10], sensors and as catalysts.[11,12] A major breakthrough in the study of transition metal oxide occurred in early 70s when Fujishima and Honda reported that titanium dioxide (TiO_2) could be used as a catalytic electrode in a photo-electrolysis cell to decompose water into H_2 and O_2 without applying a external voltage.[11,13] Extensive research has been focusing on oxides of copper (Cu) after the promising results of the study of photoelectric properties of single crystal copper(I) oxide (Cu_2O) by Pollack and Trivich in 1975.[13] As we are experiencing dwindling fossil fuel resources the solar energy development is much needed today. The high absorption coefficient in the visible region of solar spectrum, the abundance of constituent of material and non toxicity are key points for researchers to investigate of copper(I) oxide. The properties the Cu_2O surface has been the subject of numerous studies using X-ray Photoelectron Spectroscopy[14] (XPS), X-ray induced Auger electron spectroscopy[15] (XAES),

Ultraviolet Photoemission Spectroscopy (UPS), Auger Electron Spectroscopy (AES), and X-ray Diffraction (XRD).[16] The goal of this dissertation is to study the top most layer of different type of copper oxide thin films using Time of Flight Positron annihilation induce Auger Electron Spectroscopy (TOF-PAES) and the Electron induced Auger Electron Spectroscopy (EAES). To further understand the growth of oxide layer on the Cu(100) substrate has been investigated.

The TOF-PAES studies presented in this thesis were able to provide unique information on the top most atomic layer of the Cu_2O and oxidized Cu(100) surfaces due to the topmost layer sensitivity of PAES. It should be noted that while Electron Auger electron spectroscopy and X ray induced photoelectron spectroscopies are widely used as surface analysis techniques to provide quantitative details about the elements on top layers of the materials, the relatively high energy of the incident beam used in these techniques limits the surface selectivity to a minimum of 3-10 atomic layers, resulting in a large secondary electron background and can damage the surface of the sample. Positron annihilation induced Auger electron spectroscopy (PAES) is capable of selectively probing the top layer of the surface due to the fact that the core hole excitations which give rise to Auger electron emission result from the annihilation of positrons that are trapped at the surface (for example, detailed calculations indicate that 95% of the PAES signal originates from the topmost atomic layer). Because the core holes are created through annihilation rather than collision the incident positron beam energy can be selected to be small in the range of few eV s.[17] The low incident beam

energy limits surface damage and eliminates the large secondary electron background associated with electron and photon excited Auger Electron emission.

1.2 Positron trapping at the surface

The positron is the anti particle of the electron. The positron has the same mass as an electron, spin (1/2) and a positive charge. The positron was postulated by P.A.M. Dirac in 1929 and first observed by C. Anderson in 1932.[18]

Positron spectroscopy has been used as an effective tool for studying the electronic structure of metallic materials and alloys.[17,19] The main positron techniques used in bulk studies includes: Positron lifetime measurements, measurements of the Doppler broadening gamma spectra and Angular correlation of annihilation radiation (ACAR). The first two techniques are used primarily to study open volume defects in materials, while ACAR is used primarily to study the electronic structure of materials. Based on low energy positron interaction with target surface, probing techniques can be summarized as shown in figure 1.1. In order to interpret the experimental results from these systems it is essential to understand the electron-positron interaction at the surface. When positron interacts with target surface, a number of interesting phenomena take place.

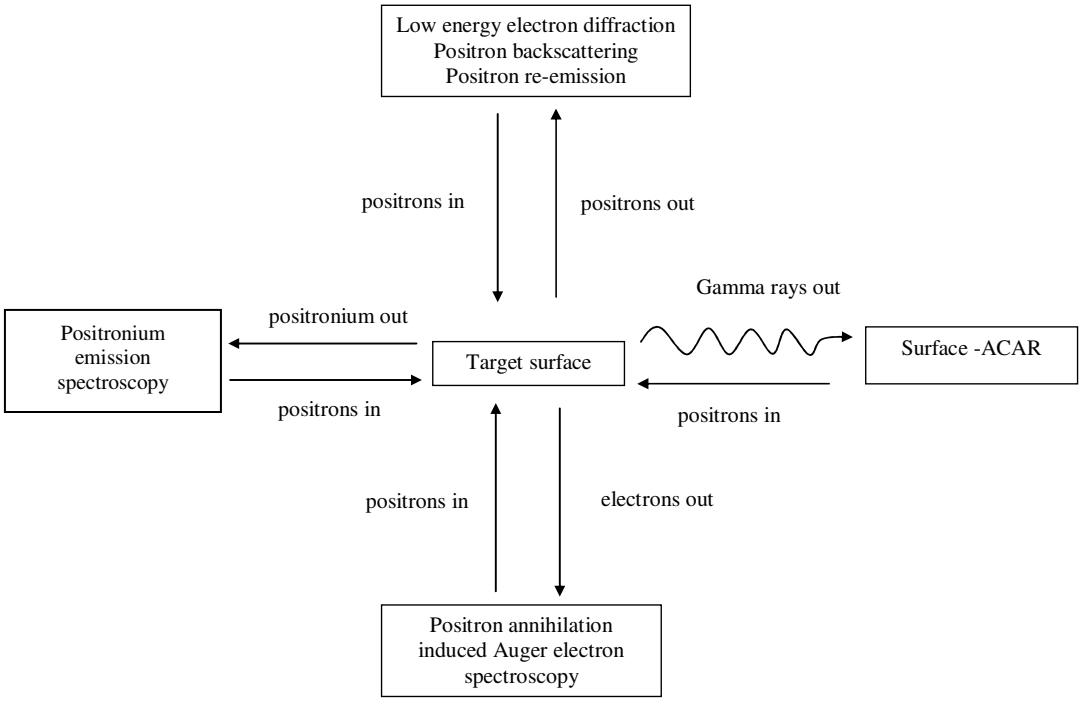

Figure 1.1 Positron surface spectroscopies.[17]

The main processes[19,20] are positron reemission into the vacuum in cases where the surface has a negative work function, positronium (Ps) formation and emission and positron trapping into a surface state. The positron interaction at the surfaces of materials is illustrated in figure 1.2. The initial process of scattering of the incident positrons, energy loss via core excitation and secondary electron production are shown in figure 1.2 (a). A few percent of the incident positrons elastically scatter from the outermost atomic layers. This is the mechanism which gives rise to low energy

diffraction. Figure 1.2 (b) shows positrons penetrating into the surface and losing energy via the production of plasmas, electron-hole pairs and phonons. Positron also can pick up an electron to form a non-thermal Ps or be reemitted as a free positron (the positron reemission spectroscopy) before they come into thermal equilibrium. Some thermalized positrons annihilate with electrons in bulk and create two gamma rays of about 511keV are shown in figure 1.2 (c). In addition to that the thermalized positrons and Ps can be released to vacuum. Finally figure 1.2 (d) shows a process that is important in understanding the surface selectivity of positron annihilation –induced Auger electron spectroscopy. Thermalized positrons become trapped in an image correlation well at the surface and annihilate with electrons and emit two gamma rays. Some thermalized positrons can be thermally desorbed. The trapped positron with an electron leaves the surface as a Ps a process that competes with annihilation in the surface state.

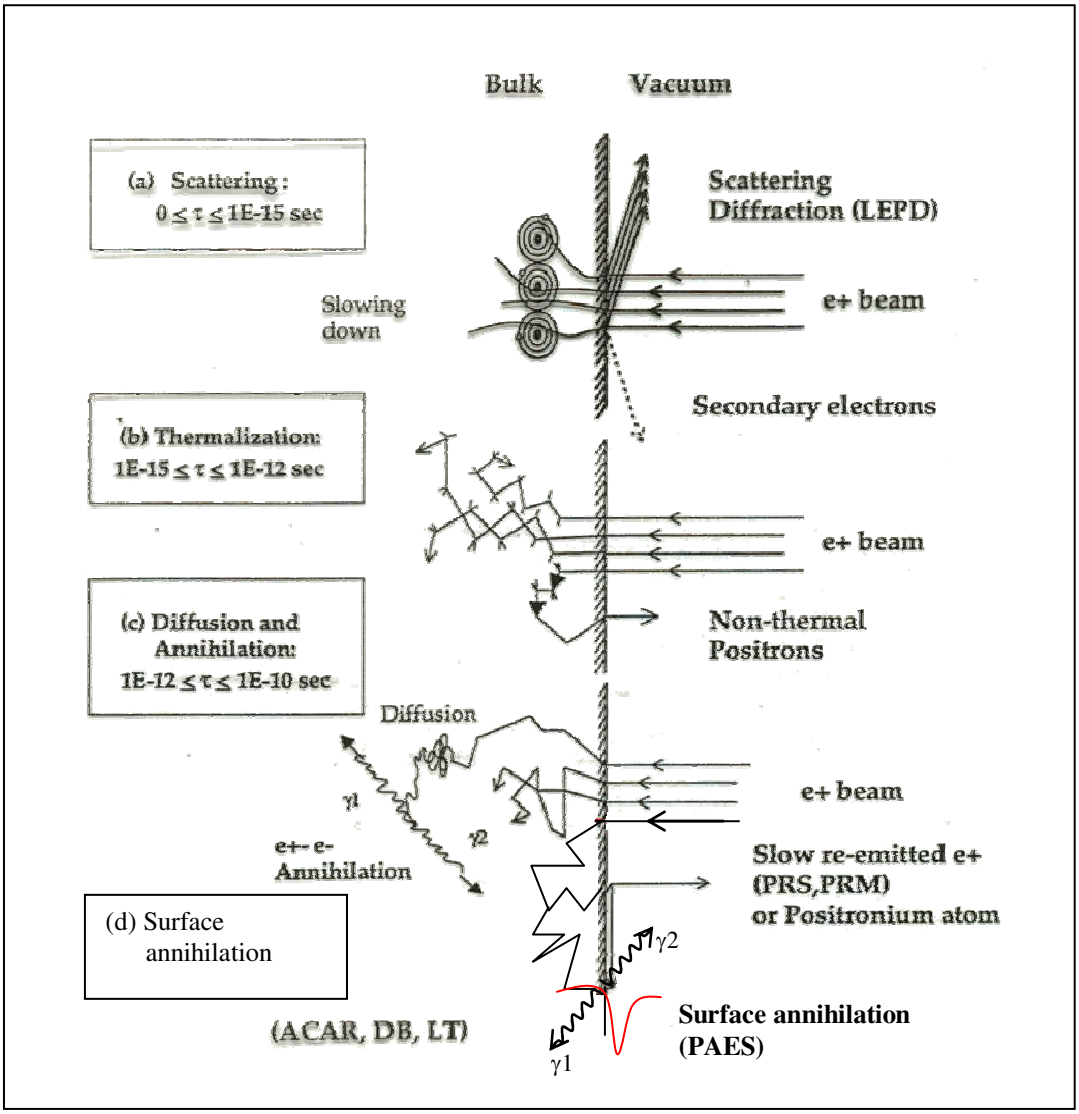

Figure 1.2 Positron interactions at the surface of materials.[19]

1.3 Auger electron spectroscopy

1.3.1 Electron induced Auger electron mechanism

Conventional methods of Auger electron spectroscopy make use of energetic electron or photons to create the core – hole excitation that result in the Auger signal. In electron induced Auger electron spectroscopy (EAES), the core level electrons are ionized through an impact process using a relatively high energy incoming electron beam. Typically the incident electron energy is set at three or more times larger than the binding energy of the core level that leads to Auger electron emission. Figure 1.3 illustrates the steps of electron induced Auger electron emission with energy level diagram of oxygen (O) atom. First, a core level electron is removed by electron impact, leaving the atom in an excited state as shown in figure 1.3 (a). The atom relaxes by filling the core hole with an electron from a less tightly bound orbital is shown in figure 1.3 (b). In this state, an electron from the L_1 sub shell fills a K shell core-hole. The energy corresponding to the difference between the binding energies of these two levels transferred to an electron in the $L_{2,3}$ sub shell causing it to leave the atom. This outgoing electron is labeled as Auger electron. The Auger process is represented symbolically by naming the shells in which vacancies occur, in both the initial and final state. For the transition of figure 2.1, the nomenclature is "Auger $KL_1L_{2,3}$ transition". Therefore, the kinetic energy $E_{KL_1L_{2,3}}$ of the Auger electron is given by,[17]

$$E_{KL_1L_{2,3}} = E_K - E_{L_1} - E_{L_{2,3}} - \phi \qquad 1.1$$

The energies E_K, E_{L_1} and $E_{L_{2,3}}$ are the binding energies of the involved electrons

Although the EAES is used widely for materials analysis it has some limitations.

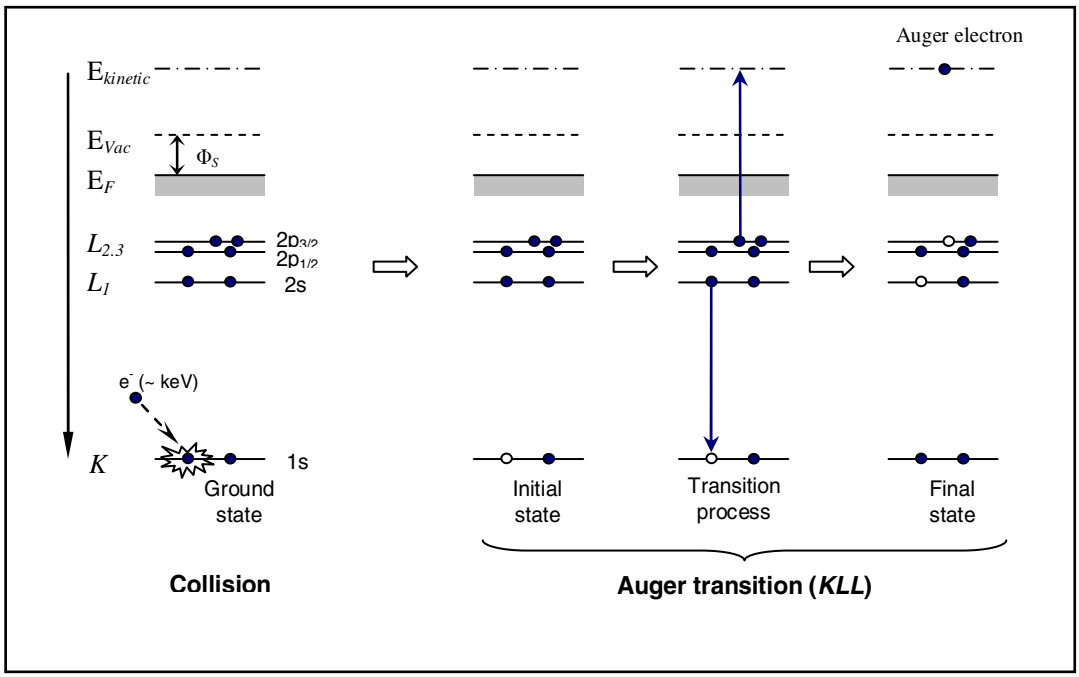

Figure 1.3 Electron induced Auger electron process with energy diagram.

1.3.2. Positron annihilation induced Auger mechanism (PAES)

In PAES, a low energy positron beam (<25 eV) is used to create core holes via the matter anti-matter annihilation process.[21-24] The Figure 1.4 shows the PAES mechanism. During this process positrons with low energy are implanted into the material. The implanted positrons slow down through a variety of inelastic processes and then diffuse to the surface and are trapped in surface state with high efficiency. While in the surface state, the positron may annihilate with an electron or pick up an electron and be thermally desorbed from the surface as positronium.

As the core holes are created by matter-antimatter annihilation and not impact ionization, the large secondary electron that occur in conventional AES can be eliminated by using an incident beam energy that is below the energy of the Auger

electron. Secondary electrons cannot be produced through impact ionization with energies larger than the kinetic energy due to conservation law of energy.

$$KE_{sec} \leq E_k = E_p - \phi^+ + \phi^- \qquad 1.2$$

Where KE_{sec} is the kinetic energy of the secondary electrons as it leaves the surface in equation (1.2), E_k is the kinetic energy of auger electrons and ϕ^+, ϕ^- are the work functions of the positron and electron respectively.

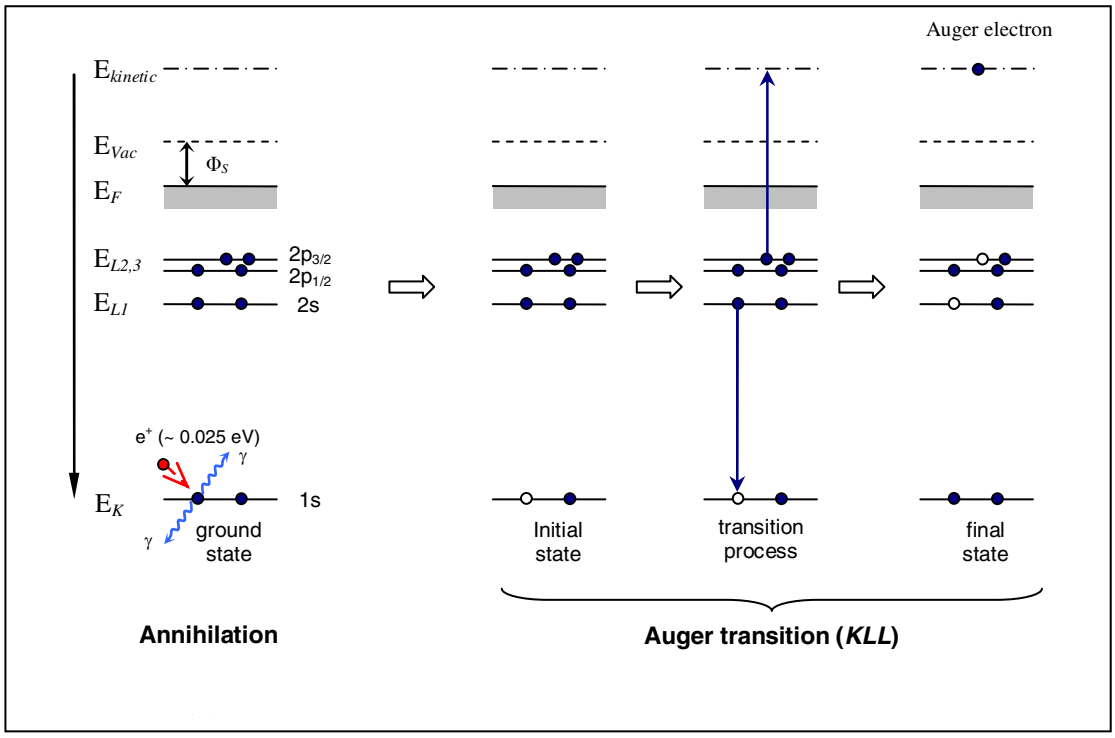

Figure 1.4 Positron annihilation induced Auger electron process with energy diagram.

1.4 Positron interaction with metals and alloys

Hodges and Scott[25] were the first to suggest the possibility of the trapping positrons in the potential well at the metal surface. The behavior of positron at the surface of a metal[26] is discussed in terms of three contributions to the positron work function for the metal, namely the positron zero point energy, the positron-electron correlation energy and the surface dipole barrier. Figure 1.5 provides a schematic representation of trapping of low positrons in the surface state of a metal.

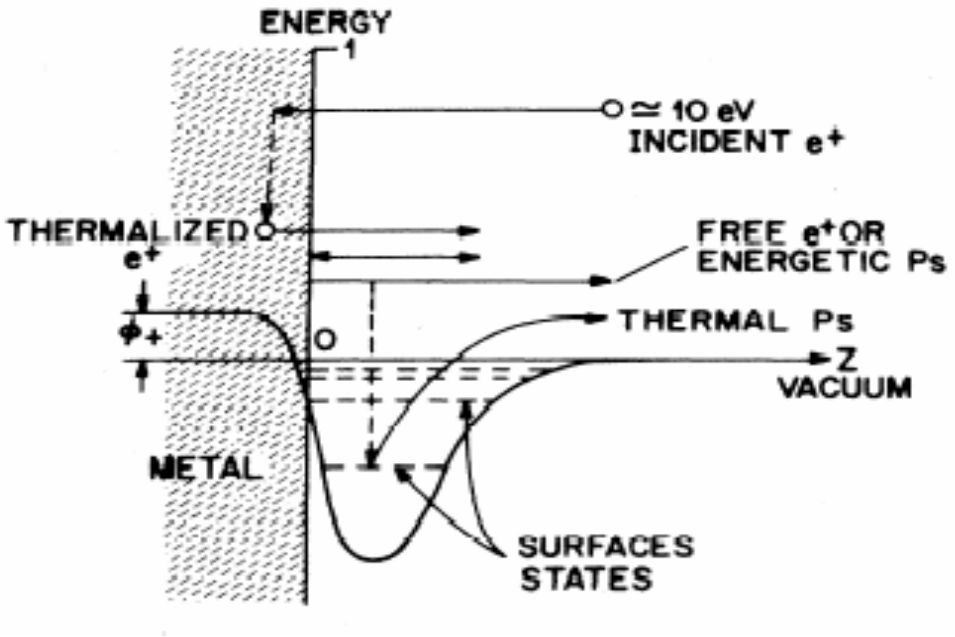

Figure 1.5 Schematic representation of some of the process that occur when slow positrons are near surface.[19]

Slow positrons incident on a metal surface quickly lose their kinetic energy various scattering process. Some of the positrons annihilate with electrons in the bulk crystal if implanted at energies at larger than 1 keV. Most of the positrons diffuse to the surface and encounter a surface dipole layer due to spilling out of electrons into the

vacuum just out side the surface. The dipole provides a potential step that lowers the energy of electrons as they enter the bulk, but raises the energy of the oppositely charged positrons. This makes it possible for positrons to have a negative work function on some surfaces. Outside the surface positron sees an attractive potential-well due to an image potential at large distance from the metal surface and electron correlation at small distances. The theoretical calculations of the surface potential and positron wave function are very useful in understanding the interaction of positrons with atoms at the surface. The potential ($V^+(r)$) due to the surface felt by a positron can be written as follows.[27,28,29]

$$V^+(r) = V_H(r) + V_{corr}(r) \qquad 1.3$$

where $V_H(r)$ is an electrostatic Hartree (Coulomb), and $V_{corr}(r)$ is a correlation component of the positron potential. The Hartree potential $V_H(r)$ was constructed as a superposition of the atomic Coulomb potentials $V_{coulomb}^{atom}(|r-R|)$ from all atoms located within predetermined radius of the evaluation point, where R is the position of the host nuclei. The correlation potential $V_{corr}(r)$ part outside the metal surface is expressed as an image potential,

$$V_{image}(r) = -\frac{e^2}{4\pi\varepsilon_0}\frac{1}{4[Z_{eff}(n(r)) - Z_0]} \qquad 1.4$$

Where e is the charge of positron, ε_0 is the vacuum permittivity, $Z_{eff}(n(r))$ is the effective distance from the surface represented as a function of the total electron density at the surface $n(r)$ and Z_0 defines the effective image-plane position on the vacuum

side of the top layer of atoms. If there is an absorbate on the metal surface or the substrate is a semiconductor the image potential is modified as follows,[28]

$$V_{image}(r) = -\frac{(\varepsilon - 1)}{4(\varepsilon + 1)} \frac{1}{[Z_{eff}(n(r)) - Z_0]} \qquad 1.5$$

Where ε is the dielectric constant of the adsobate (semiconductor).

Figure 1.6 shows the surface potential and the ground state wave function of the positron. Figure 1.6 (a) is the potential seen by the positron at a Cu (100) surface. The origin at the Z-axis is the center of the first layer. Inside the surface, the potential is calculated using the local density approximation. Outside the surface, the surface potential is determined using the local density approximation that reproduces the classical image potential at large distances. Figure 1.6 (b) is the wave function of the trapped positrons in a metal. The wave function has an appreciable overlap only with the first layer of the Cu. The implanted positrons diffuse back to the surface and are trapped in the potential well just outside the topmost layer. As a consequence, the trapped positrons that annihilate with core electrons do so almost exclusively associate with core electrons in the top most atomic layer. The PAES Auger signal that results from these annihilations is characteristic of the top most atomic layer with extremely high surface selectivity.

The specific core annihilation probability rate which gives the fraction of positron annihilation per second with core level electrons of quantum numbers n= 1,2,3,…. and *l*=s,p,d, can be calculated using equation (1.6) and it is based on the independent

particle model (IPM). In the IPM, it is assumed that the electrons are left unperturbed by the presence of positron or that the positron is a independent particle.

$$\lambda_{n,l} = \pi r_0^2 c \int dr^3 \left|\Psi_+(r)\right|^2 \left(\sum \left|\Psi_{n,l}^i(r)\right|^2 \right) \qquad 1.6$$

Where r_0 is the classical electron radius, c is the velocity of light, Ψ_+ is the positron wave function and $\Psi_{n,l}^i$ denotes core electron wave function described by the quantum number n and l.

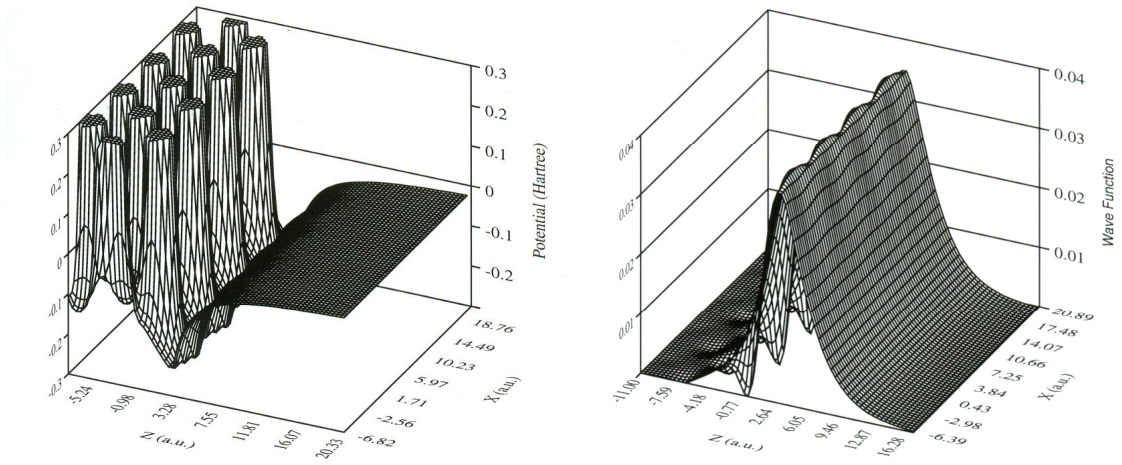

(a) (b)

Figure 1.6 Positron surface state: (a) positron potential (b) positron wave function on the Cu (100)surface (Fazleev et. al.).

The total annihilation rate λ of the surface trapped positrons is calculated by using equation (1.7). In this calculation positron –electron correlation effect is much more significant for valance electrons.

$$\lambda = \frac{\pi r_0^2 c}{e} \int d^3 r n^+(r) n(r) \Gamma(n(r)) \qquad 1.7$$

where $n^+(r)$ is the positron charge density, $n(r)$ is the electron density, and the $\Gamma(n(r))$ is the annihilation enhancement factor in an electron gas of density $n(r)$. The enhancement factor takes account of fact that the electrons are attracted toward the positively charged positron, thus increasing the overlap of the positron and core electron wave functions and annihilation rate. Considering the total annihilation rate (λ) of surface trapped positrons and the positron annihilation rate $(\lambda_{n,l})$ with specific core-electron shell described by quantum numbers n and l, the core annihilation probabilities $(p_{n,l})$ can be calculated by equation (1.8).

$$p_{n,l} = \frac{\lambda_{n,l}}{\lambda} \qquad 1.8$$

1.5 Positronium emission

Other processes that compete with the trapping of positrons into the surface state include positron reemission and positronium emission. Positronium (Ps) is atomic bound state of an electron and a positron, like a hydrogen atom. Martin Deutsch first observed Ps experimentally in 1948. The binding energy of Ps is 6.8 eV, which is equal to the half of the energy of the 1 s state of hydrogen atom. When the spin direction of positron is anti-parallel (in a singlet state) to the spin of electron in the Ps, annihilation takes place predominantly by two gamma rays. On the contrary, if the spin direction of positron is parallel to the electron in the Ps (triplet state), annihilation associates with three gamma rays. Ps formation occurs only at the surface of metals and semiconductors

as screening reduces the strength of coulombs interaction between electron-positron in the bulk. Ps is formed in two ways at the metal surface: (1) the positron picks up an electron and escape from the surface without getting trapped in a surface state (called a direct process). (2) the positron is first trapped in a surface state and is subsequently desorbed at elevated temperature as a bound electron-positron pair (positronium) if sufficient energy is available from thermal fluctuation. The Ps desorption or activation energy E_a [30] is given by the following equation,

$$E_a = E_b + \phi - \tfrac{1}{2} R_y \qquad 1.9$$

where the binding energy of positron in the surface state is $E_b > 0$, ϕ is the electron wave function of the surface and R_y is the Rydberg energy or hydrogen binding energy (~13.6 eV).

CHAPTER 2

EXPERIMENTAL DETAILS OF TOF-PAES SPECTROSCOPY

2.1 Overview

Figure 2.1 shows a schematic diagram of the Time of Flight Positron Annihilation induced Auger Electron Spectroscopy (TOF-PAES).[31] The TOF-PAES system consists of a beam transportation chamber with a Na-22 radioactive source, a sample preparation chamber and the time of flight electronic signal measurement system. Positron source part, beam transportation chamber and sample preparation chamber can be isolated by UHV gate valves.

2.2 Positron beam production and beam path

A sodium (Na-22) is used as a positron source in our lab due to its long life time (2 ½ years and the reasonable price). The radioactivity of the Na-22 source was ~ 6.88 mCi as of the end of year 2005. The positron emission rate of Na-22 is 2.546 x10^8 e^+/s (3.7 x 10^7 x 6.88). Following is the equation of radioactive decay of Na-22 isotope.

$$^{22}_{11}Na \rightarrow {}^{22}_{10}Ne + \beta^+ + \upsilon \qquad 2.1$$

Where β^+ represents a positron and υ represents a neutrino. The positrons emitted from the Na-22 source have a wide range of energy with a full width of a 545 keV with

peak energy of a 178 keV. These fast moving positrons must be slowed down in order to obtain a mono-energetic slow positron beam. In our beam positrons are moderated using a 1 μm thick and a 9 mm diameter polycrystalline tungsten foil (W). The radioactive source (Na-22) is mounted with a stainless steel disk and electrically isolated from a tungsten plug by a Macor insulator. A 0.25 mm thin film of Cu on the source was used to make the electrical contact with the moderator. Figure 2.2 shows a schematic of Na-22 source holder.

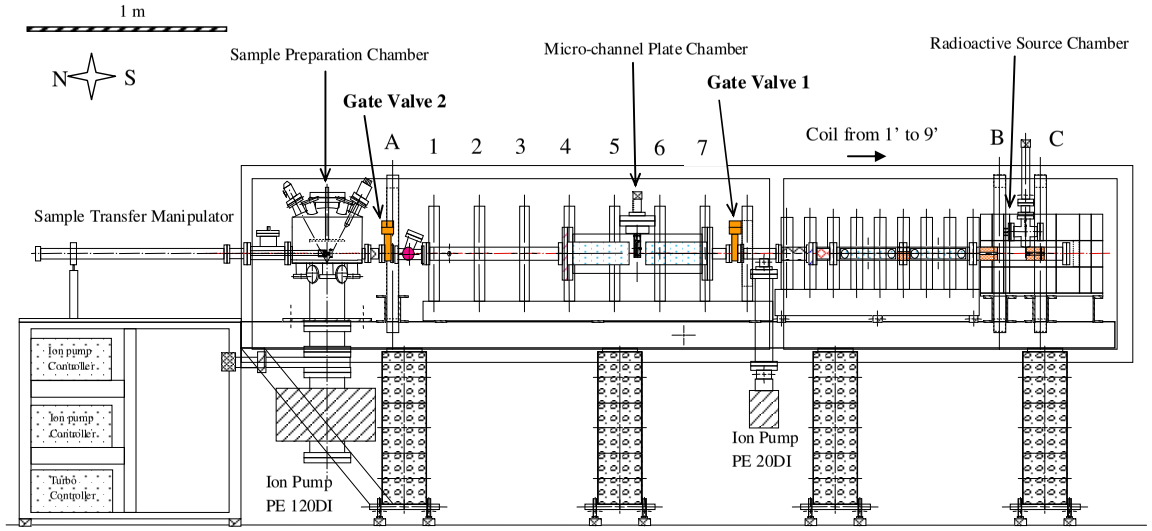

Figure 2.1 Schematic side view of high resolution time of flight positron annihilation induced Auger electron spectroscopy (TOF-PAES) at UTA.[31]

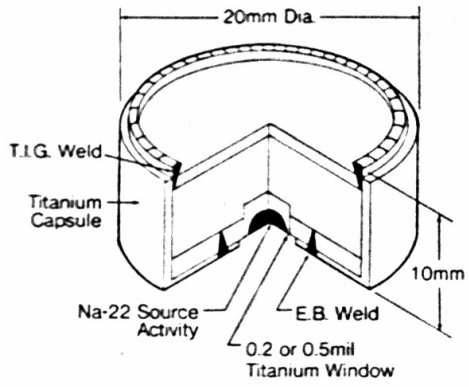

Figure 2.2 Na-22 source capsule. [31]

When the high energy positrons are implanted into the moderator, most of the positrons (~87%) are transmitted through the moderator foil with a high residual energy known as fast positrons. A very small fraction (~13%) of positrons is slowed down and thermalized. Positrons close to the surface undergo diffusion back to the surface. A fraction of the positrons thermaliz and diffuse to the surface and are emitted into the vacuum as free positrons due to the negative work function of Tungsten (W). The energy of outgoing free positrons is determined by the work function (ϕ^+) of the W. The efficiency of the moderator depends on several factors such as geometric configuration of the moderator, the fraction of positrons arriving at the emitting surface and the probability of the positrons emitting from the surface. The reason of using

tungsten as a moderator is due to its reasonable efficiency, highly negative positron work function and its cleanliness over time.

The slow positrons coming out of the tungsten moderator are extracted by a grounded grid in front of the moderator and accelerated by ExB fields to the target area. In our TOF-PAES system the transmission type moderator has been using and the moderator efficiency (ε) is in the range of ~10^{-5} to 10^{-4}. The kinetic energy of the incident beam hitting sample is determined following equation.

$$KE_{e^+ onsample} = e(V_{\mathrm{mod}\,erator} - V_{sample}) + \phi^+ \qquad 2.2$$

$V_{\mathrm{mod}\,erator}$, and V_{sample} are bias voltages on the moderator, and on the sample respectively. ϕ^+ is the work function of the positron at the sample surface and e is the charge of the electron.

In front of the moderator there are four E x B plates and two more tungsten barriers as shown in figure 2.3. The first two E x B plates (labeled A and B) filter only slow positrons and fast positrons do not have drift through the plates. Each set of E x B plates consists of a pairs of parallel rectangular stainless steel plates. An approximately constant electric field is normal to the axial magnetic field produced by a set of coils. The slow positrons are deflected upward through the first set of E x B plates (A) and downward through the second set of E x B plates (B).

After passing through the first two E x B plates, slow positrons may be accelerated by the parallel plate accelerator. In the accelerator slow positrons are accelerated (depending on potential) by means of a uniform electric field. The accelerator is a nine-stage, with 5 MΩ UHV resistors (purchased from KDI electronics)

placed between consecutive stages to provide a uniformly decreasing potential. Each stage is made of stainless steel circular disks with a ¾ inch hole in the center to allow the passage of slow positrons. One side of accelerator is connected with source tube and set at adjustable voltage V_{acc}, while the other side is grounded with MCP chamber. There are another two sets of E x B plates (C and D) sitting in front of the parallel plate accelerator and the MCP is in between these two sets of E x B plates. These two E x B plates deflect the beam path below the MCP which is blocking the central axis of the beam tube. The E x B deflection plates "C" will deflect the positron beam down and let it pass by the MCP and plates "D" deflect the beam back to normal beam line axis. The deflection plates "D" guide the Auger and secondary electrons to the MCP. The applied potential to the E x B plates must be lower and it must be adjusted carefully as it will cause an additional spread in the flight time of detected electrons.

Table 2.1 Potential on E x B plates

E x B Plate	Applied Voltage (V)	
A	$V_{AE} = 0$	$V_{AW} = +21.3$
B	$V_{BE} = 0$	$V_{BW} = -70.0$
C	$V_{CE} = +8.8$	$V_{CW} = -8.8$
D	$V_{DE} = -8.8$	$V_{DW} = +8.8$

There are two sets of rectangular helmholtz in the TOF-PAES system. One set covers the slow positron beam path and sample preparation region and other covers the

source chamber region. These two sets of rectangular helmholtz coils compensate for the earth magnetic field. The current of the each coil is adjusted in order to maximize the positron beam flux. The axial magnetic field is generated by several circular shapes helmholtz coils. This magnetic field guides positron beam from source to the target. Table 2.2 shows the parameters of helmholtz coil used to maintain axial magnetic field through the coils as of end of year 2005.

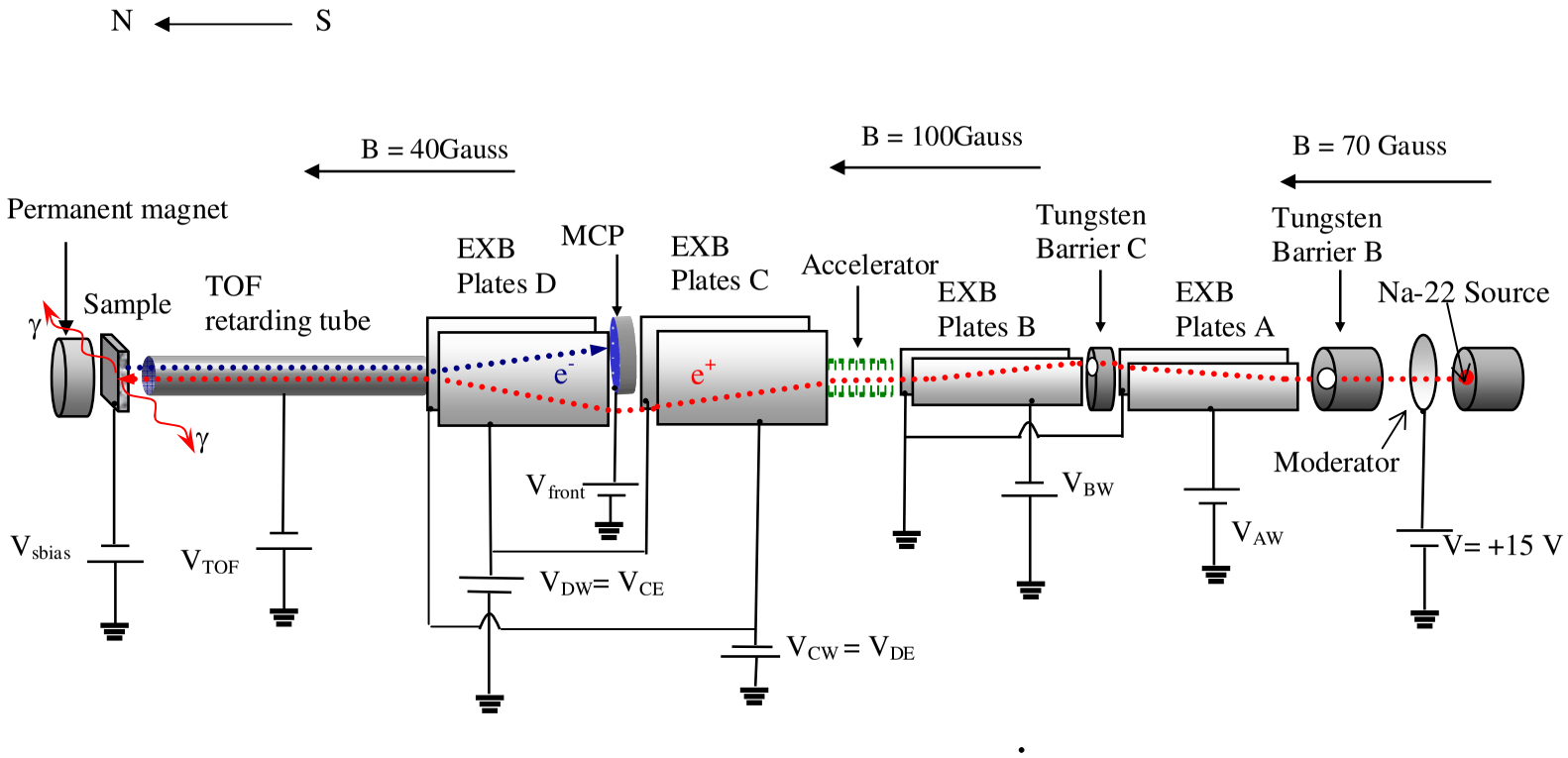

Figure 2.3 Schematic diagram of positron and Auger electron beam path.

Table 2.2 Parameters of coils that maintain axial magnetic field in positron beam path.

Coil group index	Name of the coil	Inside Diameter (inch)	Number of turns	Current going through the wire (A)	Voltage (V)	Magnetic field (Gauss)
1	A	20	363	5.00	13.08	40
2	1	10	226	3.00	2.53	40
	2	10	226	3.00	2.59	40
	3	10	226	3.00	2.10	40
	4	10	226	3.00	2.51	40
	5	10	226	3.00	2.33	40
	6	10	226	3.00	2.76	40
	7	10	226	3.00	2.54	40
	8	10	226	3.00	2.48	40
3	1`	4.5	320	3.00	3.46	100
	2`	4.5	320	3.00	3.46	100
	3`	4.5	320	3.00	3.45	100
	4`	4.5	320	3.00	3.44	100
	5`	4.5	320	3.00	3.45	100
	6`	4.5	320	3.00	3.46	100
	7`	4.5	320	3.00	3.46	100
	8`	4.5	320	3.00	3.46	100
	9`	4.5	320	3.00	3.49	100
4	B	20	159	12.00	15.14	70
4`	C	20	510	7.00	27.4	70

2.2.1 Gamma ray shielding

As discussed in the section 2.2, Na_{11}^{22} isotope is transformed to Ne_{10}^{22} by two competing mechanism: positron emission and electron (K) capture followed by emission of 1.275 MeV gamma rays (photon). According to the decay scheme of Na_{11}^{22} as shown in figure 2.4, positron are emitted in 89.8 % of transformation while the competing decay mode electron capture occurs in 10.06% of the nuclear transformation. Each emitted positron annihilates with electron and emits two gamma rays with energy

of 0.511MeV. These gamma rays are emitted with an angle of 180^0 from each other. These high energetic photons emitted from radionuclide present the most common external hazard in laboratories.

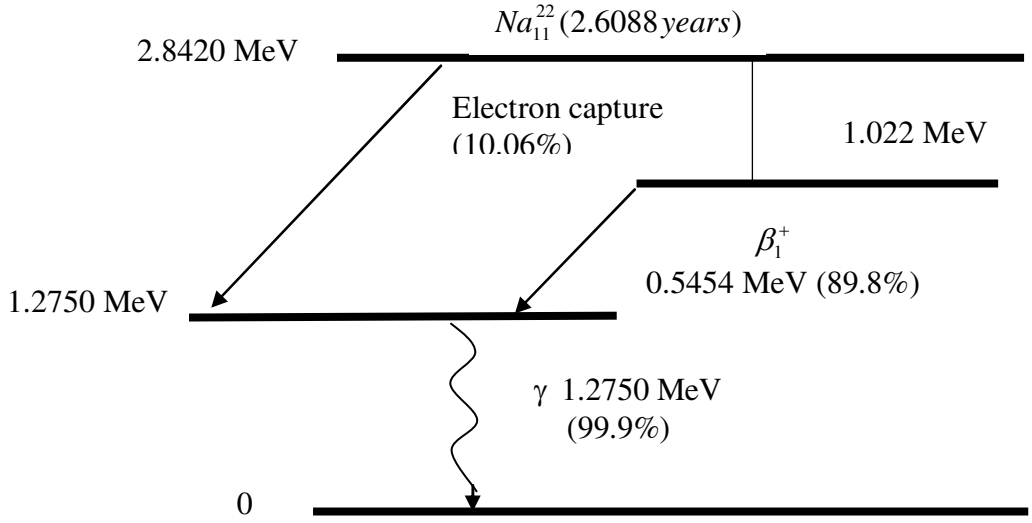

Figure 2.4 Na_{11}^{22} radionuclide decay scheme.[33]

The practical way to reduce the radiation intensity exposure to personnel would be putting a shield between the source and personnel. The best material to shield photon would be lead bricks. There is no threshold exposure rate which is considered to be safe and unrestricted. However the exposure rate of 2.5 mrem/hr is considered to be the legal limit for people. The thickness of the lead bricks that places around the Na_{11}^{22} isotope can be calculated by following equation,

$$I = I_0 e^{-\mu x} \qquad 2.3$$

I is the exposure rate at a distance with a shield and I_0 is the exposure rate without a shield. μ and x represent linear attenuation coefficient and thickness of the shielding material respectively.

The exposure rate I_0 due to the point source with a certain radioactivity can be calculated by,

$$I_0 = \frac{6CEn}{d^2} \qquad 2.4$$

In equation 2.4, C is strength of the source in Curie (Ci) and En is gamma ray energy in MeV. Number of gamma rays per disintegration and distance from the source in feet are represented by n and d respectively. The 90% of two-gamma rays are emitted with energy of 0.511MeV and 100% of 1-gamma rays are emitted with energy of 1.275MeV per disintegration of Na-22 source. The strength of Na-22 source is 100 mCi and the distance (d) from the source is 1 foot.

Hence,

$$En = [(2*0.511*90\%) + (1*1.275*100\%)] \qquad 2.5$$

Where C= 0.1 Ci , d = 1'

$$I_0 = I_{0.511MeV} + I_{1.27MeV}$$

$$= \frac{6*0.1*[(2*0.511*90\%) + (1*1.275*100\%)]}{1^2} = (551.88 + 765)mR \qquad 2.6$$

Using the equation (2.7) the thickness of the lead bricks is calculated with linear attenuation coefficients[33] of lead for 0.511 MeV and 1.275 MeV are 1.8319 cm^{-1}, 0.6669 cm^{-1} respectively.

$$x = \frac{\ln(I_0 / I)}{\mu} \qquad 2.7$$

For 0.511 MeV gamma rays

$$x = \frac{\ln(551.88/2.5)}{1.8319} = 2.946\,\text{cm} \qquad 2.8$$

For 1.275 MeV gamma rays

$$x = \frac{\ln(765/2.5)}{0.6669} = 8.5823\,\text{cm}. \qquad 2.9$$

In our PAES system, we have lead bricks with thickness of 4.5 inch that are placed around the Na source capsule for shielding gamma rays in all direction. Besides the lead bricks around the source capsule, there are two tungsten collimator barriers in front of the Na source and a tungsten plug behind the Na source. They block the gamma rays in backward and forward direction respectively.

2.2.2. Time-Of-Flight retarding tube

The TOF retarding tube is consists of two concentric, stainless steel cylindrical tubes. The diameter of the inner cylinder is 1 inch, diameter of the outer cylinder is 2 inch and both are 0.7 meter in length. The outer cylinder is a part of the vacuum chamber. The inner cylinder is isolated from the grounded outer cylinder and a nearly uniform retarding potential can be established over the length of the tube by applying a bias voltage to the inner cylinder. The data in this dissertation were acquired with -17V bias voltage on the inner cylinder. The minimum and maximum voltage that can be applied to the inner cylinder is ± 1000 V. When positrons enter the TOF tube, they are

accelerated at the entrance due to negative bias voltage of the TOF tube and they travel with constant speed through the field free central region. Electrons emitted from the sample are decelerated at the entrance of the TOF tube due to the negative bias voltage of the tube relative to the sample. Electrons maintain a constant speed inside the tube. They recover their initial speed when they leave the TOF tube and enter the chamber moving through the E x B plates (D). If electrons do not have enough kinetic energy to overcome the potential barrier they cannot pass through the TOF tube to the electron detector (MCP). In order for electrons to pass through the TOF tube the maximum kinetic energy of electrons in the region of the grounded vacuum tube in front of the TOF tube must exceed the energy eV_{TOF} where V_{TOF} is the negative bias voltage of the TOF tube. In the PAES measurements reported in this dissertation, positrons impact the grounded sample surface at 15eV by maintaining moderator bias and source tube voltage at 15 V and 0 V respectively. Thus the impact induces secondary electrons leave the sample with energies less than or equal to 15 eV. The -17 V bias on the TOF tube prevents all impact induces secondary background electrons from reaching the detectors. The prevention of the large number of secondary electrons reaching the detector greatly reduces the electron detector counting rate and thereby reduces the accidental background under the Auger spectrum. A uniform accidental background presents in the time of flight Auger electron spectrum is proportional to $N_\gamma N_{e^-} \Delta t$. Where count rate of gamma rays is N_γ, N_{e^-} is the count rate of Auger electrons and Δt is the duration of time.

2.3 Detection system

There are two types of detectors used in our TOF-PAES. A Micro-channel plate is used to detect charge particles such as positrons, electrons and Gamma ray detectors are used to Gamma radiation after positron –electron annihilation.

2.3.1 Gamma ray detectors

The gamma rays are detected by a Barium Fluoride (BaF_2) and a Sodium Iodide (NaI) with Thallium (TI) scintillation detector. These two detectors are mounted on either side of the sample as shown in figure 2.5. When a γ-ray enters a BaF_2 or a NaI (TI) crystal it delivers energy either through the photoelectric effect or a fraction through Compton effect of its energy to electrons of the crystal[33]. These energetic electrons excite the atoms in the crystal causing the crystal to scintillate and emit photons which have low energy comparing to incident photon on the crystal. These emitted photons strike the photocathode of the photomultiplier caused it to eject photo electrons. The number of electron ejected from the photocathode is proportional to the energy of the absorbed photons.

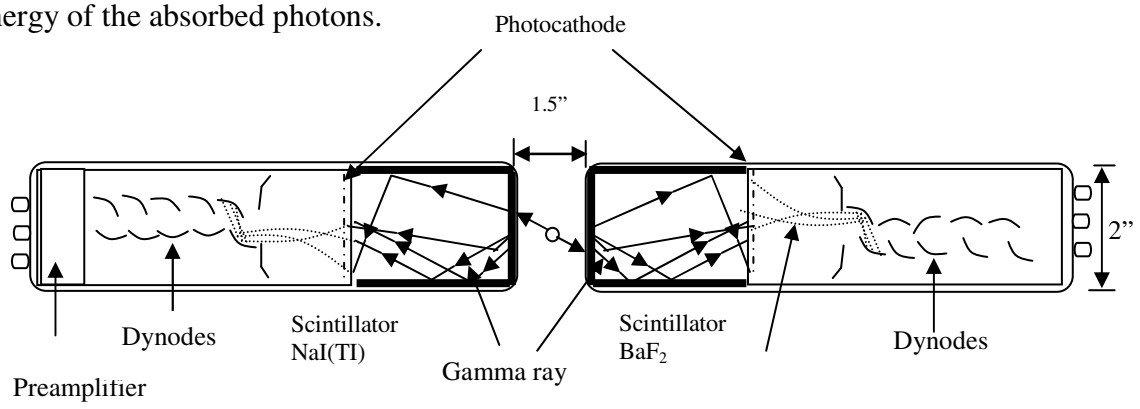

Figure 2.5 Basic arrangement of gamma ray detectors

These photo electrons are accelerated on to the first dynode where they are multiplied by means of secondary electron emission. The multiplied secondary electrons emitted from the last dynode are collected by the anode. The Output pulse height of photomultiplier tube depends on the supply voltage to dynodes even though the input gamma ray energy is a constant. It means that the total gain (G) of the photomultiplier tube is related to the supply voltage of the dynode as shown in equation (2.10) .In this equation the secondary electron emission ratio (δ) is considered to be a constant.[35]

$$G = \alpha\delta^{n} \qquad 2.10$$

Where the number of dynodes in the photomultiplier is tube is n and α is the proportionality constant.

The typical shape of the output of BaF_2 detector anode is a negative pulse with rising time is around ~1.8 ns corresponding to the time to go from 10% to 90% of peak height. A Bertran power supply is used to provide the operation voltage (-2500 V) for the photomultiplier tube of the BaF_2 detector. NaI crystals have a high efficiency and focus energy resolution relative to other scintillation detectors for detecting gamma rays as it have high density and Z (Z=53) value. In our system NaI detector is used to measure the positron intensity. Figure 2.6 shows the electronic circuit of NaI gamma ray detector system.

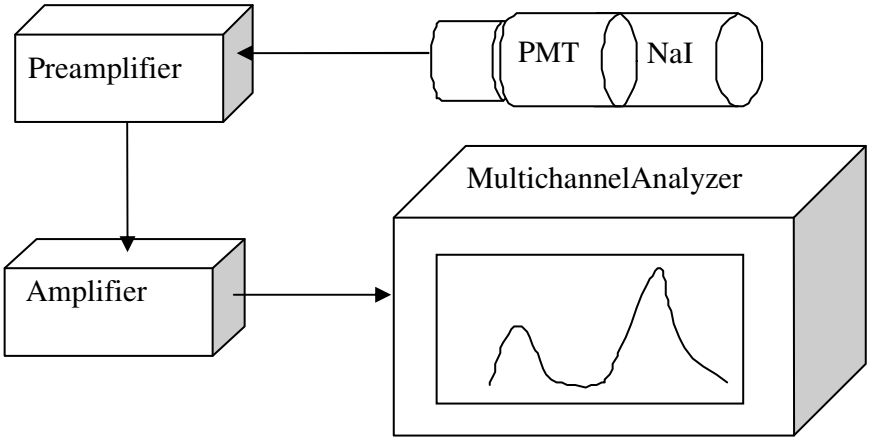

Figure 2.6 Electronic circuit used with NaI gamma ray detector.

2.3.2 Microchannel plate

Microchannel plate (MCP) is an array of 10^4-10^7 miniature electrons multiplier tubes (channels) oriented parallel to one another and made from lead glass. Each channel acts like an electron multiplier. In order to maximize the secondary electron emission the inner wall of each tube is coated with a semi conducting material. The cross section of a micro-channel plate is as shown in figure 2.7. A large potential difference across the MCP causes electrons to move from one side to the other side. The one side of MCP which is facing the sample is held at a positive voltage (+220 V) and the opposite side is held at a positive voltage (+2200 V). The Auger electron enters a channel and emits an electron from the channel wall. This secondary electron accelerates through the channel starting from the side which has lower potential while bouncing from the wall of the channel several times.[36] During their trajectory they strike on the inner wall of the channel and emit more secondary electrons. As this process is

repeated many times during their acceleration due to the potential different of the opposite sides of the channels the single input electron generate ~10^8 electrons at the output. These output electrons are collected by the MCP anode which has voltage of +2460 V.

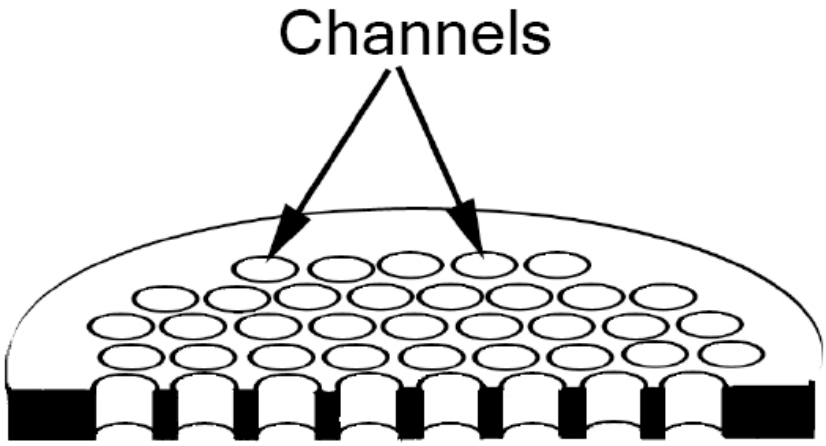

Figure 2.7 Schematic view of cross section of Microchannel Plate (MCP).[36]

2.4 Time-Of-Flight (TOF) acquisition system

After positron and electron annihilation in the sample, gamma rays and Auger electrons release from the sample surface into vacuum. The gamma rays are detected by the BaF_2 fast scintillation detector. The output pulse of the BaF_2 is fed to the fast preamplifier. Then the output pulse from the fast preamplifier is fed to the constant fraction discriminator (CFD, Canberra 2126). It is delayed by 700 ns (t_{delay}) when it passes through the delay generator (416A). The output pulse of the delay generator is considered as the stop signal of the TOF coincidence measurement.

The outgoing Auger electron from the sample drifts through the TOF retarding tube and it is detected by the micro-channel plate (MCP). The magnetic field due to a magnet behind the sample parallelize outgoing Auger electrons from the sample and it also helps to reduce the energy dispersion of Auger electrons from the axis of the TOF tube. Figure 2.8 shows the trajectories of electrons in an inhomogeneous magnetic field. The electrons are moving from the region of strong magnetic field to weaker magnetic field. The weaker magnetic field (B_a)can be calculated as shown in equation (2.11) by considering conservation of angular momentum if electron experiences negligible motion during the one revolution.[37]

$$B_a = B_s\left(\frac{\sin\theta_a}{\sin\theta_s}\right)^2 \qquad 2.11$$

Where B_s represents strong magnetic field, electron emitted with initial angle θ_s with respect to the horizontal axis (z) of the TOF tube and electron reach the analyzer with final angle θ_a. The incident Auger electrons on the anode of the MCP stimulate fast negative pulse which has a response time less than 1 ns on the cathode of the MCP and it will be the input signal to the preamplifier. The output pulse of the preamplifier goes through the second constant fraction discriminator. The output signal of the CFD is the start signal for the TOF coincidence measurement. The time interval between start and stop signal is fed to the time to amplitude converter (TAC, Ortec 437A) and it generates analog input pulse.

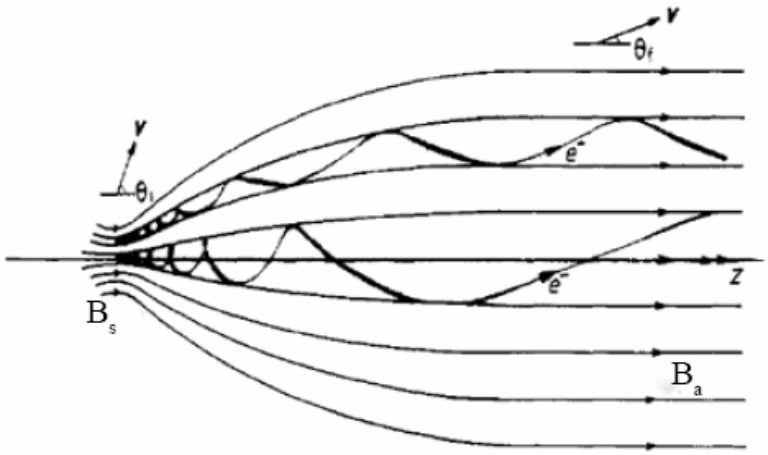

Figure 2.8 Illustration of parallelization of electrons in an inhomogeneous magnetic field going from region of strong field to weak field.[37]

The block diagram of TOF acquisition system is as shown in figure 2.9. The analog output pulse height distributions in the TAC, which is directly related to the flight time of each and every Auger electron is fed to the multi channel analyzer (MCA, Ortec, TRUMP/2K). Multi Channel Analyzer (MCA) builds a histogram of counts depending on their pulse height (in this case pulse height corresponds to time) representing coincidence events. The reason of selecting MCP output signal as the start signal TAC is that BaF_2 counts per second are much higher than MCP counts per second. If BaF_2 signal is considered as the start signal while an extremely low counting rate of MCP is supplied to the stop input, the TAC will spend lot of time responding to the start pulses that have no associated stop pulse within the selected time range. Start with no stops will cause excessive dead time in the TAC without producing useful data. So that the reverse timing measurements contribute high efficiency of TAC counts and

low noise in the flight time spectrum of Auger electrons. Output analog pulses from the TAC go through the analog to digital converter (ADC) for digitizing the pulse and those digitized out put pulses of ADC are sorted into bins (channel) according to their pulse amplitude. These digital values are used as the address of memory location corresponding to a given channel) that is incremented. Our MCA is micro-processor controlled. Therefore flight spectrum can be stored in the computer. MASTRO software is used to collect data and analyze them. Moreover these stored data files can be converted to Microsoft Excel format. Figure 2.10 shows the time of flight spectrum obtained from the Cu (100) recorded in MCA and it is a histogram of the number of counts versus pulse height. Horizontal axis of the graph represents time and channel number and flight time is inversely is proportional to channel number. Vertical axis represents number of counts per second. In order to understand the different energy of Auger electron in the sample, timing spectra of MCA must be converted to energy spectrum.

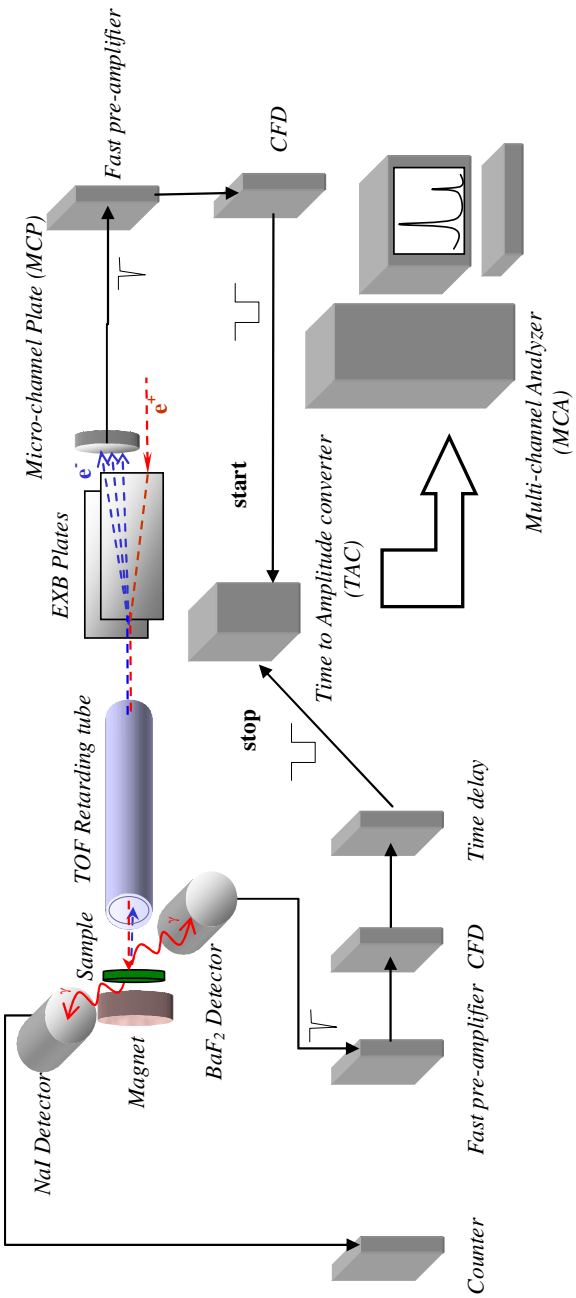

Figure 2.9 Block diagram of TOF acquisition system.[31]

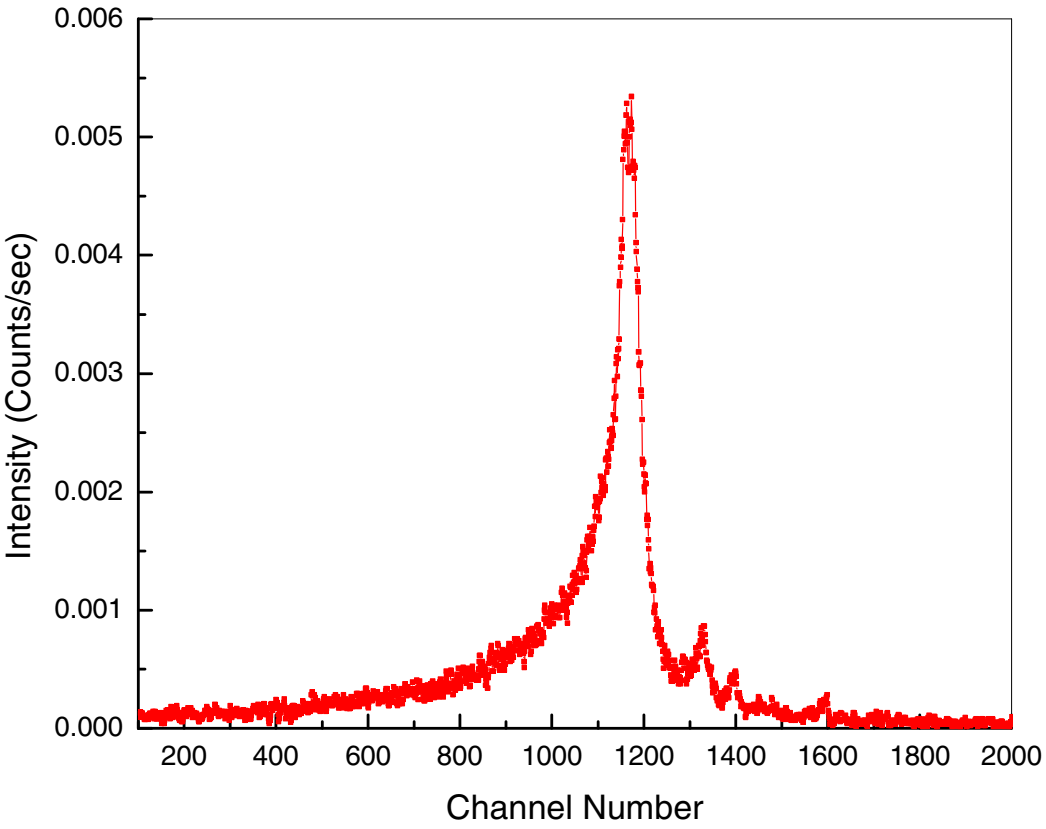

Figure 2.10 Channel/ time of flight spectrum of Cu (100).

2.4.1 Time to energy conversion

The outgoing Auger electrons from the sample encounter regions with magnetic field, no field, and electromagnetic fields in between the sample and MCP as shown in figure 2.11.

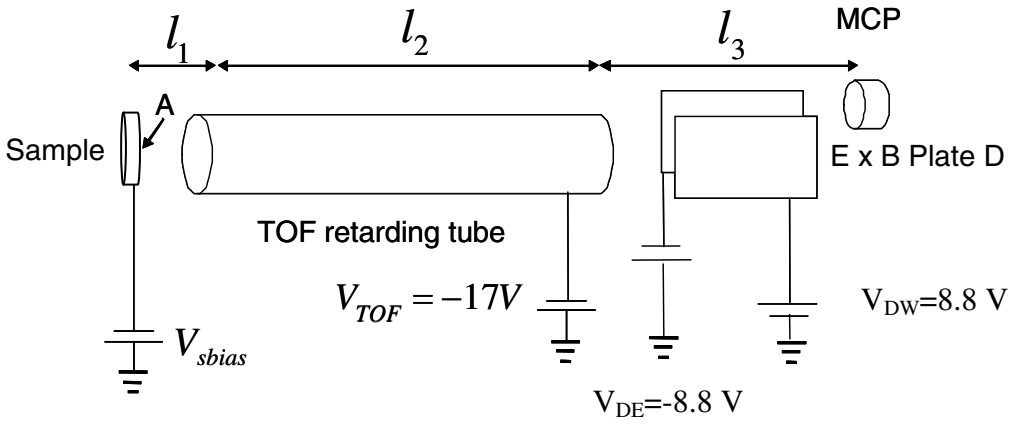

Figure 2:11 Schematic of Auger electron path from the surface of sample to the MCP.

Total time taken by the Auger electron going from the sample surface to MCP can be written by following equation.

$$t_{flight} = t_1 + t_2 + t_3 \qquad 2.12$$

Travel time of Auger electron going from sample to TOF tube is t_1, travel time of Auger electron in the TOF tube is t_2, and travel time of Auger electron from the end of TOF tube to the MCP is t_3.

$$t_{flight} = \frac{l_1}{\sqrt{\frac{2}{m}E_{Auger}}} + \frac{l_2}{\sqrt{\frac{2}{m}(E_{Auger} - eV_{TOF})}} + \frac{l_3}{\sqrt{\frac{2}{m}E_{Auger}}} \qquad 2.13$$

The distance from the sample to the TOF tube front side is l_1. The length of the TOF tube and the distance from back end of the TOF tube to the MCP are l_2 and l_3 respectively. The mass of the electron is m and the total energy of outgoing Auger electron at the sample is E_{Auger}. Here we considered there is no acceleration during Auger electron entering and leaving the TOF tube.

Following equation can be obtained after rearranging the equation 2.13,

$$t_{flight} = \frac{l_2\sqrt{m/2}}{\sqrt{(E_{Auger} - eV_{TOF})}} + \frac{(l_1 + l_3)\sqrt{m/2}}{\sqrt{E_{Auger}}} \qquad 2.14$$

Measured flight time (t_{MCA}) from spectrum of MCA according to the reverse timing method is not the true flight time (t_{flight}). The true flight time can be calculated from the following equation

$$t_{flight} = (t_{delay} - t_{MCA}) \qquad 2.15$$

Total number of channels in the MCA is 2000 and Channel number of the MCA is inversely proportional to the flight time as mention in previous section. Time range of TAC is 800 ns. Therefore the time corresponding to given channel number ($\#_{flight}$) can be calculated by the following equation;

$$t_{flight} = (t_{delay} - t_{MCA}) = \#_{flight} \times \frac{800}{2000} \qquad 2.16$$

Channel number can be calculated from equation 2.14 and 2.16,

$$\#_{flight} = \frac{2000 \times (t_{delay} - t_{MCA})}{800} = \frac{2000}{800} x \left(\frac{l_2\sqrt{m/2}}{\sqrt{E_{Auger} - eV_{TOF}}} + \frac{(l_1 + l_3)\sqrt{m/2}}{\sqrt{E_{Auger}}} \right) \qquad 2.17$$

$\#_{flight} \propto \frac{1}{\sqrt{E}}$ as m , l, total number of channel (2000) and time window of the TAC (800 ns) are constants.

If $\#_{MCA}$ corresponds to t_{MCA} and $\#_{delay}$ corresponds to t_{delay}

Then $\#_{flight} = \#_{delay} - \#_{MCA}$ 2.18

$$\#_{MCA} = \#_{delay} - \left(\frac{2000}{800} \times \left(\frac{l_2\sqrt{m/2}}{\sqrt{(E_{Auger} - eV_{TOF})}} + \frac{(l_1 + l_3)\sqrt{m/2}}{\sqrt{E_{Auger}}} \right) \right) \quad 2.19$$

By simplifying equation 2.15

$$\#_{MCA} = P_1 - \left(\frac{P_2}{\sqrt{(E_{Auger} - P_3)}} + \frac{P_4}{\sqrt{E_{Auger}}} \right) \quad 2.20$$

Where P_1 represents $\#_{delay}$, P_2 represents $(2000/800)l_2\sqrt{m/2}$, P_3 represents eV_{TOF}, and P_4 represents $(2000/800)(l_1 + l_3)\sqrt{m/2}$

The best method to find P_1, P_2, P_3 and P_4 would be to study timing spectra of positron induced secondary electrons. When positron incident on the sample surface some of electrons in the conduction band get excited. Some of excited electrons excite other electrons in the band who will be emitted into the vacuum if they have enough energy. Outgoing electrons with maximum energy are shifted ~2-3 eV higher than the sample bias. As the negative bias voltage on the sample increases, the kinetic energy of the outgoing electrons increases and the time required by the outgoing electrons to reach MCP get smaller. Electrons with maximum energy (E_{peak}) would be,

$$E_{peak} = eV_{sbias} + 2eV \quad 2.21$$

Where e is the charge of electron and V_{sbias} is the negative voltage applied to the sample. In our research applied negative bias voltage would be in the range of -20 V to -900 V. Figure 2.12 shows the coincidence counts versus channel spectra for TiO_2 on Ta sample with sample bias voltage at -900V and -50V. Considering peak channel

corresponding to the bias voltage of the sample, we can plot so called calibration curve can be plotted. Calibration curve for TiO_2 on Ta is shown in figure 2.13. The following equation 2.22 exactly matches the calibration curve.

$$E_{Auger} = \frac{P_2^2}{(P_1 - \#_{MCA})^2} + P_3 \qquad 2.22$$

The solution for E_{Auger} in terms of other parameters can be obtained by neglecting the flight time of Auger electrons in the region of magnetic field and electromagnetic field. Hence the equation (2.17) can be simplified as shown in equation (2.23).

$$\#_{MCA} = \#_{delay} - \left(\frac{(2000/800) l_2 \sqrt{m/2}}{(E_{Auger} - eV_{TOF})} \right) \qquad 2.23$$

$$\#_{MCA} = P_1 - \left(\frac{P_2}{(E_{Auger} - eV_{TOF}} \right) \qquad 2.24$$

Therefore $E_{Auger} = \frac{P_2^2}{(P_1 - \#_{MCA})^2} + P_3 \qquad 2.25$

Where P_1, P_2 and P_3 represent $\#_{delay}$,($(2000/800) l_2 \sqrt{m/2}$) and eV_{TOF} respectively. The value obtained for these parameters explains that P_2 parameter depends on the length of TOF retarding tube, P_3 depends on the TOF bias voltage and P_1 depends on the channel number corresponding to delay time. Considering calculated energy in the range of 22 eV to 600 eV gives percent error less than 1%. Calculation of energy less than 22 eV gives the percent error around~3% while energy in the range of 800 eV to 1000 eV gives percent error around~1.2%. Hence the simple equation 2.25 can be used as a calibration function.

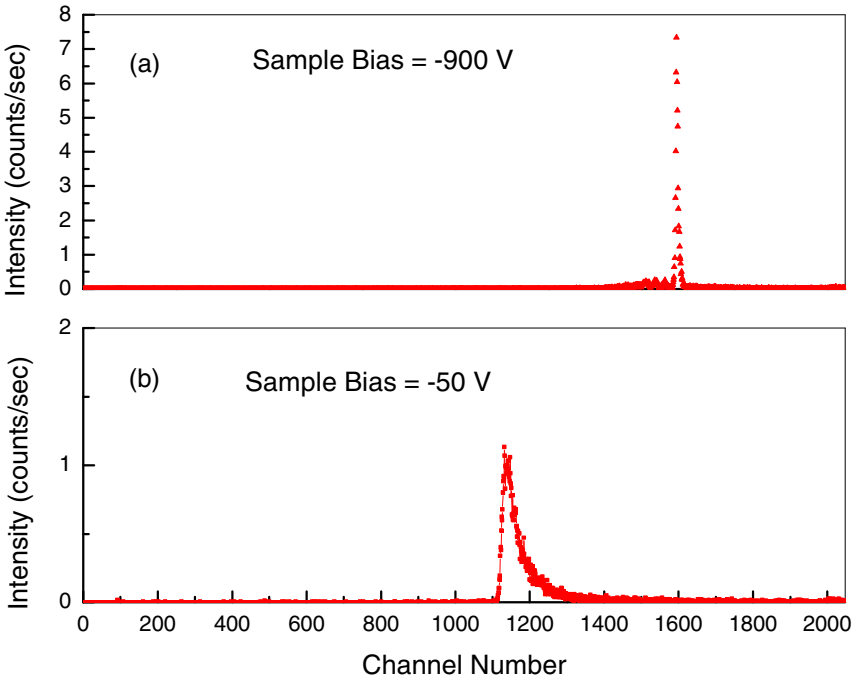

Figure 2.12 Count rate versus channel number of TiO_2 on Ta with sample bias (a) -900 V (b) -50 V.

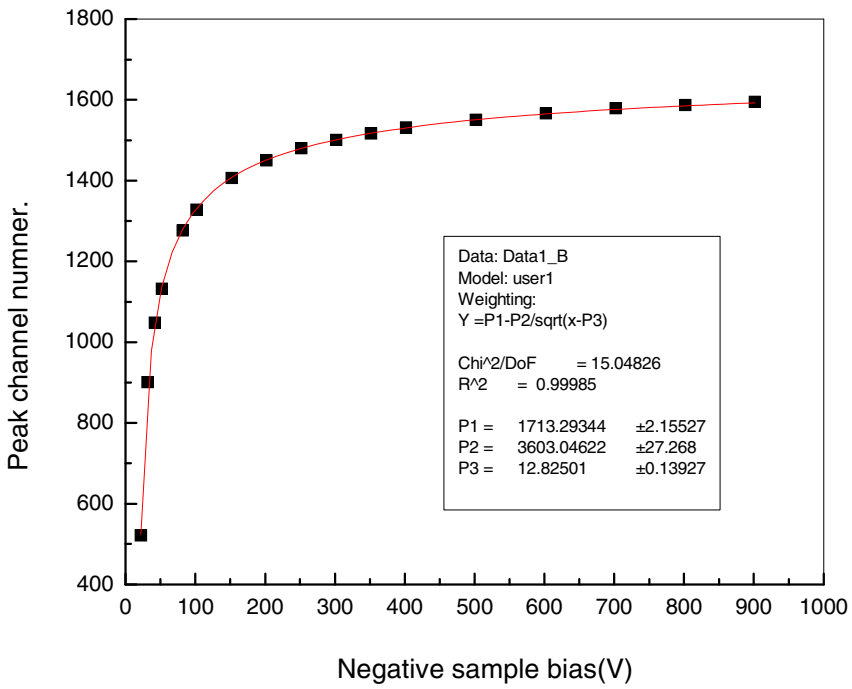

Figure 2.13 Calibration curve for TiO_2 on Ta sample.

2.5 Sample preparation chamber

Sample preparation chamber of TOF-PAES system consists of Sample holder with linear transfer shaft, High temperature UHV button (substrate) heater, sputter gun and low energy diffraction (LEED) system. Side view of sample preparation chamber is shown in figure 2.14. The sample preparation chamber is made of non magnetic stainless steel by MDC Inc. from a custom design. Chamber cylinder is 12" in diameter and 14" in height. The sample holder is attached to the tip of a linear transfer shaft both made of non magnetic stainless steel. The sample holder is electrically isolated from the linear transfer shaft using ceramic spacers. A permanent magnet (a disk with 1" in

diameter and ¼" thick) is mounted in the sample holder head. The purpose of mounting a magnet behind the sample permanently is to create a strong divergent magnetic field at the sample surface and near region. This helps to make the trajectory of electrons parallel to the time of flight retarding (TOF) tube axis. This is shown in figure 2.15. The sample bias cable is attached to the sample holder. A high temperature (~1200 ^{0}C) UHV button heater sits on the top of the cover of the magnet in a small cylinder with an opening on sample side. The small cylinder is attached to the magnet cover by rectangular shaped non magnetic stainless steel legs. The button heater is made of molybdenum (Mo) and it is 0.502 inches in diameter and 0.135 inches in thickness. Its maximum power is 60 Watts. A K type thermocouple is attached to the sample to measure the temperature. It is connected to a digital thermometer (OMEGA) to measure the surface temperature of the sample for low temperature. Temperatures higher than 400 ^{0}C were measured using an infrared thermometer (ULTIMAX, UX-10). A drawing of the sample holder and a linear transfer shaft is shown in figure 2.16.

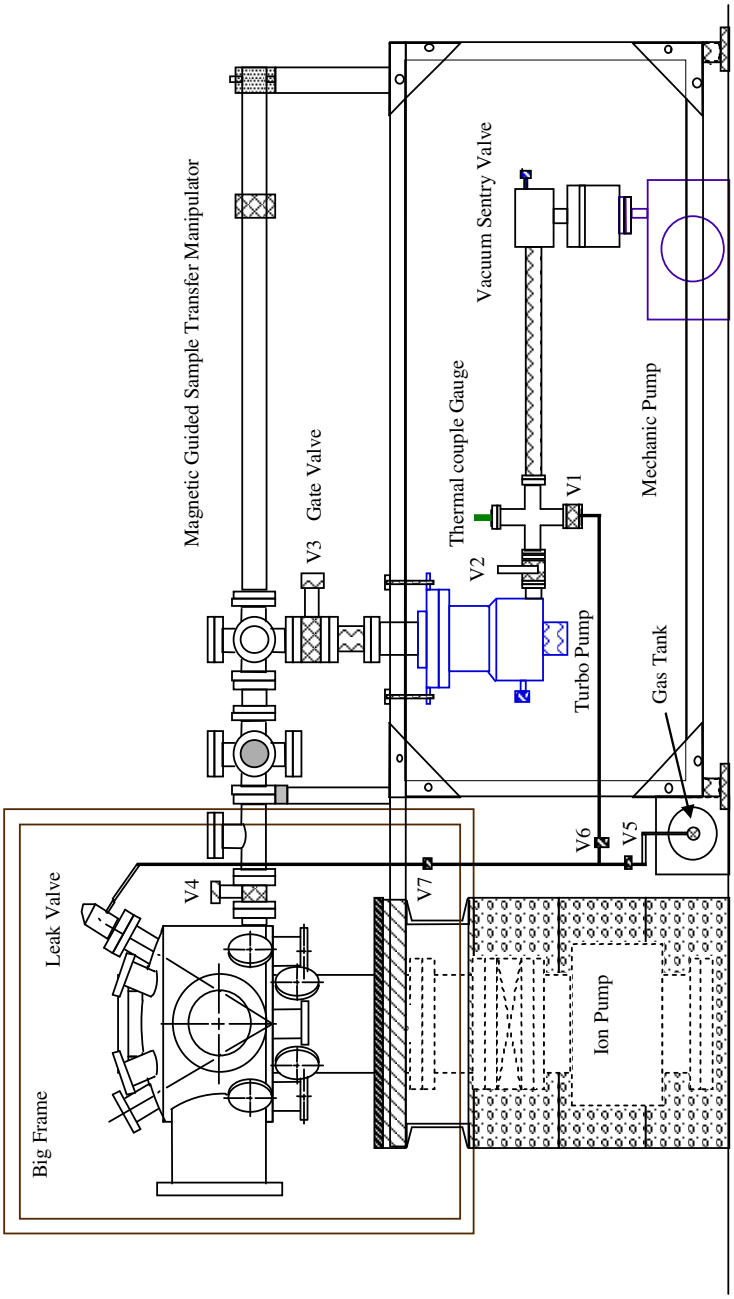

Figure 2.14 Side view of sample preparation chamber.[31]

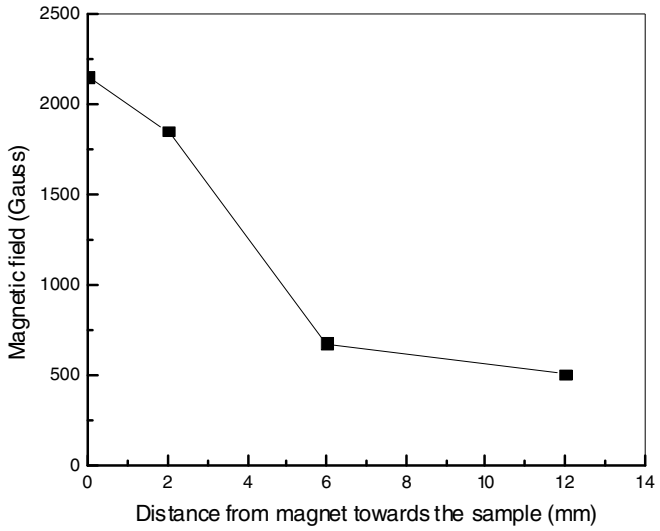

Figure 2.15 Magnetic field variations in front of the sample surface.

The UHV chamber has to be opened in order to mount a sample on to the sample holder. The pressure inside the chamber is maintained at ~10^{-10} Torr. This helps in taking data with a clean surface to achieve reliable results and to minimize significant contamination by background gases. Impurities such as carbon (C) can be removed from the sample *in-situ* using a ion sputter gun (Perkin-Elmer) in an argon (Ar) gas environment. The energy of the ion beam of the sputter gun can be varied within the range 0.5 keV to 5 keV with Ion gun control unit (Physical electronics industries, PHI model 20-115). The size of the ion beam is around 5 mm and it will be expanded up to 10x10mm area with scanning. Scanning during sputtering process helps to maintain uniform sputter rate. The surface current due to sputtering is varied from 4-10 μA depending on the material of the sample. A variable leak valve (Varian 951-5100) is

used to control the argon gas input to the chamber while sputtering. This valve can also be used to leak other gases such as O_2, N_2 and H_2 into the chamber.

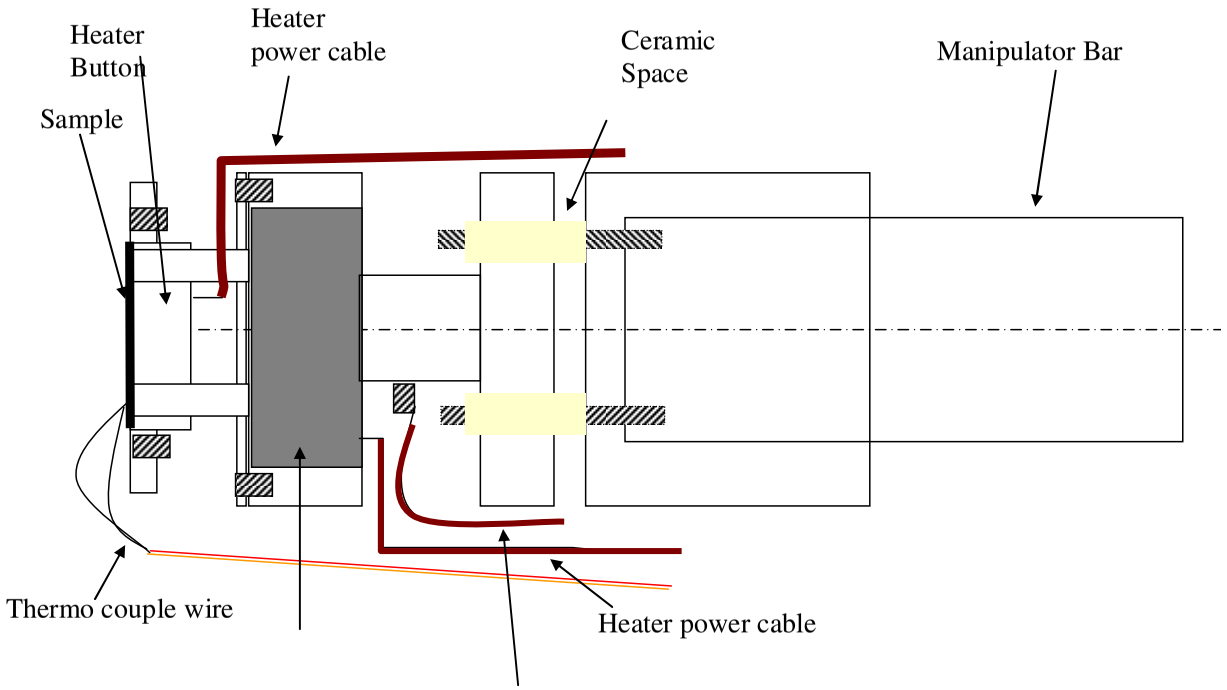

Figure 2.16 schematic of the sample holder with linear transfer shaft.

2.6 Energy spectrum and smoothing

As discussed in the previous section, time of flight spectrum or channel spectrum on MCA can be converted to energy spectrum using conversion function with parameters P_1, P_2 and P_3. The energy is determined from the flight time distribution using the equation (2.22). However the data are acquired in bins with equal time. In the time of flight spectrum count rate (N (t)) is the number of counts per unit time and corresponding count rate in the energy spectrum (N (E)) is number of counts per unit energy. That can be calculated using equation 2.26.[31]

$$N(\#_{MCA})x\left(\frac{(P_1-\#_{MCA})^3}{2P_2^2}\right)\rightarrow N'(\#_{MCA})\xrightarrow{\#_{MCA}=P_1-\frac{P_2}{\sqrt{E_k-P_3}}}\rightarrow N(E) \qquad 2.26$$

Figure 2.17 shows the energy spectrum of Cu (100).

Theory behind the conversion from N(t) to N(E) is explained by following equations.

$$\int_{t_1}^{t_2} N(t)dt \Leftrightarrow \int_{E_1eV}^{E_2eV} N(E)dE \qquad 2.27$$

Time $t = t(E)$ the derivative of t is dt with partial differential equation,

$$dt = \frac{dt(E)}{dE}dE \qquad 2.28$$

Substituting from equation (2.23) to (2.24)

$$\int_{t(E_1}^{t(E_2)} N(t(E)\frac{dt(E)}{dE}dE \Rightarrow \int_{E_2}^{E_1} N(E)dE \qquad 2.29$$

$$\text{Hence } N(E) = N(t(E)\frac{dt(E)}{dE} \qquad 2.30$$

In figure 2.17 Y axis represents N(E) and X axis represents corresponding energy. Physics implies that the counts per time interval (channel number) are proportional to

dE . Consequently the number of counts per time interval (channel number) is small at low energy as shown in figure 2.17. The data is noisy due to low count rates according to Poisson statistics. The Poisson distribution is generally appropriate for counting experiments where data represent the number of events observed per unit time interval. According to the Poisson statistics relative uncertainty, $\sigma = \frac{N}{\sqrt{N}} = \sqrt{N}$, it is smaller when counting rate is higher. Therefore raw data need to be smoothed. Due to the wide variation in the number of counts per energy, Savitsky Golay method is not suitable for smoothing of our data. The method, in which the number of points averaged is proportional to the number of data points per unit energy, is useful. The moving average method which is used to smooth our data works very well (Appendix A). Figure 2.18 shows smooth spectrum of Cu (100) after smoothing the spectrum in figure 2.17 with dE =3eV. The low energy side is completely clear after smoothing. Our algorithm has a ability to smooth according to given energy range (dE).

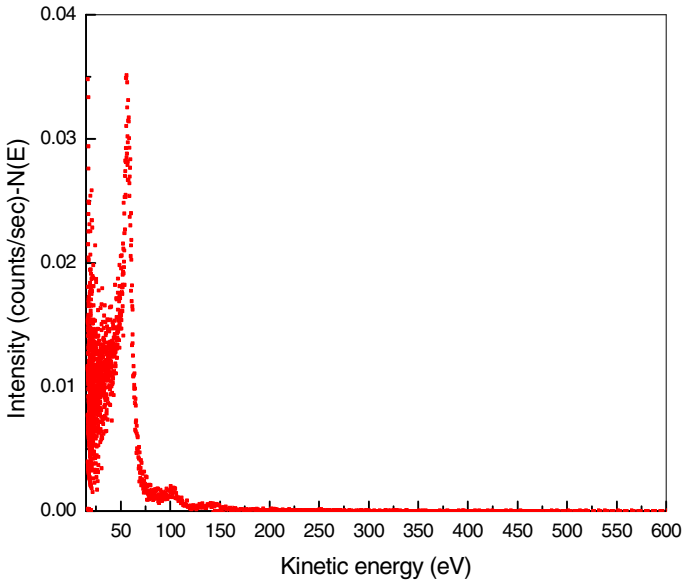

Figure 2.17 Energy spectrum of Cu (100).

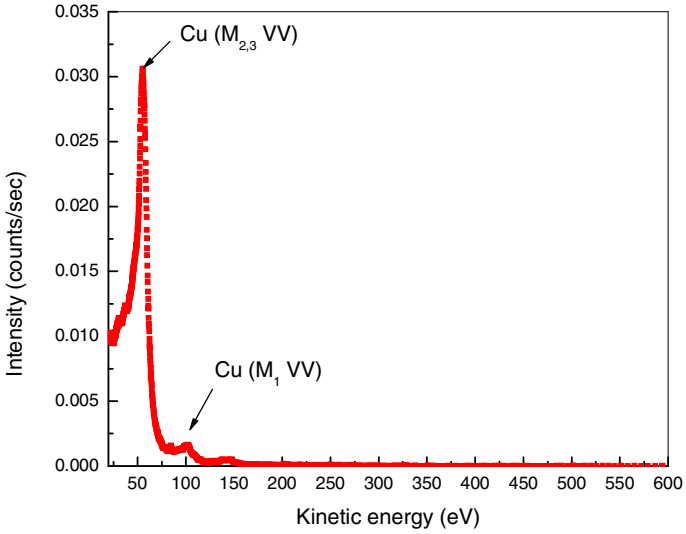

Figure 2.18 Energy spectrum of Cu (100) after smoothing with dE =3eV.

2.7 Energy resolution of the TOF-PAES system

The energy resolution function of the TOF spectrometer strongly depends on two major factors. Those are time resolution of the TOF measurement itself and the spread in the distribution of trajectories of electrons through the spectrometer. In general we can estimate the width of a peak (ΔE_m) measured using a given spectrometer using following equation.

$$\Delta E_m = \sqrt{(\Delta E_{spec})^2 + (\Delta E_s)^2} \qquad 2.31$$

$$\Delta E_{spec} = \Delta E_{spec}(E, P(\theta)) \qquad 2.32$$

Where ΔE_{spec} is spread in energy introduced by the measurements in the analyzer and ΔE_s is the width of the peak as it would be measured by a perfect spectrometer.

The energy width ΔE_m of a peak measured using our TOF PAES system was modeled as follows.

$$\Delta E_m = \sqrt{(\Delta E_s)^2 + ((\Delta E_\theta)^2 + (\Delta E_t)^2)} \qquad 2.33$$

Where ΔE_s is the width of the energy distribution of electrons leaving the surface of the sample as would be measured by a perfect energy spectrometer.[37] ΔE_θ is the width of the distribution of measured energies associated with the angular distribution of electrons leaving the sample. ΛE_t is the width of the distribution of measured energies associated with time spread.

If the electrons have trajectories parallel to the horizontal axis of TOF then the kinetic energy can be written as follows

$$E = \frac{1}{2} m_e \left(\frac{l}{t}\right)^2 \qquad 2.34$$

Where, l is the length of the TOF tube, t is the flight time of outgoing electron and m_e is the mass of electron.

For the convenience equation 2.34 can be rearranged as follows,

$$E = \frac{\alpha}{t^2} \qquad 2.35$$

Where $\alpha = \left(\frac{m_e l^2}{2} \right)$ is a constant, which is equal to 283 x 10^4 eV.(ns)^2

Taking the derivative of both side of equation 2.35,

$$\frac{dE_t}{dt} = \alpha \frac{d}{dt}\left(t^{-2}\right) \qquad 2.36$$

After rearranging the equation 2.35 and 2.36 following equation can be obtained

$$\Delta E_t \approx 2E \frac{\Delta t}{t} \qquad 2.37$$

where t is the time of flight of Auger electron, Δt is the width of the peak in time spectra, and E is the kinetic energy of Auger electron. Here ΔE_s, ΔE_θ, and ΔE_t are assumed to have no cross correlation. The contribution to the estimated width of a peak measured from the angular distribution of the out going electrons from the sample due to the magnetic field can be approximated as follows[37]

$$\Delta E_\theta = E(B_a / B_s) \qquad 2.38$$

Where B_a the magnetic field in the TOF drift region and B_s is the magnetic field at the sample which is the sum of magnetic field due to the magnet behind the sample and solenoid currents.

Combining equations 2.33, 2.37 and 2.38 ΔE_m can be written as follows.

$$\Delta E_m = \left[\Delta E_S^2 + E^2 (\frac{B_a}{B_S})^2 + 4 * \left(\frac{\Delta t}{t} \right)^2 E^2 \right]^{\frac{1}{2}} \qquad 2.39$$

ΔE_m can be re written by substituting Δt from equation 2.35 to equation 2.39.

$$\Delta E_m = \left[(4\frac{\Delta t^2}{\alpha}) E^3 + (\frac{B_a}{B_S})^2 E^2 + \Delta E_S^2 \right]^{1/2} \qquad 2.40$$

Comparing equations 2.31 and 2.40, ΔE_{spec}^2 can be set as follows,

$$\Delta E_{spec}^2 = \left(\frac{4\Delta t^2}{\alpha} \right) E^3 + \left(\frac{B_a}{B_s} \right)^2 E^2 \qquad 2.41$$

Where ΔE_{spec}, represents the width of the resolution function of the spectrometer and it would result from a mono-energetic electron leaving the surface of the sample having a given angular distribution).

The equation 2.41 can be rearranged as follows,

$$\Delta E_m = \left[(1.4x10^{-6} A_1^2) E^3 + A_2^2 E^2 + A_2^3 \right]^{1/2} \qquad 2.42$$

Where $\frac{4}{\alpha} = 1.4x10^{-6} eV^{-1} (ns)^{-2}$ and parameters A_1, A_2 and A_3 are Δt, $\frac{B_a}{B_s}$ and ΔE_S respectively.

In order to measure ΔE_{spec} directly and to test the model distribution the secondary electron spectra were measured with a series of different sample bias values. Figure 2.19 shows the secondary electron spectra as obtained from the Cu (100) single crystal with different sample bias voltage in the range of -20 V to -900 V. A negative bias voltage (V_{sbias}) was applied to shift the peak of the secondary electron energy

distribution to higher energies. It also results in the acceleration of primary positron beam. Hence the energy of incident positrons on the sample would be (15eV + (-eV_{sbias})). The bias between the sample and the beam tube will also change the angular distribution of electrons leaving the sample region. Figure 2.20 shows the general shape of (a) the channel and (b) energy spectrum of secondary electrons from Cu (100) with primary beam energy at 115 eV on the sample surface. Figure 2.21 contains the FWHM (ΔE_m) of secondary electron spectra corresponding to different sample bias voltage as a function of energy. The FWHM of the spectra is narrower with smallest negative sample bias voltage and it is getting broader at high negative sample bias voltage.[38,39] During this experiment the heater button is sitting between sample and the magnet. Therefore the measured magnetic field in front of sample B_S is ~503 Gauss and that is much smaller than that of without the heater, which has a value of 1850 Gauss.

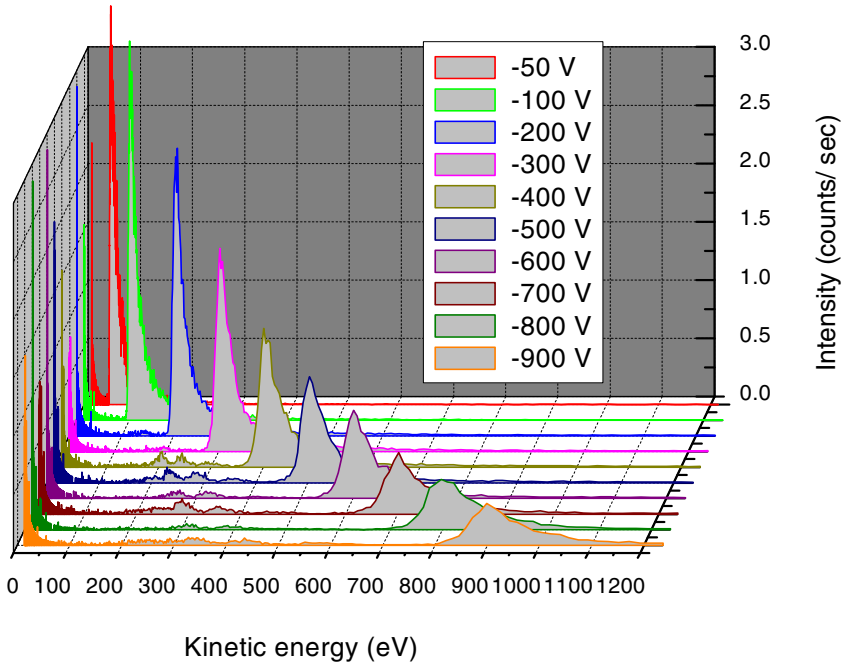

Figure 2.19 The change in energy spectrum of secondary electrons from Cu (100) with different sample bias voltage (V_{sbias}).

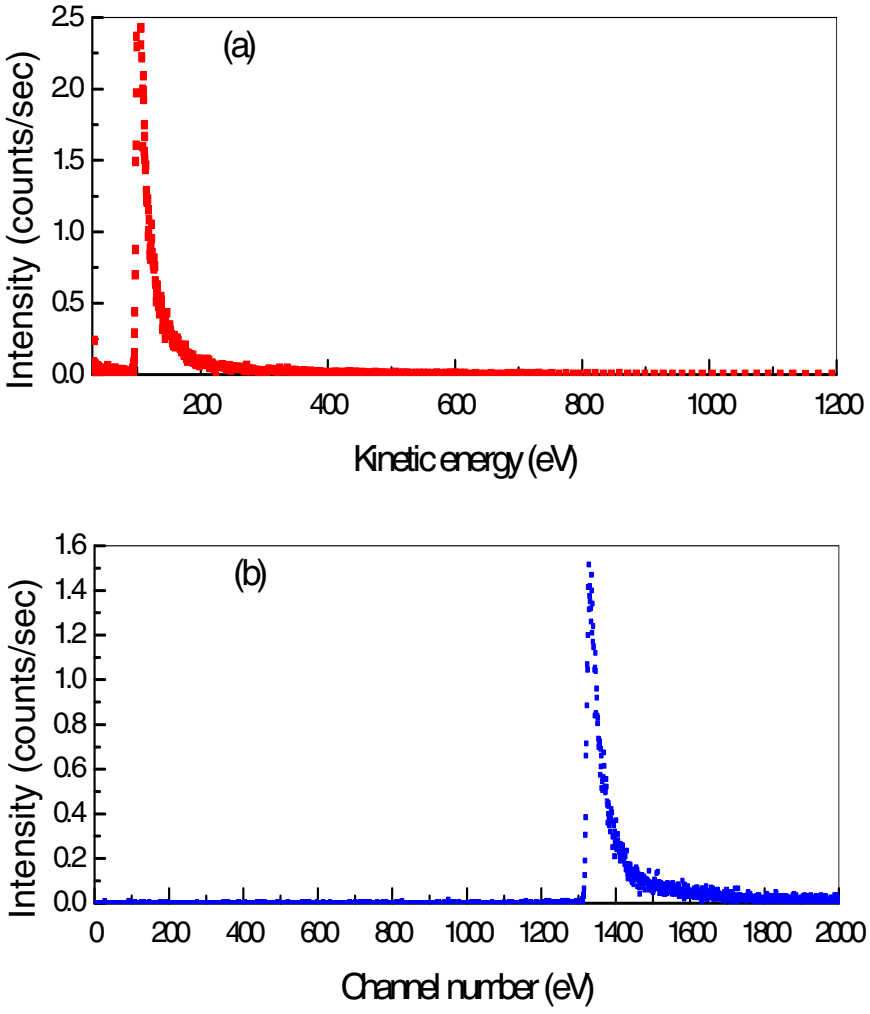

Figure 2.20 The general shape of (a) energy (b) channel spectrum of secondary electrons from Cu (100) with incident primary positron beam energy at 115 eV on the sample surface. The sharp turn on the intensity is at energy of 100 eV ($=-eV_{sbias}$)

The red solid curve is fitted using modeled equation (2.42). The generated values for parameters A_1, A_2 and A_3 are 1.93 ±0.407 (ns), 0.0546 ±0.01383, and 2.35 eV respectively. According to values generated for parameters, the time resolution (Δt) of the TOF-PAES system itself is 1.93 ns if heater button is between sample and magnet.

The FWHM (ΔE_m) of secondary electron spectra corresponding to different sample bias voltage as a function of energy for polycrystalline Cu are shown in figure 2.22. The polycrystalline Cu sample is sitting on the magnet in this experiment. According the fitting parameters, the time resolution of the system (Δt) of the TOF-PAES system is ~1.8036 ±0.41574 ns.

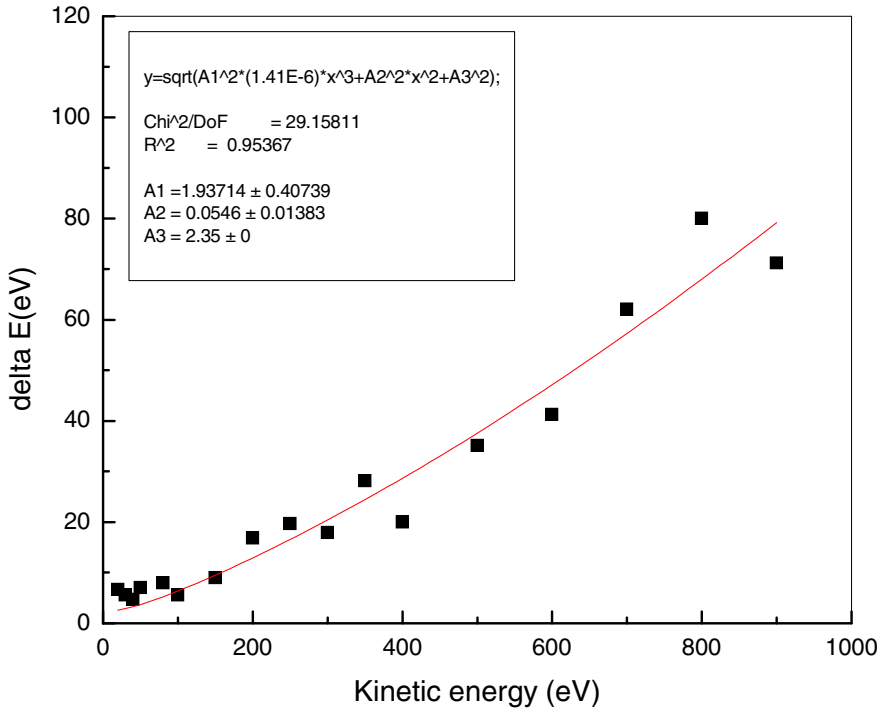

Figure 2.21 the FWHM (ΔE_m) of secondary electron spectra as a function of peak energy. Note there is a heater button between Cu (100) sample and the magnet.

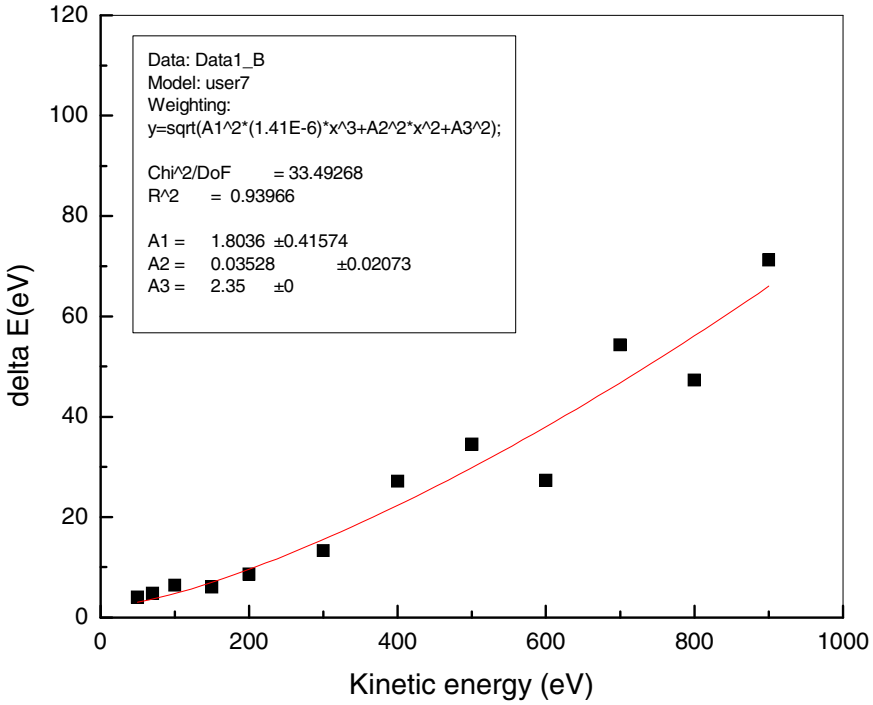

Figure 2.22 the FWHM (ΔE_{total}) of secondary electron spectra as a function of peak energy. Note there is no heater button between polycrystalline Cu thin film and the magnet.

CHAPTER 3

COPPER(I) OXIDE

3.1 Introduction

Copper(I) oxide, Cu_2O has attracted increasing attention in recent years as an active component in solar cells and photodiodes. It has also been used as a photocatalyst for solar water splitting and H_2 generation.[10-12]

Cuprous oxide is a simple cubic structure with 4 Cu and 2O atoms in its basis and a lattice constant of 4.27 Å.[40] The Cu atoms form a FCC lattice and O atoms form a BCC lattice where each O atom is surrounded by a tetrahedron of Cu atoms. It is a p-type semiconductor due to copper vacancies with band gap energy of 2.1eV. The p-Cu_2O formed junctions with other oxide semiconductors such as n-TiO_2 [41] and n-ZnO [42,43] for solar cell applications. Figure 3.1 shows the basis structure of Cu_2O. The color of Cu_2O is red and it is an inexpensive, a non toxic and widely available material. Several methods can be used to prepare Cu_2O thin films such as anodic oxidation, thermal oxidation, vacuum evaporation, electrodeposition, spray coated method and a variety of gas-phase deposition techniques including radio frequency magnetron or reactive sputtering, vacuum deposition ,molecular deposition molecular beam epitaxy and laser ablation. In this chapter, spray coated cuprous oxide powder on Tantalum substrate and

electrochemically deposited cuprous oxides have been investigated using TOF-PAES and electron induced Auger electron spectroscopy.

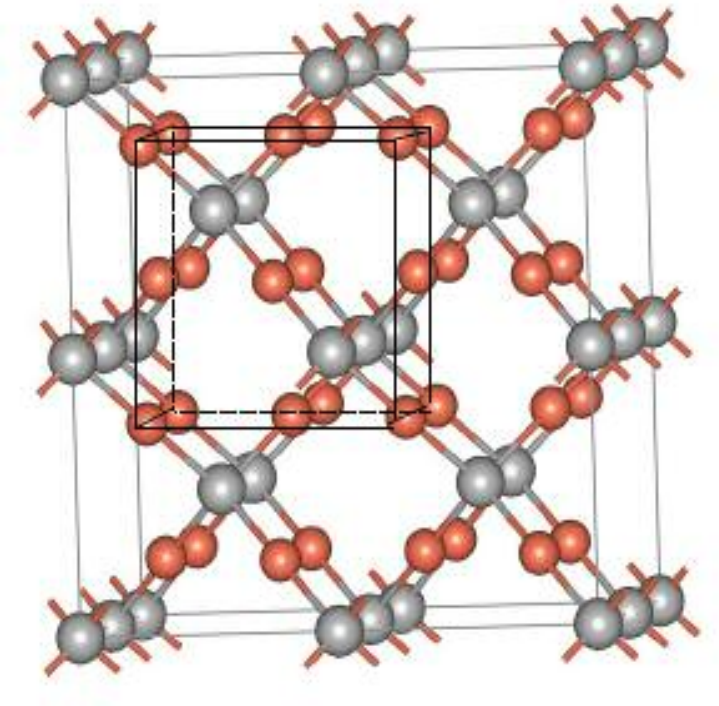

Figure 3.1 Cu_2O structure.

3.2 Spray coated Cu_2O on Tantalum

3.2.1 Experimental details

Cu_2O thin film was prepared by spraying a colloidal mixture of Cu_2O powder (Alfa easer, 99.998%) and isopropyl alcohol onto a Tantalum (Alfa easer 99.95%) substrate. The spray coated thin film was dried in an oven at temperature at 55^0C for one hour. PAES measurements were taken at room temperature from the Cu_2O thin film before and after vacuum annealing at 300 ^{0}C for 13 min. PAES measurements were also

taken after re-oxidation of Cu_2O thin film with O_2 (UHP 99.999%) at room temperature. Oxygen dose was started at 0 L and increased up to 10^7 L.

3.2.2 Results and discussion

The surface morphology of the Cu_2O thin layer on Ta is shown in figure 3.2. According to the SEM image size of the Cu_2O grains are in the range of 1-4 micron. The surface of the thin film is not uniform. Figure 3.3 shows the distribution of flight time of electrons emitted subsequent to the annihilation of positrons at the surface of the Cu_2O thin film sample before and after thermal annealing in the vacuum at 300 ^{0}C for 13 min.

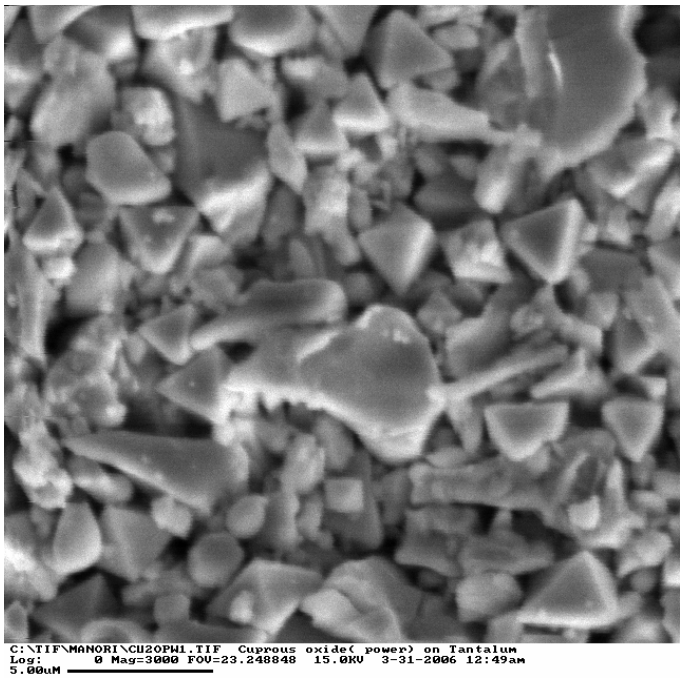

Figure 3.2 SEM image of dip coated Cu_2O on Tantalum substrate.

The C(KLL) and O(KLL) peaks are clearly visible in the PAES timing spectra of the "as received" sample shown in fig. 3.3 (a). After thermal annealing at 300 ^{0}C, a strong peak appears in the spectra due to electrons emitted as a result of an annihilation induced $M_{2,3}$ VV Auger transition as shown in figure 3.3 (b). Figure 3.4 shows the energy spectra calculated from the time-of-flight data shown in fig. 3.3 (a) and 3.3 (b) along with a reference spectra from a clean Cu(100).

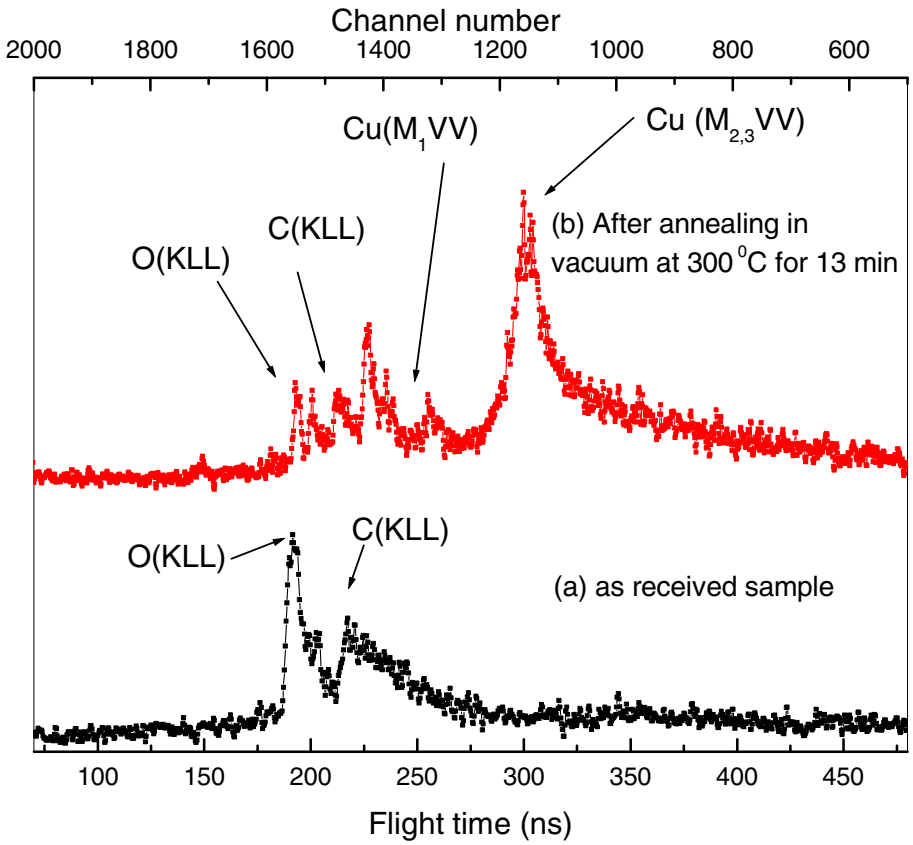

Figure 3.3 Distribution of flight times of positron annihilation induced Auger electrons from a Cu_2O surface (a) before and (b) after thermal anneal at 300 ^{0}C for 13 min.

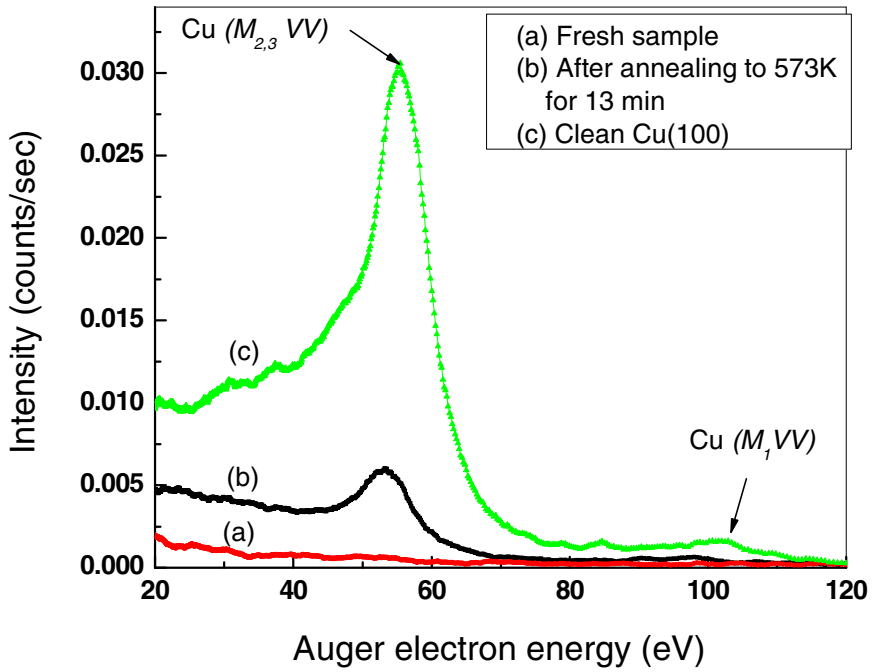

Figure 3.4 PAES energy spectra of Cu_2O (a) before, (b) after thermal anneal at 300 ^{0}C for 13 min., and (c) reference spectra from a clean Cu(100).

The total intensity of PAES energy spectra of the sample before annealing (fig. 3.4 a) is almost flat while the Cu $M_{2,3}VV$ Auger transition at ~53.5 eV and the Cu M_1VV transition at ~101 eV are clearly visible after thermal anneal (fig. 3.4b) at 300 ^{0}C for 13 min. The spectrum for the Cu (100) single crystal features the corresponding signals at ~55.6 eV and ~103.4 eV respectively. Previous studies[15] showed that the vacuum annealing led to the removal of O-H related features. The absence of a Cu PAES peak before annealing is consistent with the presence of a complete overlayer that pushes the positron wave function away from the Cu atoms at the overlayer-Cu_2O interface.

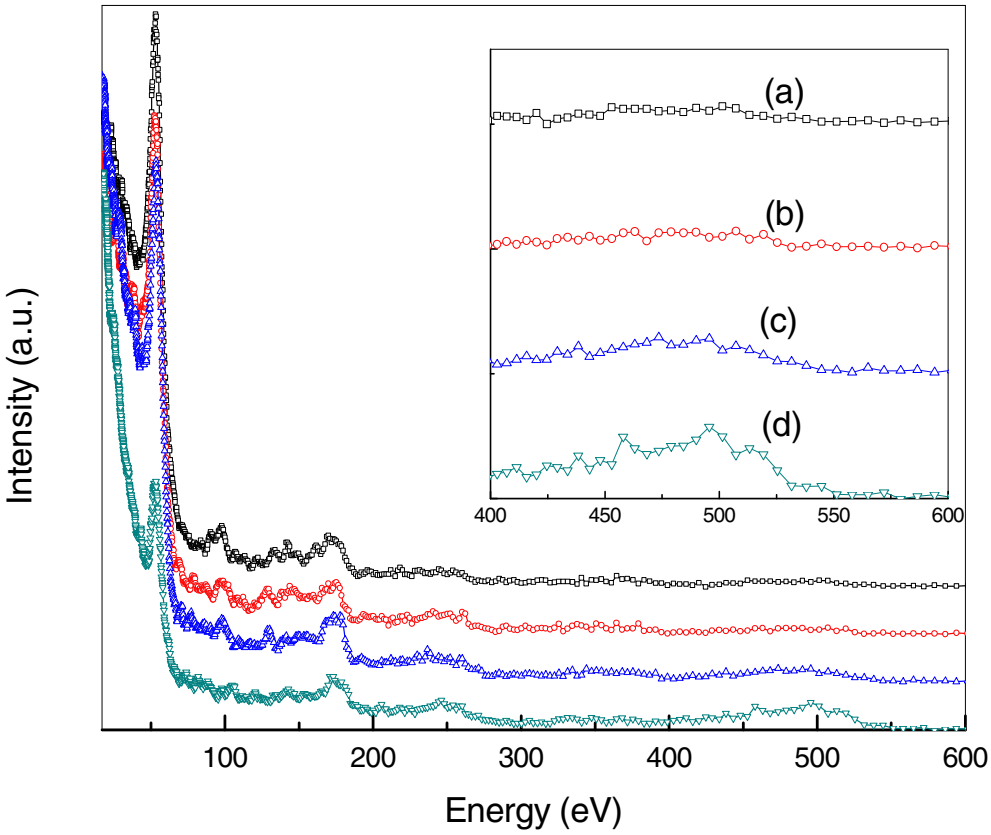

Figure 3.5 PAES spectra after re-oxidation at room temperature (a) after thermal anneal at 300 ^{0}C for 13min. (b) ~1.0 x 10^{5} L , (c) ~7.11 x 10^{6} L , and (d) ~1.3 x 10^{7} L.

The appearance of a strong Cu peak indicates that the overlayer present on the surface of the Cu_2O before annealing has been substantially removed after vacuum annealing at 300 ^{0}C.[15] The observed shift of 2.1eV to lower energy of the Cu peak observed from the vacuum annealed Cu_2O thin film as compared to the peak observed from clean Cu(100) is indicative that the Cu atoms at the surface of the Cu_2O are bound to oxygen. [44]

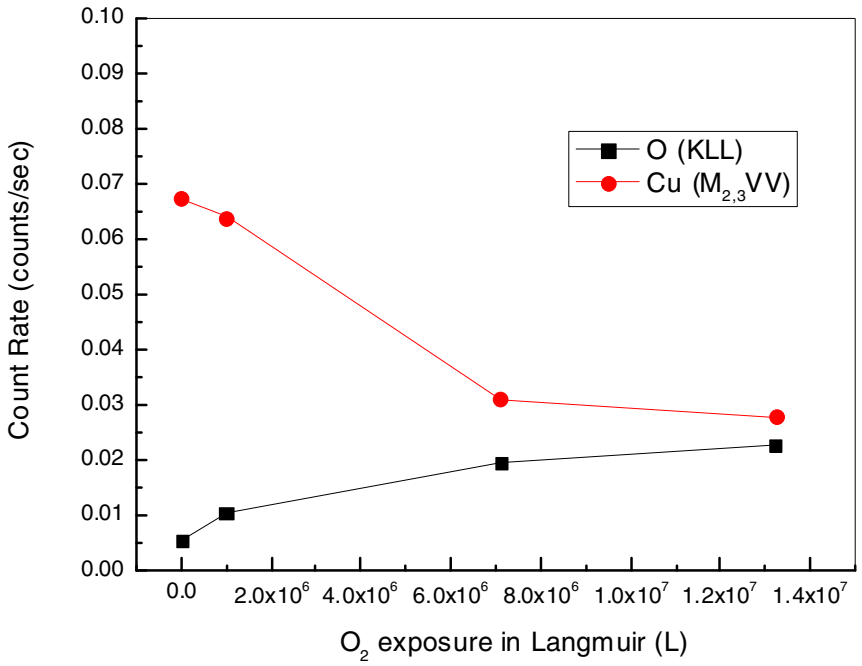

Figure 3.6 Intensity of Cu and O peaks as a function of O_2 exposure.

Figure 3.5 shows a series of PAES spectrum obtained before (Fig. 3.5a) and after exposure of the annealed Cu_2O thin surface to 1.0 x 10^5 L (Fig. 3.5 b), 7.1 x 10^6 L (Fig. 3.5 c) 1.3 x 10^7 L (Fig. 3.5 d) of O_2 [the unit L signifies a Langmuir corresponding to an exposure to 10^{-6} Torr for 1 sec.]. The Cu $M_{2,3}VV$ peak at ~53.5 eV may be seen to decrease with increasing oxygen exposure while the O KLL peak at ~500 eV grow larger and more narrow. Figure 3.6 shows a plot of the intensity of the Cu and O peaks as a function of O exposure of the Cu_2O. The PAES peak intensities were determined from the areas under the Cu $M_{2,3}VV$ and O KLL Auger transitions. As may be seen in figure 4, the Cu $M_{2,3}$ VV Auger intensity decreases and the O KLL Auger signal

increases as a function of oxygen dose. Surface modification of a spray deposited Cu_2O polycrystalline thin film by vacuum annealing and low pressure oxygen exposure has been studied with positron annihilation induced Auger electron spectroscopy. The PAES measurements showed that Cu was exposed in the top most layer of Cu_2O after annealing in the vacuum at 300 ^{0}C for 13 minutes. The PAES measurements during re-oxidation of the previously annealed Cu_2O thin film suggested that Cu atoms at the surface were partially covered with O after exposure to 1.3 x 10^7 L of O_2 resulting in a significant decrease in the PAES Cu signal and a significant increase in the PAES O signal. These results demonstrate the utility of PAES in the study of oxide surfaces.

3.3 Electrochemically deposited Cu_2O

3.3.1 Preparation of Cu_2O on TCO

The polycrystalline Cu_2O samples were prepared by cathodic electro deposition as described elsewhere.[12,45-55] The electrolyte consists of 0.4 M copper(II) sulfate (Alfa Aesar, 98-102%), 3 M lactic acid and distilled water.[56,57] A standard single-compartment, three-electrode electrochemical cell was used for film preparation as shown in figure 3.7. A Cu mesh and an Ag|AgCl|satd. KCl reference electrode (Microelectrode Inc.) along with a transparent conducting oxide (TCO) substrate (indium tin oxide, ITO coated on soda lime glass) as the working electrode, completed the cell set-up. Electrodeposition was carried out with an EG & G Princeton Applied Research Versastat II potentiostat and at a bath temperature of 60 ^{0}C. The pH value of the bath was carefully adjusted to 9.0, 10.0 and 12.0 by controlled addition of 4 M

NaOH (Alfa Aesar, 97%). The oxide films were grown at -0.40 V (vs. Ag|AgCl|satd. KCl reference) for a nominal duration of 30 min. The surface morphology of the films was studied using ZEISS supra 55 VP scanning electron microscopy (SEM). The X-ray Diffraction (XRD) were measured using X-ray Siemens D-500 powder diffractometer using CuK_{α} radiation and it confirmed that the predominant crystallographic planes of the Cu_2O thin films on TCO glass were (200), (110) and (111) with electrolyte pH of 9.0, 10.0 and 12.0 respectively.[8m] These three types of Cu_2O films are designated, in what follows, as Cu_2O (9.0), Cu_2O (10.0), and Cu_2O (12.0) respectively. Figure 3.8 shows the SEM images and XRD spectra of Cu_2O on TCO. The SEM micrograph indicates that the grains in the Cu_2O on TCO with predominant orientation (111) are larger than that of other two predominant orientations. The average thickness of the Cu_2O thin films were in the range of 1-2 μm. The grain size of Cu_2O with different predominant orientation is different.

The average thickness of the Cu_2O films was in the range of 1-2 μm as assessed by stylus profilometry. A Cu (100) film (Matech Company, Germany) was polished on one side to a roughness less than 0.3 μm prior to measurements.. The XRD spectra confirmed that the predominant crystallographic planes of the Cu_2O thin films on TCO glass were {200}, {110} and {111} with pH of electrolyte 9.0, 9.9 and 12.0 respectively.

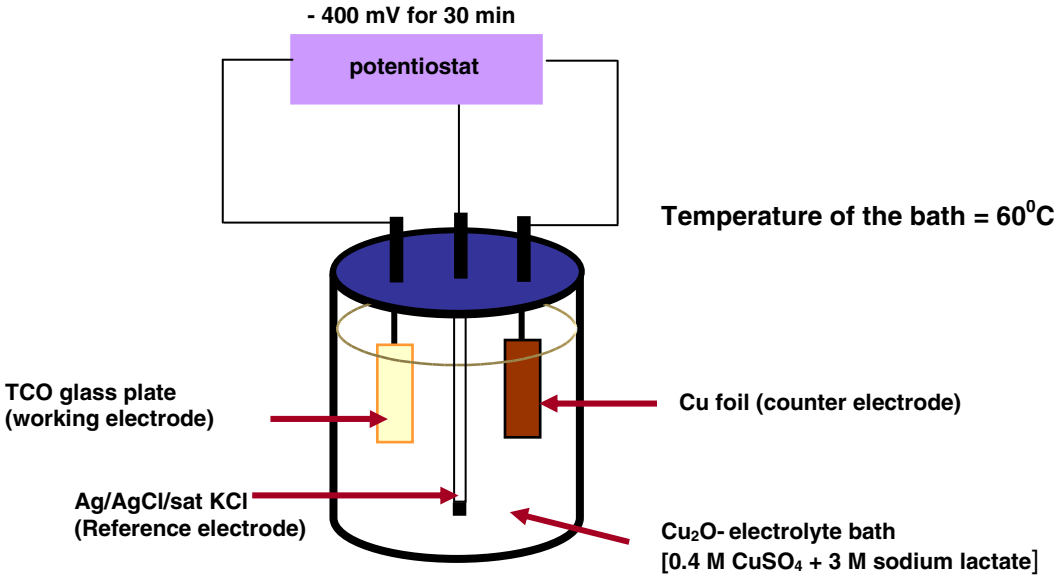

Figure 3.7 Schematic of electrochemical deposition set up with three-electrode electrochemical cell.

TOF-PAES spectra were obtained for all electrodeposited Cu_2O on ITO samples at room temperature after each *in situ* annealing at 100, 200, 250, 300, 350 and 400 ^{0}C for 1 min. The substrate temperature was measured using a K-type thermocouple. Heating of the sample was performed using non gassy standard UHV button heater (HeatWave Labs, Inc) situated behind the back of the sample. The sample chamber was maintained at a pressure below ~ 2.0 x 10^{-8} Torr during the time of the PAES measurements.

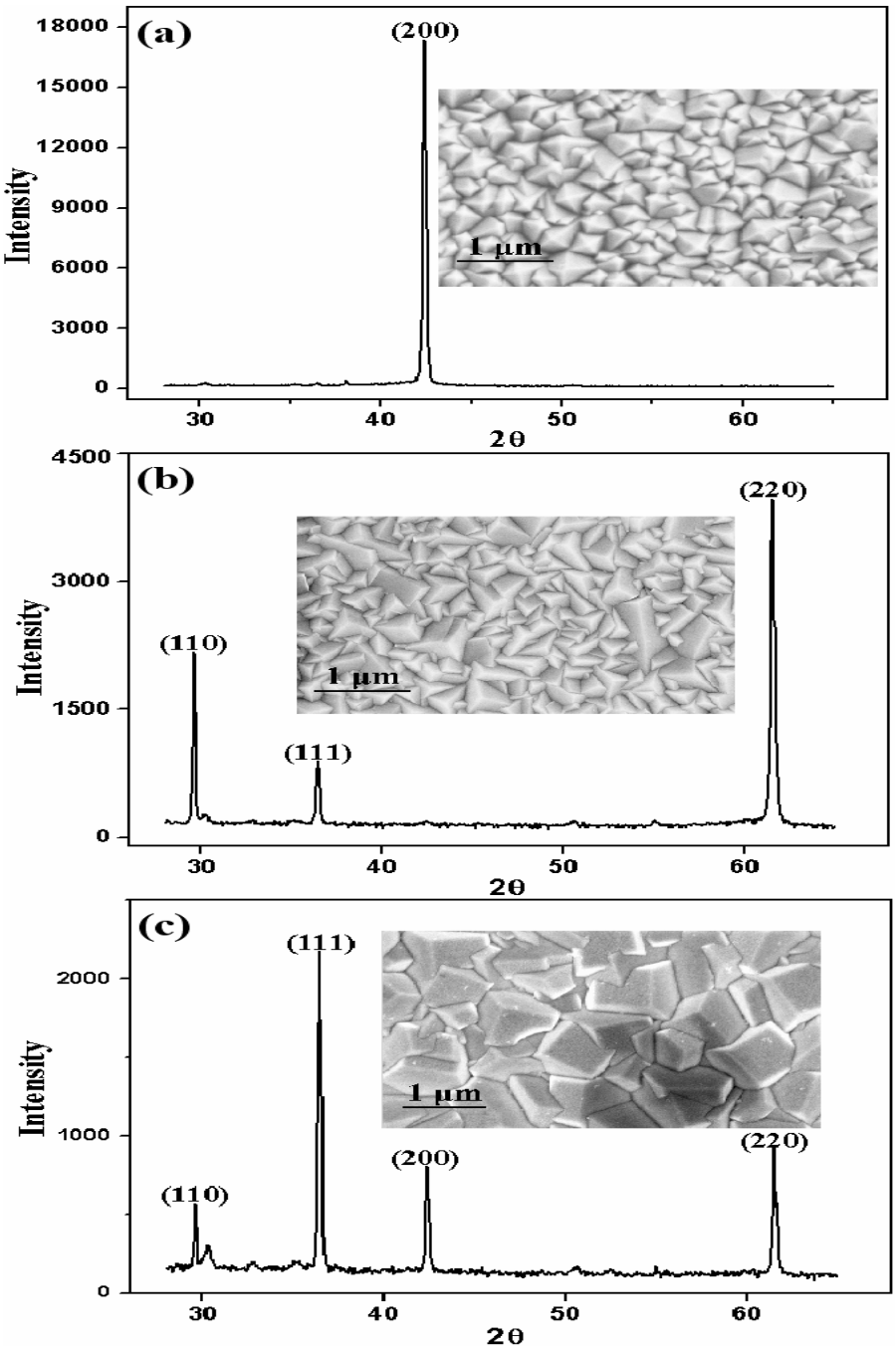

Figure 3.8 SEM images and XRD spectra of Cu_2O on TCO with solution pH (a) (9.0), (b) (10.0), and (c) (111).[55]

3.3.2 Results and discussion

Figure 3.9 (a) and (b) contain the PAES spectra for a Cu_2O (12.0) sample before and after thermal anneal at 400 ^{0}C. The spectrum prior to thermal anneal is almost flat (Figure 3.9 a) while the Cu $M_{2,3}VV$ Auger transition at ~53.5 eV and the Cu M_1VV transition at ~101 eV are clearly visible after thermal anneal (Figure 3.9 b). A spectrum of the Cu (100) is shown for comparison in figure 3.9 (c), and features the corresponding signals at ~55.6 eV and ~103.4 eV respectively. The observed shift of 2 eV to lower energy going from Cu to the annealed Cu_2O surface is consistent with the corresponding 2.1 eV shift in the Cu LVV peak seen for Cu_2O using X-ray induced AES and is indicative that the Cu atoms at the surface of the annealed Cu_2O surface are at least partially oxidized.[44] It should be noted that, unlike the X-ray induced AES data in reference 44, in which the width of the LVV peak observed for Cu_2O is nearly twice that observed for Cu, the PAES peak from the Cu_2O surface remains narrow with what appears to be a shoulder at the position of the un-shifted Cu peak suggesting that at least some of the Cu atoms at the surface are in a reduced state.

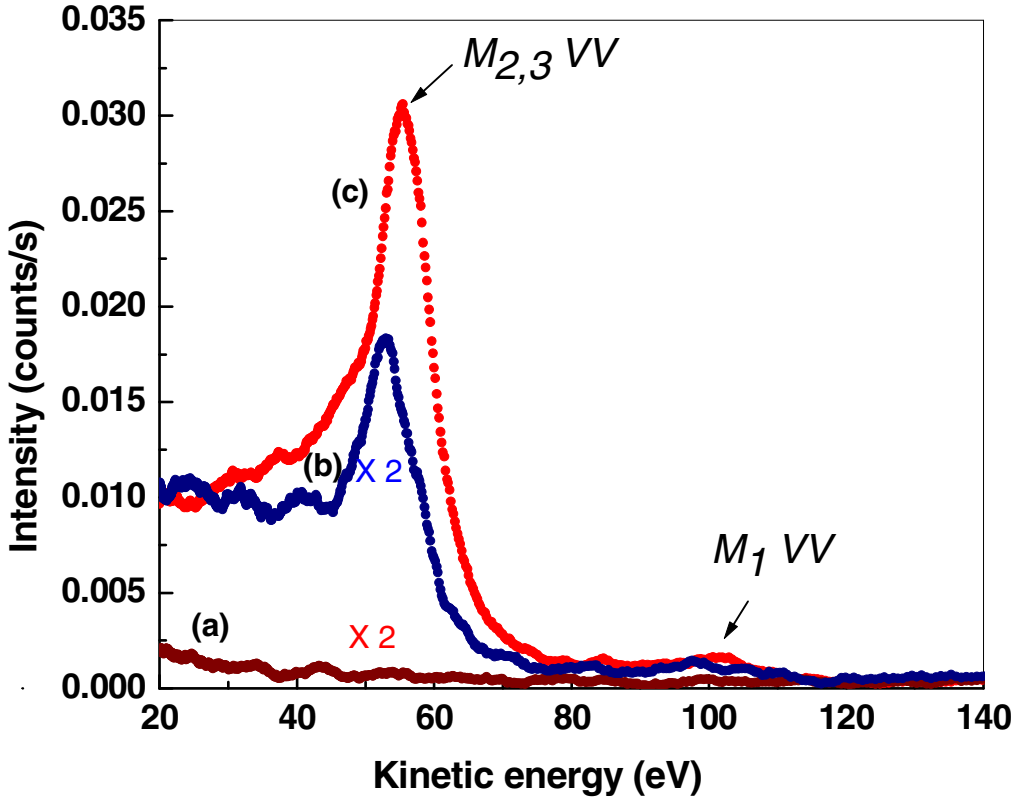

Figure 3.9 PAES profiles of Cu_2O (12.0) thin film (a) before and (b) after thermal anneal at 400 ^{0}C for 2 min and (c) Cu (100) single crystal. Data corresponding to spectra (a) and (b) were expanded two times with respect to their original data.

Prior studies have demonstrated that PAES probes the top-most layer and that the presence of a complete overlayer can block the Auger signal from the substrate due to the trapping and localization of the positrons just outside the top layer prior to annihilation.[24] Thus absence of a significant Cu PAES signals prior to annealing (Figure 3.9a) and the relatively large Cu PAES signal seen after annealing (~30% of the clean Cu signal after annealing at 400 ^{0}C) provides strong evidence that the Cu_2O surface is completely covered with an overlayer prior to annealing and that this overlayer is

largely removed after annealing at 400 ^{0}C.

Figure 3.10 shows the effect of vacuum annealing on the PAES spectra of the electrodeposited Cu_2O surfaces. The data in panel 3.10a, 3.10b, and 3.10c were obtained for samples grown in a solution with pH 9, 10 and 12 respectively. Each sample was subjected to a series of isochronal anneals of 2 min at temperatures of 100, 200, 250, 300, 350 and 400 ^{0}C. PAES measurements (~11 hr each) were made before and after each annealing cycle.

It may be seen that for each of the three series of PAES data shown in Figure 3.10, the Cu $M_{2,3}VV$ peak grows monotonically with increasing anneal temperature, obtaining significant intensity starting at ~250 ^{0}C in the case of the samples grown at pH 9, pH 10, and ~200 ^{0}C for the pH 12 sample. The PAES spectra of all samples reveal carbon KLL Auger transition at around ~273 eV and an oxygen Auger transition at 503 eV. The carbon peak intensity increases with the annealing temperature up to 300 ^{0}C temperature and decreases noticeably at 400 ^{0}C. The O signal intensity stays constant during this sequence of thermal anneal while the peak width becomes narrower at 300 ^{0}C. These trends for Cu, C, and O are consistent with the Cu_2O surface becoming progressively cleaner during the anneal treatment. At 300 ^{0}C annealing temperature the color of all the electrodeposited Cu_2O samples changed from red to gray and gave grayish red color at 350 ^{0}C. Previous studies have shown that this color change is an indication of a change from Cu_2O to Cu.

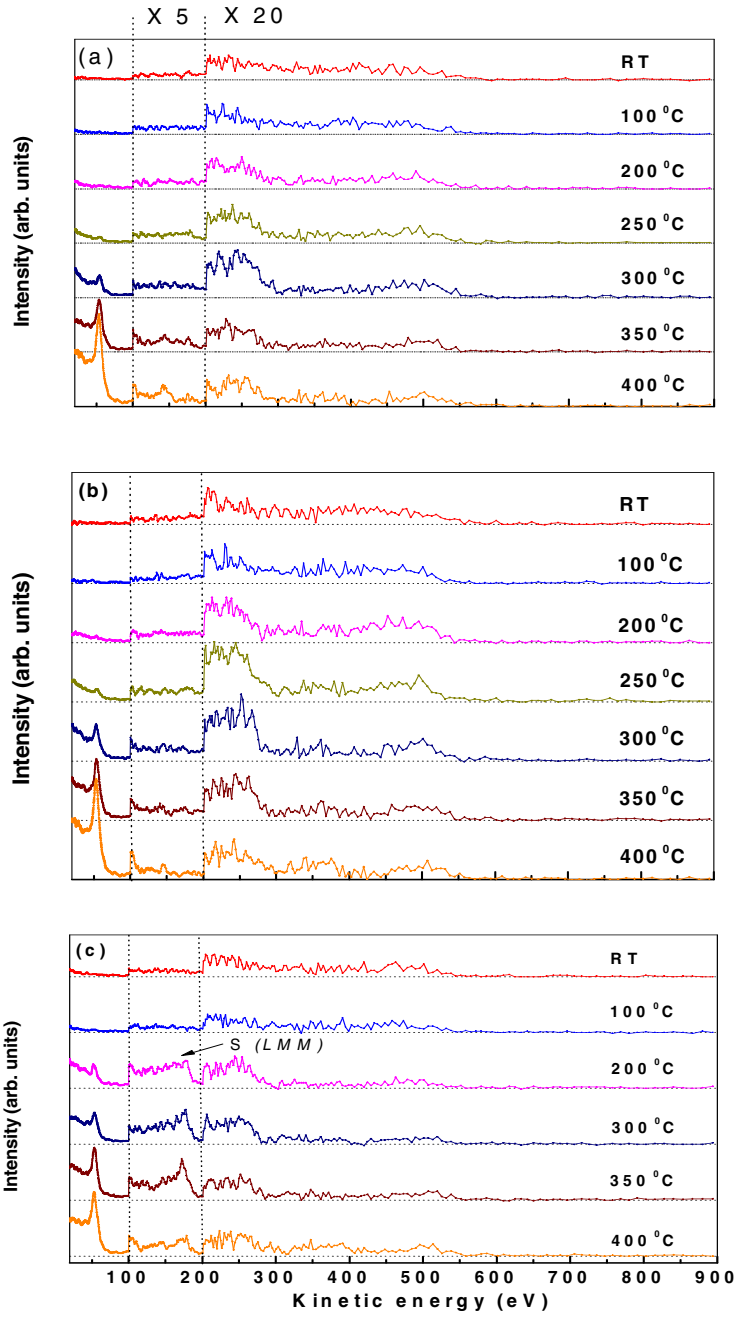

Figure 3.10 PAES profiles of electrodeposited Cu_2O films (a) (9.0), (b) (10.0), and (c) (12.0) as a function of thermal anneal temperature. Data corresponding to kinetic energy in the 100 - 200 eV range were expanded five-fold and data corresponding to energy in the 200 - 900 eV range were expanded 20-fold.

The fact that the PAES signal increases from near zero to a substantial fraction of the clean Cu signal upon annealing is consistent with previous studies which have shown that the presence of a thin over layer results in a large reduction in the PAES signal from the substrate due to the top-layer selectivity of PAES. It should be noted that the Cu_2O (12.0) sample shows a sulfur Auger LMM peak at ~152 eV after thermal anneal at 200 ^{0}C. This peak subsequently disappears after anneal at ~400 ^{0}C. The S signal presumably originates from the sulfate species (from the electrolyte bath) that were adsorbed on the oxide surface.

Figure 3.11 maps the dependence of the intensity of the Cu $M_{2,3}VV$ PAES peak on annealing temperature. It may be seen that for both the sample grown at pH 9 and pH 10, there is a sharp rise in the Cu PAES intensity of starting at ~250 ^{0}C. For the sample grown at pH 12, the increase in Cu intensity with annealing temperature is more gradual and starts at a lower temperature (~100 ^{0}C). The variant evolution for the Cu_2O (12.0) case is correlated with a strong S peak in the PAES spectra for this sample not present in the spectra of the other two samples. This suggests that significantly more S is incorporated into the sample grown at pH 12 than for those grown at pH 9 and 10 (the most likely source of this S is from $CuSO_4$ in the electro deposition solution) and that the presence of S reduces the temperature at which the Cu becomes exposed in the top layer of the Cu_2O surface.

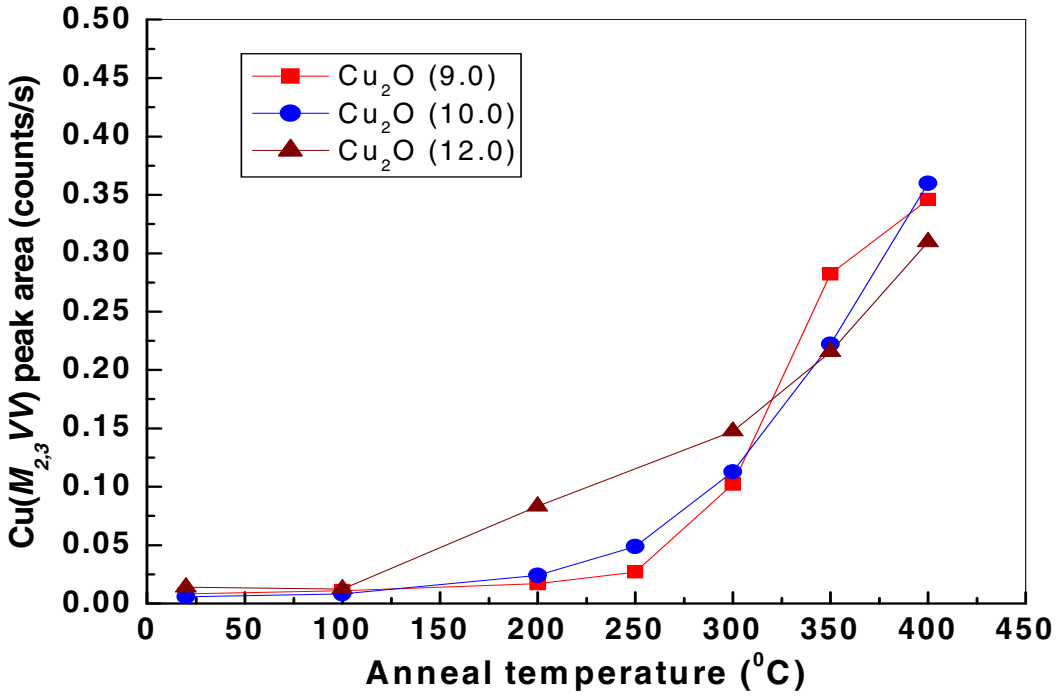

Figure 3.11 Cu ($M_{2,3}VV$) Auger peak integrals from the PAES data for the three types of electrodeposited Cu_2O films as a function of thermal anneal temperature.

Figure 3.12 contains the EAES profiles (dI/dE vs. E) for the baseline (room temperature) case and for samples subjected to four representative thermal anneal steps at temperatures ranging from 200 ^{0}C to 640 ^{0}C. These profiles are shown for the Cu_2O (12.0) sample. The peaks at ~ 58, 770, 844, and 918 eV correspond to the Cu $M_{2,3}VV$, LMM, LMV, and LVV respectively. The C KLL Auger transition is seen at ~269 eV while the O KLL signal appears at ~502 eV (Figure 3.12). The C signal systematically decreases with increasing anneal temperature while the O signal stays relatively constant.

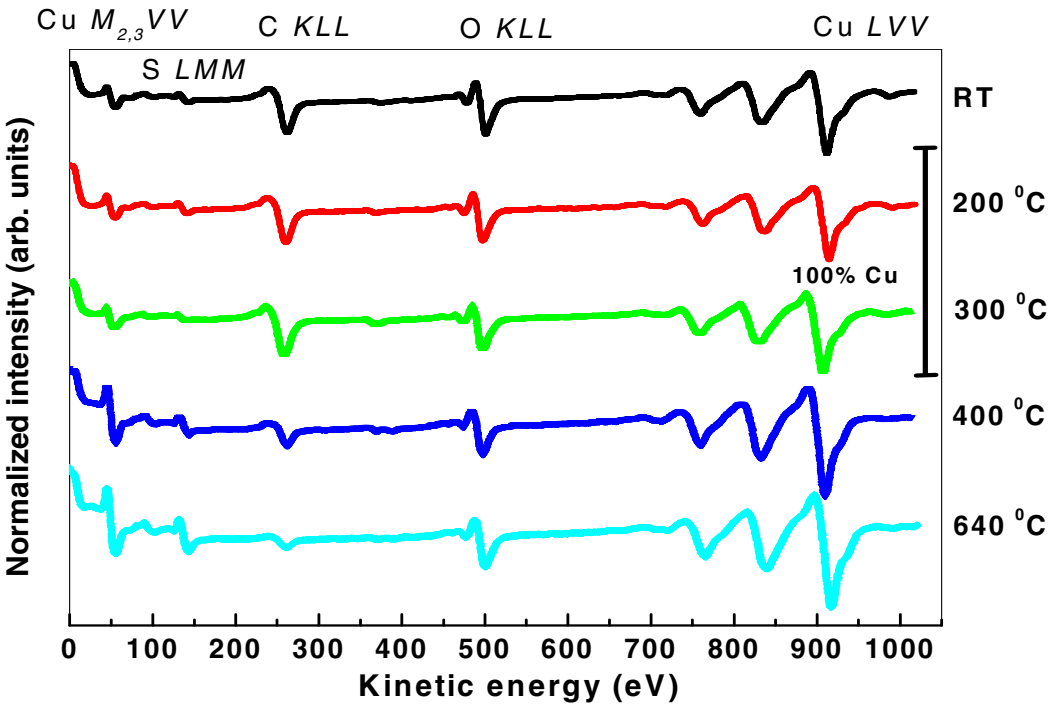

Figure 3.12 EAES profiles of Cu_2O (12.0) after thermal anneal at 200, 300, 400 and 640 ^{0}C.

The near-surface concentrations of Cu, C, O, and S (averaged over the probe depth of EAES) were calculated [PHI Handbook] from the peak-to-peak heights of the Cu $M_{2,3}VV$ (59 eV), C KLL (271 eV), O KLL (503 eV), and S LMM (152 eV) according to the methods outlined in reference 58. We note that the C signal in the EAES spectra decreases in the same range of temperatures (between ~350 ^{0}C and 400 ^{0}C [see Figure 3.13]) as the Cu peak is showing the largest rate of increase in both the PAES and EAES spectra. The O profile remains relatively invariant with the anneal temperature in both EAES (Figure 5) and in PAES.

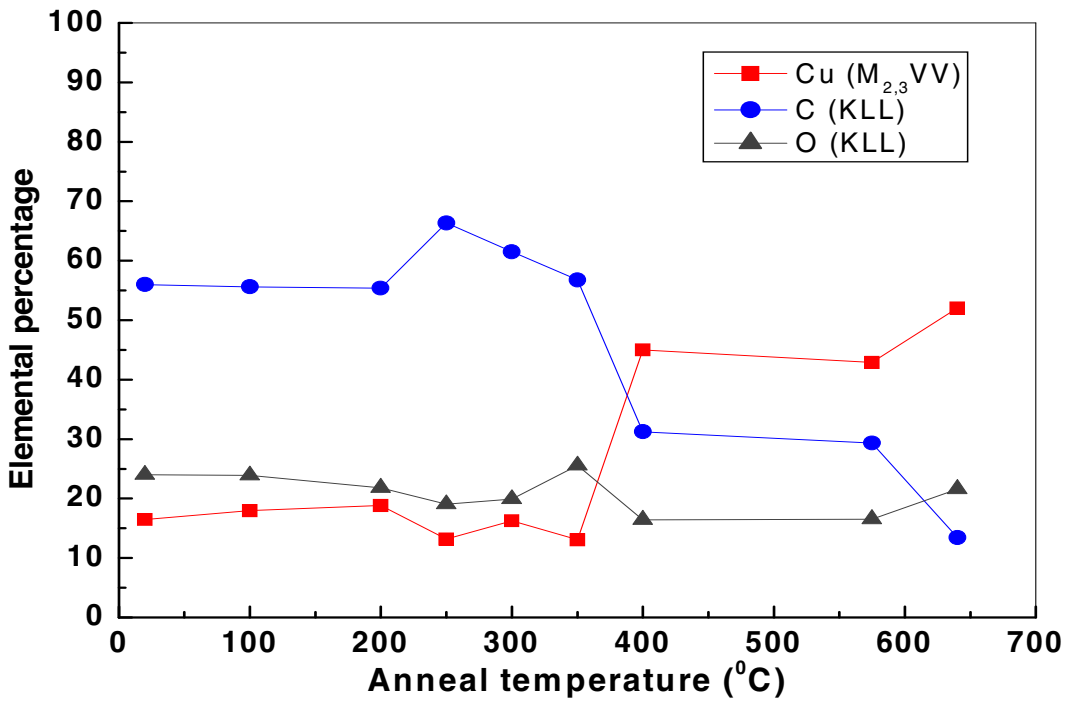

Figure 3.13 Calculated elemental percentage (from EAES data) at near surface of the Cu_2O (12.0) thin film as a function of thermal anneals temperature. The variant sensitivity of the two Auger transitions to the presence of carbonaceous overlayer is underlined.

The EAES data clearly shows that thermal annealing is responsible for the removal of C from the surface but does not provide unambiguous evidence of the Cu content of the top most layer due to the fact that EAES probes several atomic layers below the surface. As discussed above, the PAES data does indicate that the Cu atoms of the Cu_2O are completely covered before annealing and are substantially exposed after annealing. The EAES data strongly suggests the overlayer that was posited based on the PAES results is carbon rich. The fact that there is a substantial EAES signal from Cu before annealing indicates that this overlayer must be thin enough to allow a substantial number of Auger electrons to escape from the Cu_2O surface without losing energy. A

quantitative estimate of the overlayer thickness is derived below from a consideration of the inelastic mean free paths of the electrons emitted in the two observed Cu Auger transitions observed.

The Cu $M_{2,3}VV$ peak to peak intensity observed in the EAES data after annealing at 400 ^{0}C is ~125% larger than the corresponding intensity before annealing. This increase is significantly larger than the corresponding ~33% increase in the Cu LVV peak (but still much less than the ~3000% increase in the Cu $M_{2,3}VV$ peak observed in the PAES data). We note that the relative size of the percent increase in intensity of the Cu LVV (EAES), Cu $M_{2,3}VV$ (EAES), and Cu $M_{2,3}VV$ (PAES) peaks can be explained in terms of the relative probe depth of the three signals if it is assumed that, before annealing, the Cu_2O surface is covered by a thin carbonaceous layer which is removed as a result of annealing to expose the Cu atoms in the top layer. The fact that the increase in the peak to peak intensity of the Cu $M_{2,3}VV$ EAES signal is larger than the increase in the Cu LVV EAES signal (see Figure 3.14) is consistent with the longer mean free path of the higher energy electrons which make up the LVV signal.

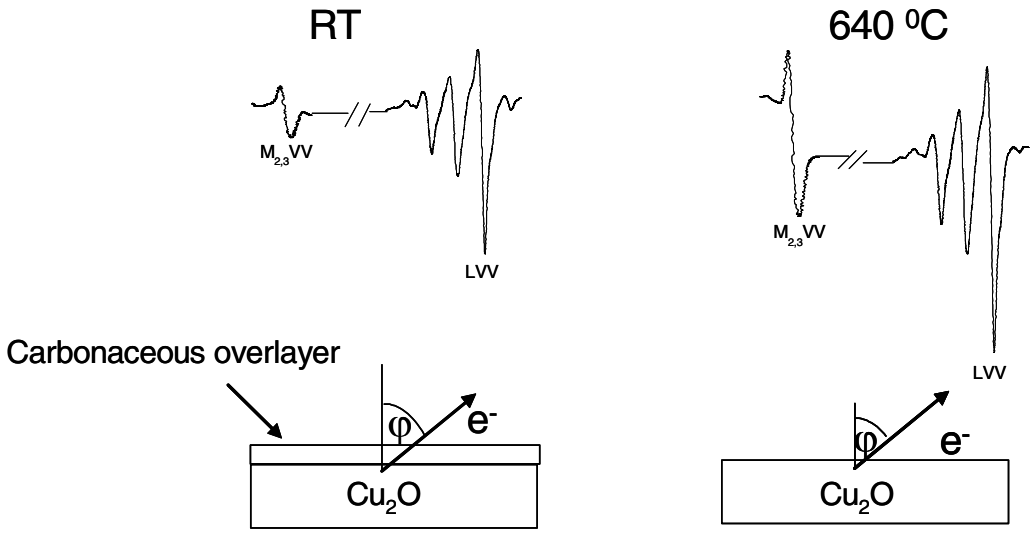

Figure 3.14 Schematic diagram of the path of the outgoing Auger electrons from Cu atoms in the substrate before and after thermal stripping of the carbonaceous overlayer. The EAES spectra shows the change in peak to peak height of Cu($M_{2,3}VV$) and Cu(LVV) Auger transitions before and after annealing at 640 ^{0}C.

Due to the large difference between the inelastic mean free paths of Auger electrons emitted from the high energy LVV (920 eV) and low energy $M_{2,3}VV$ (60 eV) Cu peaks, it is possible to make a quantitative estimate an overlayer covering a Cu containing substrate.[58,59]

3.3.3 Calculation of the overlayer thickness

The intensity of electrons (I) emitted from all depths greater than (d) emitted at an angle (φ) to the surface normal is given by the extended Beer Lambert relationship as follows,

$$I = I_0 \exp(-d / \lambda \cos\varphi) \qquad 3.1$$

where I_0 is the intensity of electrons from an infinitely thick, uniform substrate and λ is the inelastic mean free path of electron in the substrate.

According to the thin overlayer thickness d of carbonaceous material on the Cu-O substrate as shown in figure 3.14, the equation (3.1) can be rewritten for the intensity of the electrons due to Cu M $_{2,3}$ VV and Cu LVV Auger transition at different temperature

$$I_{T,60eV} = I_{0,60eV} \exp(-d / \lambda_{60eV} \cos\varphi) \qquad 3.2$$

$$I_{T,920eV} = I_{0,920eV} \exp(-d / \lambda_{920eV} \cos\varphi) \qquad 3.3$$

Taking the ratio of equations (3.2) and (3.3),

$$\frac{I_{T,60eV}}{I_{T,920eV}} = \left(\frac{I_{0,60eV}}{I_{0,920eV}}\right)\left(\frac{\exp(-d / \lambda_{60eV} \cos\varphi)}{\exp(-d / \lambda_{920eV} \cos\varphi)}\right) \qquad 3.4$$

By rearranging equation (3.4) the thickness d in terms of the ratio of the Cu $M_{2,3}VV$ and LVV EAES intensities can written as follows;

$$d = \frac{\lambda_{920eV}\lambda_{60eV}}{\lambda_{920eV} - \lambda_{60eV}} \cos\varphi \ln\left(\frac{I_{0,60eV} / I_{0,920eV}}{I_{T,60eV} / I_{T,920eV}}\right) \qquad 3.5$$

where λ_{60} and λ_{920} are the mean free path of electrons emitted in the Cu $M_{2,3}VV$ and LVV Auger transitions respectively, $I_{0,60} / I_{0,920}$ is a constant representing the ratio of Auger intensities in the absence of an overlayer, $I_{T,60} / I_{T,920}$ is the measured ratio of Auger intensities at a temperature T and φ is the escape angle of the electrons with respect to the surface normal. In our calculations, we assumed that the Cu_2O surface was covered by a uniform carbonaceous layer of thickness d (see Figure 3.15) and the

carbonaceous overlayer was homogenous-clearly oversimplification of the real situation. The values of the constants λ_{60} and λ_{920} were taken to be 5 Å and 25 Å respectively based upon the values of the mean free path listed for C in reference 59 and φ was taken to be the 42.30^0 average acceptance angle of the cylindrical mirror energy analyzer used in the EAES measurements.

The value of the constant $I_{0,60}$ / $I_{0,920}$ was set equal to intensity ratio, $I_{640,60}$ / $I_{640,920}$, obtained after annealing at 640 ^{0}C based upon the PAES results which indicated that the overlayer had been largely removed by that temperature. Figure 3.15 shows a plot the film thickness d as a function of annealing temperature calculated using eq. 3.5 and the EAES data (shown in part in Figure 4 panel c) for the Cu_2O sample grown at pH 12. We note that the PAES measurements were critical in establishing that there was an initial overlayer and that it was substantially removed by annealing, two facts that were used in developing the model described above which was used to estimate of the layer thickness.

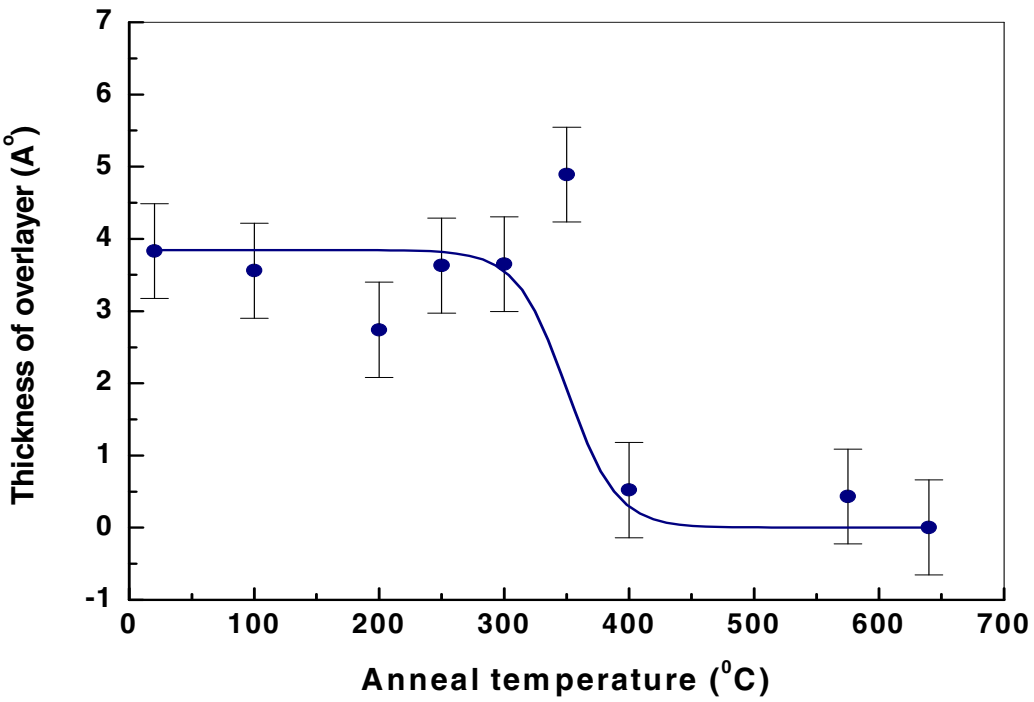

Figure 3.15 Thickness of the carbonaceous overlayer on Cu_2O (12.0) film (see eqn. 1) as a function of thermal anneal temperatures. The solid sigmoidal curve is a Boltzmann function that was fit to the data as a guide to the eye.

Finally, figure 3.16 contrasts the differing analytical sensitivity of the two types of Auger electron spectroscopies, PAES and EAES, to the topmost atomic layers of the sampled Cu_2O surface. To probe this, the Cu $M_{2,3}VV$ Auger transition was considered and the ratio of the signal intensity for the sample subjected to a given anneal temperature over the corresponding value at room temperature, was plotted as a function of the anneal temperature (Figure 3.16). The Cu $M_{2,3}VV$ EAES signal intensity ratio is relatively invariant up to ~350 ^{0}C for reasons discussed earlier. On the other hand, the PAES signal counterpart starts its growth at ~100 ^{0}C (c.f., Figure 3.11) and is amplified (relative to the EAES signal) by approximately an order of magnitude at the

higher thermal anneal temperatures. Clearly, the masking effect of the C overlayer on the Auger signal for Cu (Figure 3.14) is much less of a factor in EAES unlike in the PAES case, underlining the variant spatial origins of the Auger electrons in the two cases. While the contrast shown in Figure 3.16 pertains to the Cu_2O (12.0) sample case, similar trends also manifest in the other two PAES cases, albeit to varying degrees.

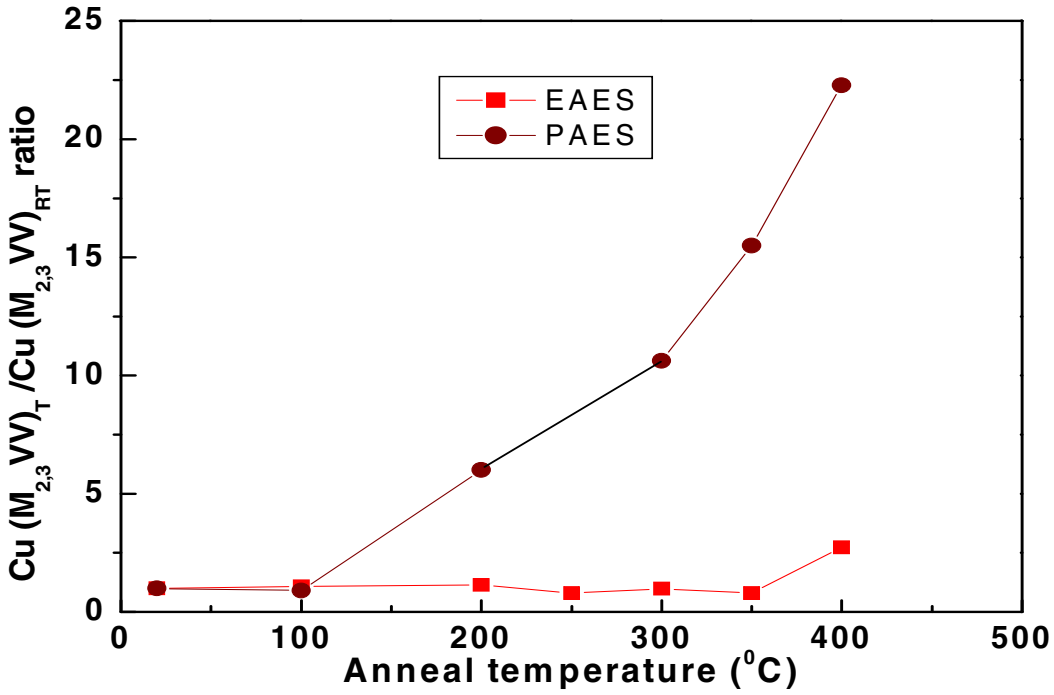

Figure 3.16 Contrast of the sensitivity of PAES and EAES to changes in the topmost atomic layers of Cu_2O (12.0) as a function of the thermal anneal temperature (see text).

Finally, this C overlayer is both transparent and to light as well as electronically conductive. Thus, electrodeposited and thermally annealed Cu_2O films show cathodic photocurrents under band excitation of the oxides. Similarly well-behaved

voltammograms were obtained in background electrolytes in the dark (flat and showing good rectification in the reverse bias mode) with no manifestation of significant ohmic resistance effects.

3.3.4 Conclusions

We have reported the results of PAES and EAES measurements of the top layer and near surface elemental composition of electrodeposited Cu_2O surfaces which have been subjected to a series of anneals in vacuum at increasing temperature. The intensity of the PAES signal from Cu increases dramatically upon annealing from ~1% of the signal from a clean single crystal Cu standard before annealing to ~30% after annealing at 400 ^{0}C for 2 min in vacuum. In light of the fact that PAES selectively probes the top most atomic layer due to the trapping of positrons in an image-potential state before annihilation, these results provide strong evidence that the Cu_2O surface was initially covered by a complete overlayer before annealing and that this overlayer is substantially removed after annealing in vacuum. In contrast to the large changes seen in the PAES intensities from Cu, the changes in the EAES spectra are relatively small. The EAES intensity associated with the Cu LVV transition increased from ~40% of the clean Cu value to ~50% consistent with the hypothesis that the initial overlayer was thin enough to transmit most of the 918 eV Cu LVV electrons. The percent change upon annealing in the $M_{2,3}VV$ Cu EAES signal was about 2 times larger that that for the LVV peak which is consistent with the greater attenuation of the lower energy $M_{2,3}VV$ electrons in the initial overlayer. The PAES results were used together with the EAES results to

provide a quantitative estimate the thickness of the overlayer as function of annealing temperature yielding an estimate of ~4 Å for overlayer thickness before was annealing. The results of this study clearly demonstrate the utility of PAES as a complement to conventional EAES the study of Cu_2O surfaces due to its ability to selectively sample to top most atomic layer.

CHAPTER 4

VACUUM ANNEALED PREVOIUSL OXIDIZED Cu (100)

4.1 Introduction

This chapter describes the effect of temperature on the stability of the top layer of oxide on a Cu(100) using Positron annihilation induced Auger electron Spectroscopy. The understanding of metals oxidation is of both fundamental and practical importance in a wide variety of applications from corrosion to catalysis. Cu has received much attention as its oxide is used in vast range of application including heterogeneous catalysis, high temperature superconductors and metal corrosion. Previous investigators have used oxides on pure transition metal as a model system to understand oxidation kinetics experimentally and theoretically.[60-66] The Cabrera –Mott Model[67] is the most widely used theory to describe the formation of the metal oxides and assumes a uniform oxide growth. J Yang and colleagues[68] have used modified JOHNSON-MEHL-AVRAMI-KOHLMOGOROV (JMAC)[69] theory to explain the oxidation mechanism. They have applied this theory to study the intermediate mechanism of the oxidation using TEM as the probe.[68] The system used was a micrometer thick Cu (001) film thick enough to be treated as a bulk material but thin enough to be studied with a TEM. They concluded that oxide islands nucleate and then coalesce with time followed by reduction

in the growth rate.[70] TEM is known to sample more than the surface layer. Also the high energy of the probe can affect the oxidation.[68]

Motivated in part by this and other limitations of the electron probes, we have studied the sample using PAES. In our case sample thickness is not a limitation. Hence the oxidation in our system occurs on bulk sample and not on thin films. PAES has been shown to selectively sample the topmost atomic layer. This is very critical because the oxidation is a surface mediated process.[67] It has been shown theoretically that oxygen on Cu surface can adsorb at on-surface as well as subsurface sites.[68] Yang et al. found that, depending on oxygen coverage, subsurface sites may be energetically favorable than the on-surface site.[62] PAES has been shown to be sensitive to submonolayer coverage of oxygen and is hence ideal for studying the initial stages of oxidation.[21-24] The oxidized surface was sputter etched and PAES was used to probe the near surface region. The same surfaces have been studied with electron induced Auger electron spectroscopy and the results have been compared to that of PAES. Since the signal in case of EAES comes from near surface region as compared to the surface region sampled by PAES, the resulting spectra can be compared to shed more light on presence of oxygen. The formation of oxide the metal has been done with different methods as described in chapter 3. In our experiment the oxide layer was formed by exposing the surface to a low pressure oxygen atmosphere while maintaining a high substrate temperature (<600^{o}C).

4.2 Experimental set up

A Cu (100) single crystal (purity 99.999%) was used as a substrate. The sample is 10 mm in diameter and 1mm in thickness was purchased from the Matech Company. It was polished on one side with a roughness<0.3 micron. Before mounting to the sample holder, Cu single crystal was degreased ultrasonically in acetone and rinsed with ethyl alcohol and deionized water. The sample was then mounted on the sample holder, rinsed again with deionized water and dried using nitrogen gas (N_2). The base pressure of the PAES system was maintained at 1.0 x 10^{-9} Torr. The Cu (100) was cleaned in the vacuum chamber with several sputtering and low temperature annealing (at 300 ^{0}C) cycles in order to remove impurity from the sample surface prior to the oxidation process. Oxidation of the Cu (100) surface to form a Cu_2O layer was performed as discussed in the ref 71 and 72. Figure 4.1 shows the phase diagram of the Cu-Cu_xO system. The annealing temperature in degrees is represented by the X axis and pressure in the unit of Torr is represented by Y axis. It may be seen from the phase diagram that surface oxidation may be performed at substrate temperature < 1100 ^{0}C and oxygen partial pressures less than 0.1 Torr. Copper forms two thermodynamically stable oxides Cu_2O and CuO. In our experiment, a pressure of 5.0 x 10^{-4} Torr was selected as the oxygen (high purity 99.999%) partial pressure and the substrate temperature was maintained at ~ 590-595 ^{0}C temperature to obtain only Cu_2O layer on Cu(100) surface. The reason for selecting the above parameters including relative high substrate temperature is that previous attempts at low temperatures did not give us good results. After oxidation the sample substrate was annealed to a sequence of isochronal annealing

cycles in vacuum at increasing temperature, holding the sample at each different temperature for 2 minutes. PAES spectra were acquired at room temperature after each thermal anneal cycle. The sequence of oxidation and anneal cycle was repeated three times in order to check the reproducibility. Before each PAES spectra NaI gamma ray spectrum was obtained in order to calculate the positronium (Ps) fraction.

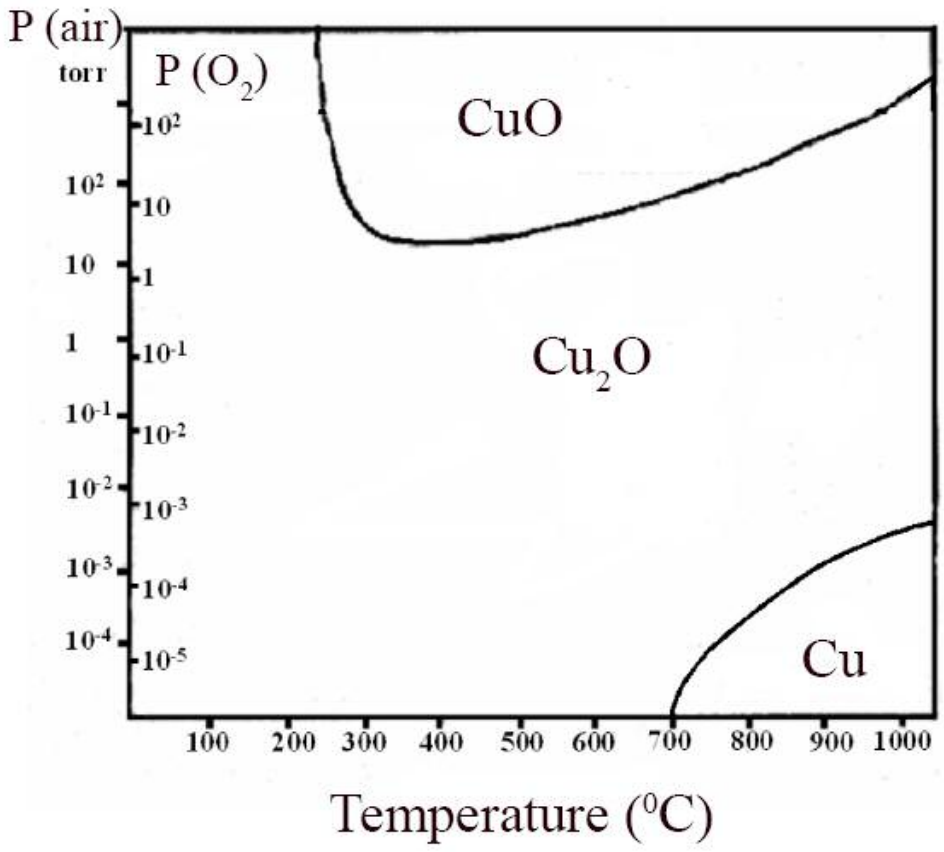

Figure 4.1 Phase diagram of Cu-Cu_xO system.[71,72]

4.3 PAES results on vacuum annealed previously oxidized Cu(100).

The figure 4.2 shows a comparison of PAES spectra from clean Cu surface and the oxidized surface. The PAES spectrum from clean Cu is shown in figure 4.2 (a). two peaks may be observed at ~60 eV and ~103 eV corresponding to the Cu ($M_{2,3}VV$) and Cu (M_1VV) Auger transition respectively. The PAES spectra obtained from oxidized clean Cu(100) are shown in figure 4.2 (b). These results indicate that the intensity of the Cu ($M_{2,3}VV$) peak is reduced by ~93%. The inset of figure 4.2 shows the higer energy range of the PAES spectra corresponding to the range of the O (KLL) auger transition at ~503eV and it tells clearly that the O (KLL) peak is increased by ~200 %.

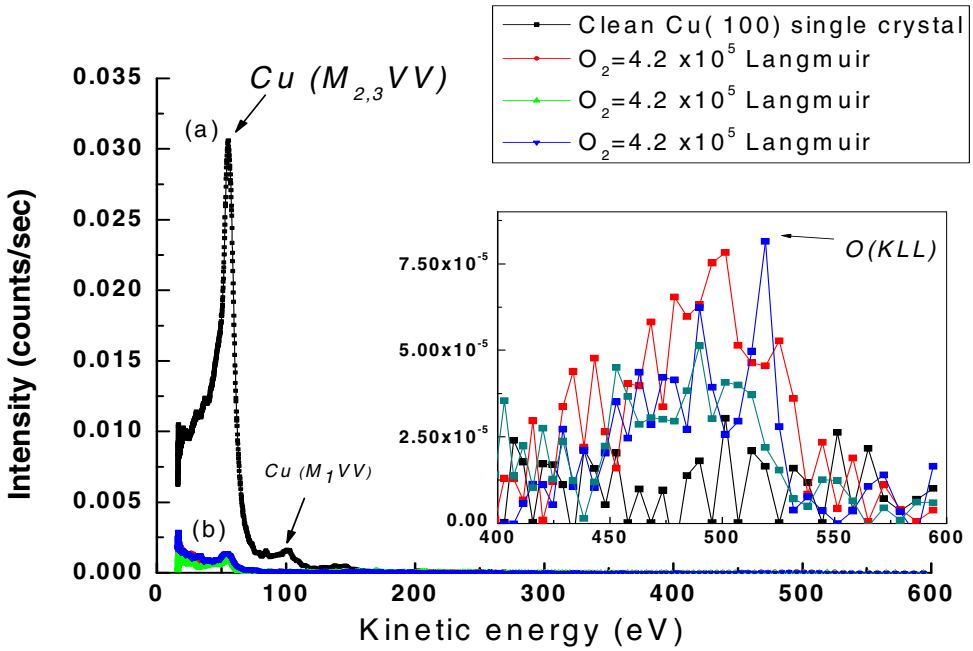

Figure 4.2 PAES spectra of Cu (100) before and after oxidation.

The intensities of Cu ($M_{2,3}VV$) and O(KLL) peak integrals from oxidized Cu(100) as a function of annealing temperature are shown in figure 4.3 (a) and (b) respectively. It may be seen that the Cu peak integral intensity increases steadily during annealing up to 300 ^{0}C and reaches maximum intensity at 300 ^{0}C. Then the Cu PAES intensity decreases as the temperature is increased further. In contrast, the O (KLL) PAES intensity is the lowest at 300 ^{0}C and it starts to increase again as the temperature is increased further. During the experiment the intensity of C (KLL) Auger peak at ~272 eV remains virtually constant. The PAES spectrum obtained after annealing at 300 ^{0}C temperature looks similar to the clean Cu PAES spectrum. The PAES spectra obtained from clean Cu (100) spectra and oxidized Cu (100) after annealing at the temperature 300 ^{0}C are shown in figure 4.4.

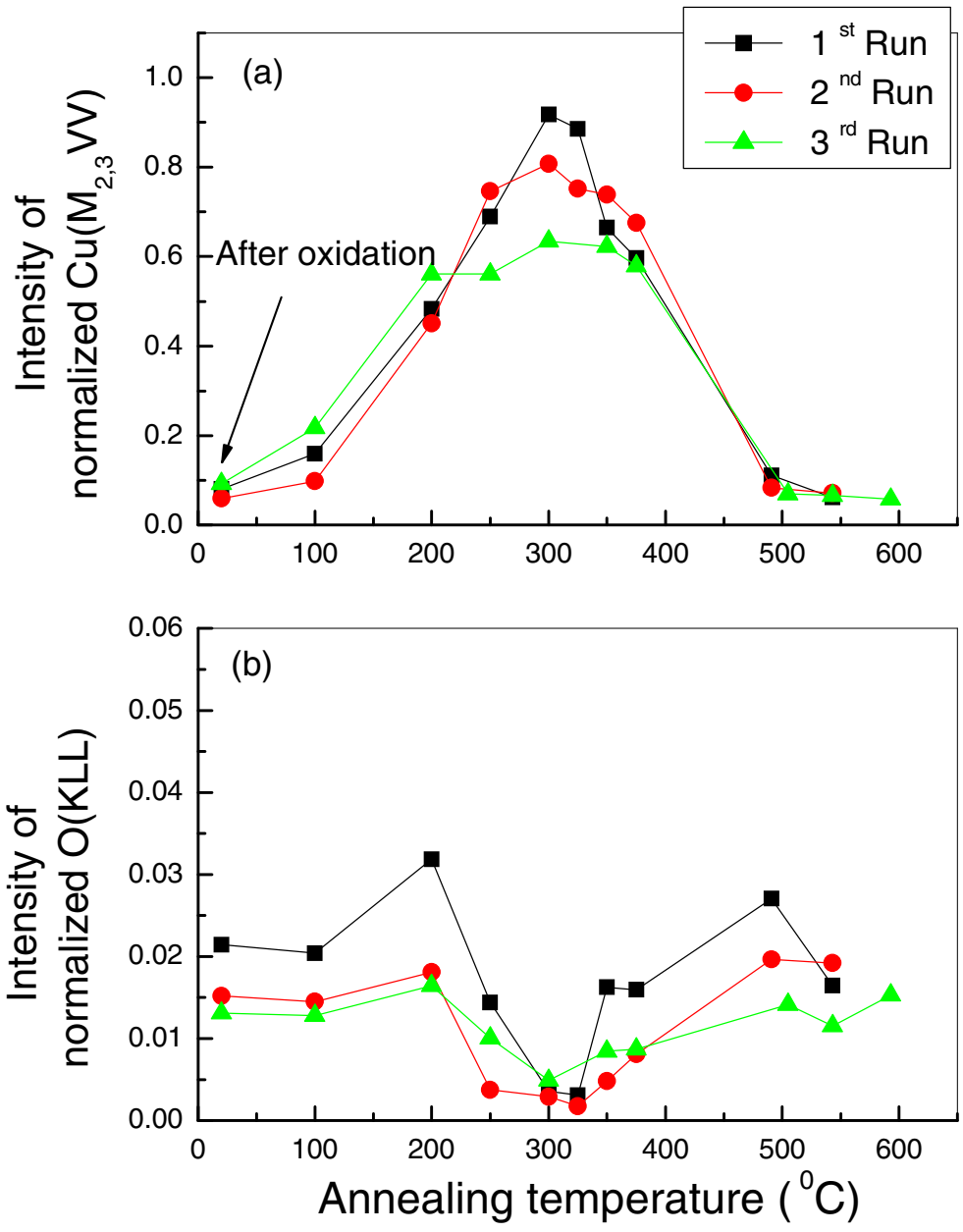

Figure 4.3 PAES Intensity of t (a) Cu ($M_{2,3}VV$) and (b) O (KLL) peak integral of Cu(100) that has been previously oxidized as a function of thermal anneal temperature.

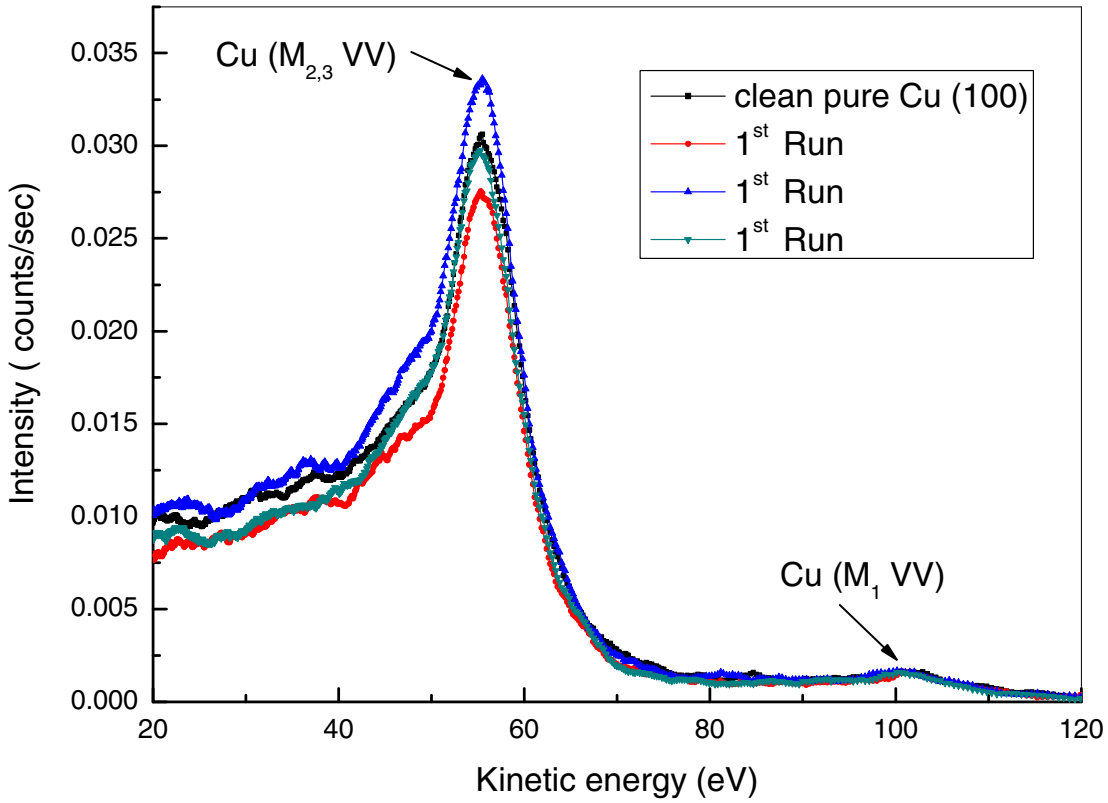

Figure 4.4 Comparison of PAES spectra of Clean Cu (100) with the PAES spectra of previously oxidized surface after thermal anneal at 300 ^{0}C.

Based on these results we posit that after oxidation, a Cu_2O layer is formed on the surface of Cu (100) single crystal in a way such that a layer of oxygen covers the surface of Cu (100). During annealing, O atoms desorb or diffuse into bulk and Cu atoms appear on the surface. Further annealing of the substrate leads to diffuse bulk oxygen to the surface and that causes less PAES intensity (Ref fig. 4.3 (a)). In order to prove the mechanism that we proposed same experiment was done on sputter cleaned previously oxidized Cu (100) single crystal. After the oxidation of Cu (100) with 4.0 x

10^5 L dose of oxygen, the oxide layer was removed by ion beam sputtering in Ar_2 environment with partial pressure of 5.0 x 10^{-5} Torr and ion beam acceleration voltage of 3 kV. Then the same vacuum annealing experiment was performed two times on Cu(100) for reproducibility. After sputtering, peak intensity of Cu ($M_{2,3}VV$) was reduced by ~42 % with respect to the intensity obtained from Cu(100) substrate before the oxidation. The calculated Ps fraction from the sputtered surface shows an increase in Ps fraction by 55% as compared to that of from the surface before oxidation. The less peak intensity and the higher Ps fraction suggest that the sputtering causes increase in the surface roughness of Cu(100) surface and leads to the less probability of positron annihilation with surface electrons. The change in Cu peak integral intensity which corresponds to ($M_{2,3}VV$) Auger transition as a function of thermal anneal temperature is shown in figure 4.5. The intensity of Cu peak integral is increased by ~14% by annealing in the temperature range of 20 ^{0}C to 375 ^{0}C. Further annealing causes the intensity to drop by ~77% at 490 ^{0}C. The peak intensity of oxidized Cu and sputtered previously oxidized surface have the same intensity at vacuum annealing temperature of ~490 ^{0}C.

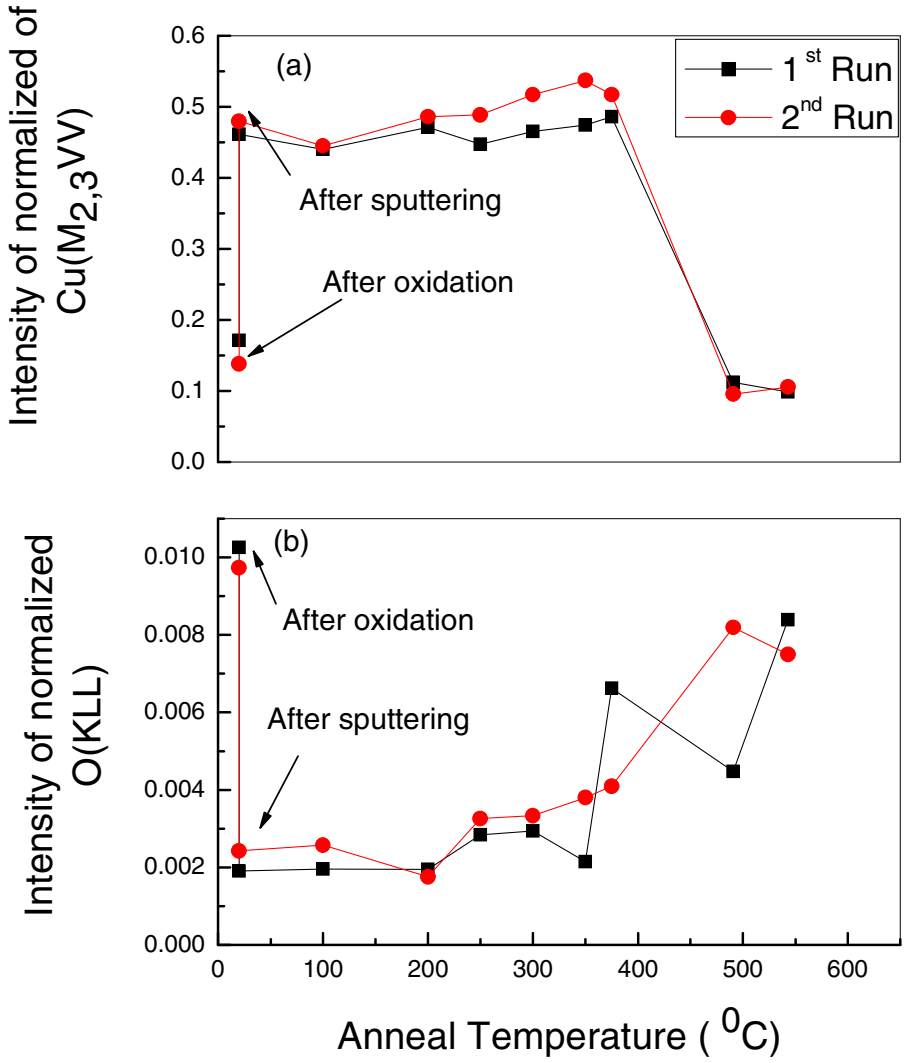

Figure 4.5 PAES Intensity of t (a) Cu ($M_{2,3}VV$) and (b) O (KLL) peak integral of Cu(100) that has been previously oxidized and sputtered as a function of thermal anneal temperature.

4.4 EAES results on vacuum annealed previously oxidized Cu(100).

Vacuum annealing on previously oxidized Cu(100) was also investigated using electron induced Auger electron spectroscopy (EAES). The incident electron beam was selected as 3 keV and base pressure of the vacuum chamber was maintained at ~8.0×10^{-10} Torr during data acquisition. As described in previous section Cu(100) was cleaned with different sputtering and annealing cycle until obtained the clean spectra. For reproducibility, the experiment was performed three times. The set of data was obtained with elapsed time between anneal temperature similar to that of PAES measurements. The EAES spectra were obtained with single pass cylindrical mirror analyzer (Model PHI 10-155) at three different positions on the sample for each isochronal annealing cycle. The same oxidation and annealing sequence was used as in the PAES measurement described in the previous section. EAES spectra were obtained at room temperature after annealing at different elevated temperature for 2 minutes. The EAES spectrum of clean surface of Cu(100) before oxidation shows ~80.88 % of Cu , ~14.19 % of C and 4.92 % of O considering peak to peak height of Cu($M_{2,3}VV$) at ~63 eV, C(KLL) at ~273 eV and O(KLL) at ~503 eV Auger transitions respectively. On the other hand ~ 88.62% of Cu, ~ 8.44 % of C and ~2.92 % of O show on the surface by considering peak to peak height of Cu (LVV) at ~920 eV with C(KLL) and O(KLL) at ~273 eV and ~503 eV respectively.

Figure 4.6 shows EAES profiles (*dI/dE vs E*) of oxidized Cu(100) before and after thermal anneal at 100, 250, 350 and 629 ^{0}C. According to EAES spectra, Cu and O on the surface of Cu(100) after oxidation and Cu peaks at ~63eV and ~920 eV stay

almost the same during annealing. C signal appears on the surface after annealing at 100 ^{0}C and it disappears after annealing 250 ^{0}C while O signal intensity remains constant with anneal temperature.

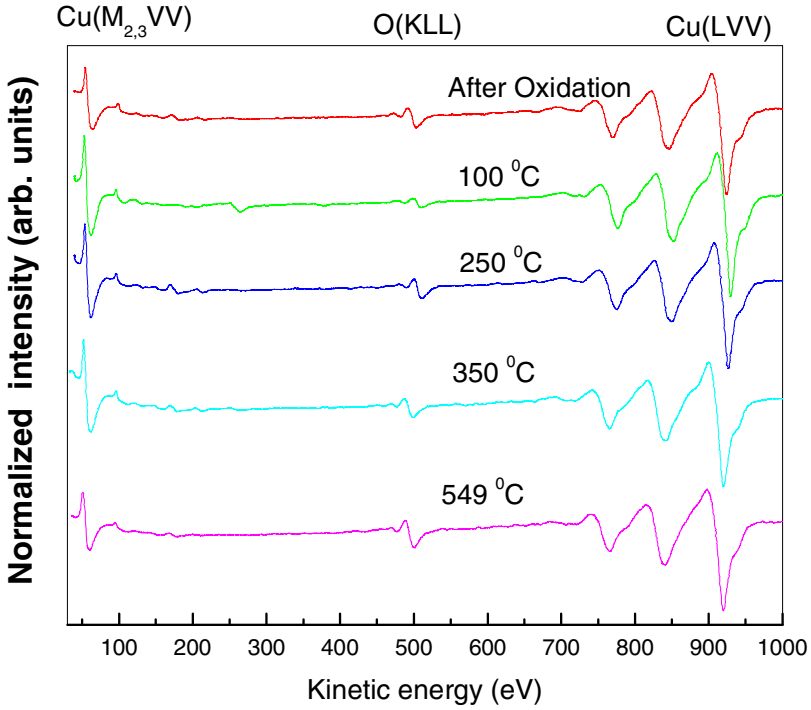

Figure 4.6 EAES profiles of oxidized Cu (100) before and after thermal anneal at 100, 250, 350 and 549 ^{0}C.

Figures 4.7 and 4.8 show calculated elemental percentage of Cu, C and O on the Cu(100) as a function of thermal anneal temperature. The peak to peak height of Cu ($M_{2,3}VV$) Auger derivative peak along with C(KLL) and O(KLL) were considered for calculation of relative elemental percentage in figure 4.7. While peak to peak height of the Cu(LVV) Auger derivative peak along with C(KLL) and O(KLL) were considered for relative elemental percentage shown in figure 4.8. After oxidation of Cu(100),

relative percentage of C is decreased by ~70-75% and O is increased by ~150%. After annealing at 100 ^{0}C for 2 minutes, O percentage is decreased by 50% while C percentage is increased by 275%. Further annealing of sample led to decrease in C percentage on the surface and increase in O. During the entire annealing process Cu percentage almost stays same.

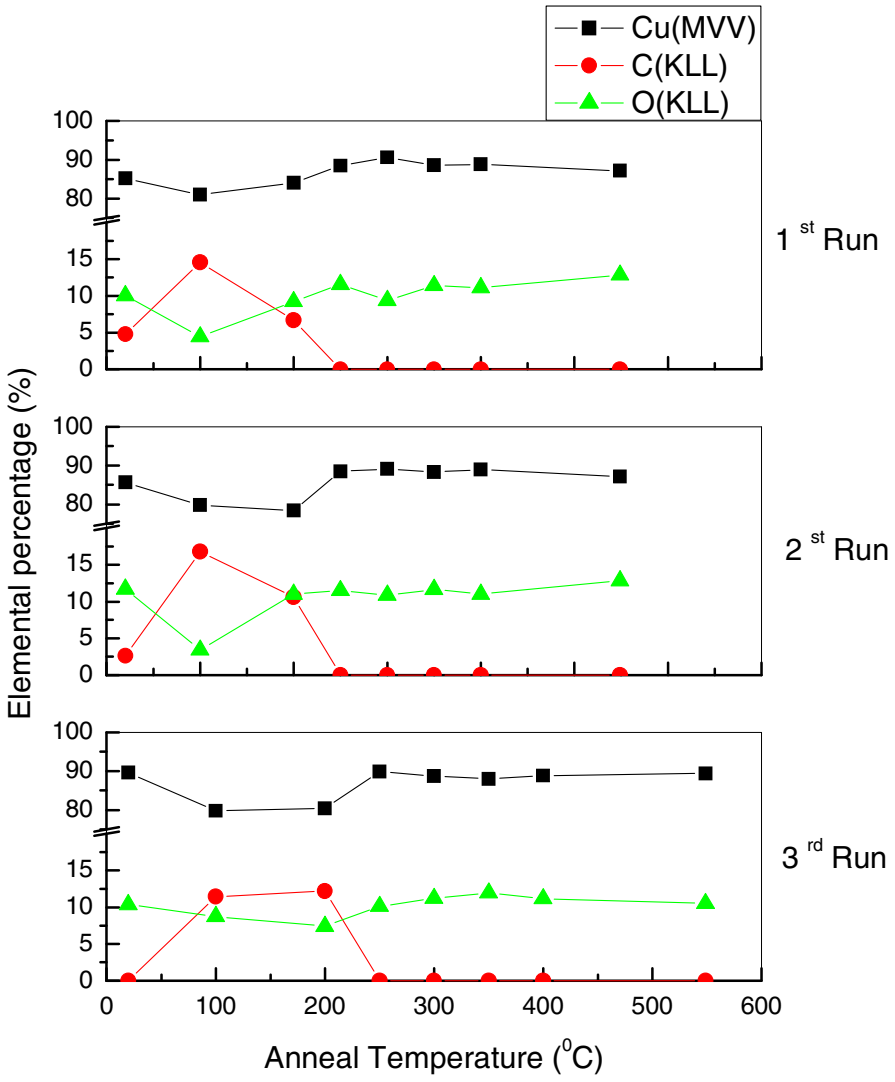

Figure 4.7 Calculated elemental percentage of C, Cu and O on Cu(100) as a function of thermal anneal temperature considering peak to peak height of Cu($M_{2,3}$VV) at ~63eV along with C(KLL) at ~273eV and O(KLL) at ~503eV Auger peak intensity.

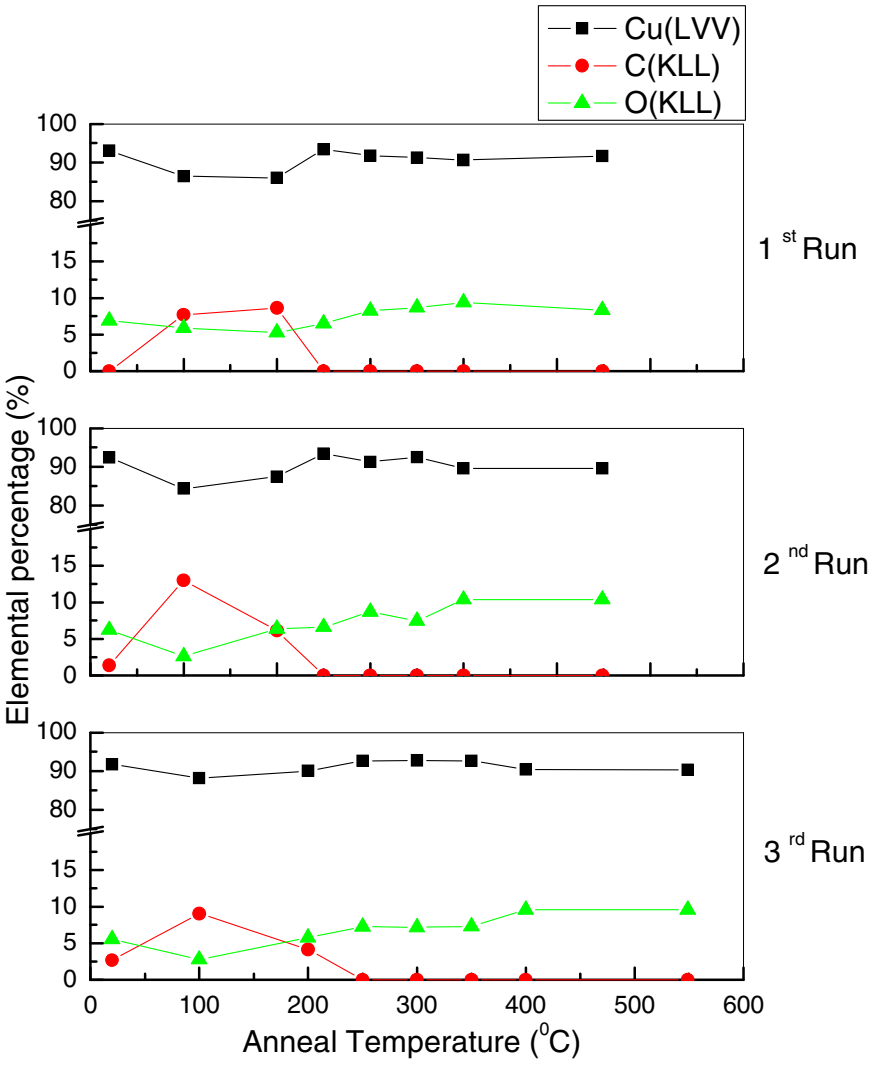

Figure 4.8 Calculated elemental percentage of C, Cu and O on Cu(100) as a function of thermal anneal temperature considering peak to peak height of Cu(LVV) at ~920eV along with C(KLL) at ~273 eV and O(KLL) at ~503eV Auger peak intensity.

4.5 Positronium fraction

In chapter one, the two ways of positronium (Ps) formation at the metal surface was discussed. In this section a method of Ps fraction calculation will be discussed. Positronium may be determined by the gamma ray spectrum obtained by NaI detector during PAES experiment. Figure 4.9 shows the gamma ray spectrum as a function of channel number that obtained during positron annihilation experiment on Cu(100). There are two peaks on the spectrum. Peak at channel ~552 corresponds to energy of 511 keV results from annihilation via two gamma rays (called a photo peak) when positrons in the surface state (p-Ps). The peak corresponds to energy less that 511 keV is a result of gamma ray produced via three gamma (o-Ps) and Compton scattering of 511 keV gamma rays.

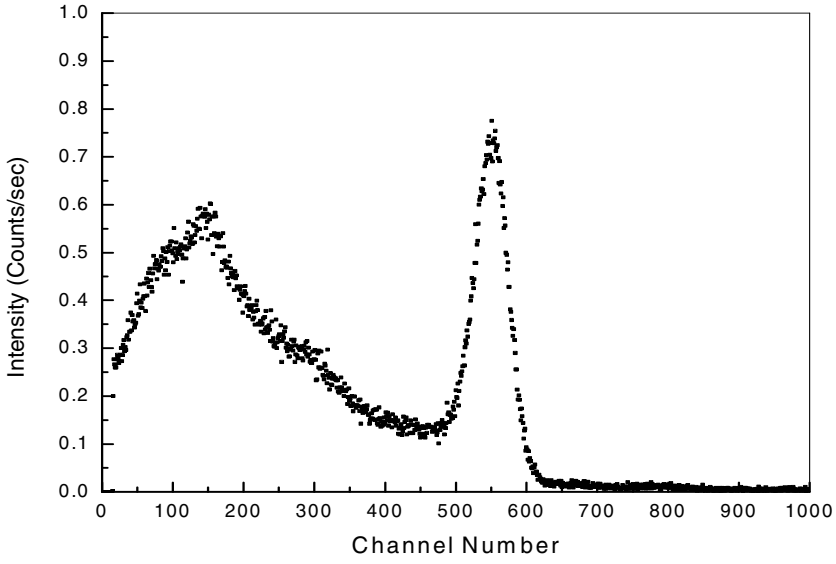

Figure 4.9 Gamma ray spectrum as a function of channel number.

The Ps fraction (f_{ps}) can be related to gamma ray spectrum by considering the total number of gamma ray counts per unit time (T) and the total number of 511keV gamma ray counts per unit time (P). Considering the Ps fraction, T, and P, following equations[69] can be written.

$$T = f_{Ps}T_1 + (1 - f_{Ps})T_0 \qquad 4.1$$

$$P = f_{Ps}P_1 + (1 - f_{Ps})P_0 \qquad 4.2$$

Where subscript 1 and 0 refer to complete Ps formation (f_{Ps} =1) and no Ps formation (f_{Ps} =0) respectively. P and T are the measured peak and total counts of the spectra from which f_{Ps} is to be measured.

Considering equations 4.1, and 4.2, the ratio R is defined by assuming no dependence on the positron beam strength while R_1 and R_0 are ratios for 100% and 0% Ps fraction respectively.

$$R = \frac{(T - P)}{P} \qquad 4.3$$

$$R_1 = \frac{(T_1 - P_1)}{P_1} \qquad 4.4$$

$$R_0 = \frac{(T_0 - P_0)}{P_0} \qquad 4.5$$

Hence the Ps fraction f_{Ps} can be determined by the following equation.

$$f_{Ps} = \left[1 + \frac{P_1}{P_0}\left(\frac{R_1 - R}{R - R_0}\right)\right]^{-1} \qquad 4.6$$

In order to calculate the Ps fraction using equation (4.6) the three quantities R_0, R_1 and P_1/P_0 must be determined experimentally. The quantities R_1 and P_1 are pertain to the spectrum for 100% Ps formation, which can be obtained by heating the sample at high temperature such that the thermal desorption approaches 100%. Whereas R_0 and P_0 are pertain to the spectrum resulting from 0% Ps emission, which can be obtained by applying a high bias voltage to the sample such that the positrons are trapped in the bulk. We have considered f_{Ps}=0.9 for 100% Ps formation and f_{Ps}=0.52 for 0% Ps formation[73] for Cu(100) sample in order to calculate unknown parameters P_1, T_1, P_0 and T_0 respectively. In our case the gamma ray spectra were obtained at room temperature after annealing at elevated temperature for 2 minutes of previously oxidized Cu(100).

4.6 Core hole annihilation probability using PAES coincident spectrum.

The core hole annihilation probability (ρ) is experimentally determined from the total number of Auger electrons generated by positron annihilation per unit time within a solid angle ($\Omega_S = 4\pi$) at the sample surface (N_A) and the total number of positrons localized at the surface state (N_{SS}) according to following equation.

$$\rho = \frac{N_A}{N_{SS}} \qquad 4.7$$

The measured number of coincidence events yielding Auger electrons per unit time ($N_{A-Coin}(E)$) is related to the core-hole annihilation probability, the number of positrons

per unit time at the surface ($N_{e^+(\exp)}(E)$), and fraction of positrons that contribute to annihilation ($f_{ss} = (1 - f_{ps})$) by following equation.

$$N_{A-coin}(E) = N_{e^+(\exp)}(E).(1 - f_{Ps}).\rho.\Omega_A.\varepsilon_{BaF_2}.\varepsilon_{MCP}.T.\eta(E) \qquad 4.8$$

Where ε_{BaF_2} is the BaF_2 detector efficiency for two 511 keV gamma ray emission and ε_{MCP} is the microchannel plate detector efficiency for electrons. T is the transmission probability of Auger electron traversing the surface layer(s) and Ω_A is the solid angle subtended by the microchannel plate which equals to 2π. The quantity $\eta(E)$ is the electron transport efficiency of electron from sample to MCP. Ps fraction is defined as the fraction of incident positrons which form positronium.

The measured number of secondary electron per unit time $N_{\sec}(E)$ is calculated from following equation

$$N_{\sec}(E) = N_{e^+(\sec)}(E).\delta(E).\Omega_S.\varepsilon_{MCP}.\varepsilon_{BaF_2}.\eta(E) \qquad 4.9$$

$N_{e^+(\sec)}(E)$ is the number of positrons that generate secondary electrons per unit time at the surface, $\delta(E)$ the secondary electron yield at a specific energy and Ω_S solid angle subtended by surface. Considering the equations (4.8) and (4.9), the annihilation probability can be determined as shown in equation (4.10).

$$\rho = \frac{(N_{A-Coin}(E)).\delta(E).(\Omega_S / \Omega_A).N_{e^+(\sec)}(E) / N_{e^+(\exp)}(E)}{(N_{\sec}(E)).(1 - f_{Ps}).T} \qquad 4.10$$

The secondary electron yield (δ) of Cu Auger peak at 60 eV is calculated using the universal curve of secondary electron production, which is given by the following equation.[70]

$$\delta(E_{PE}) = 1.28.(\delta^m).\left(\frac{E_{PE}}{E_{PE}^m}\right)^{-0.67}.\left(1-\exp(1.614-\left(\frac{E_{PE}}{E_{PE}^m}\right)^{1.67})\right) \qquad 4.11$$

Where E_{PE} is the energy of primary incident beam. E_{PE}^m is the primary beam energy which corresponds to maximum secondary electron yield δ^m. Figure 4.10 shows the schematic profile of secondary electron yield as a function of primary incident beam energy and figure 4.11 shows the generated secondary electron yield $\delta(E_{PE})$ curve as a function of energy of primary beam energy considering $\delta^m = 1.53$ for $E_{PE}^m = 400eV$.[74]

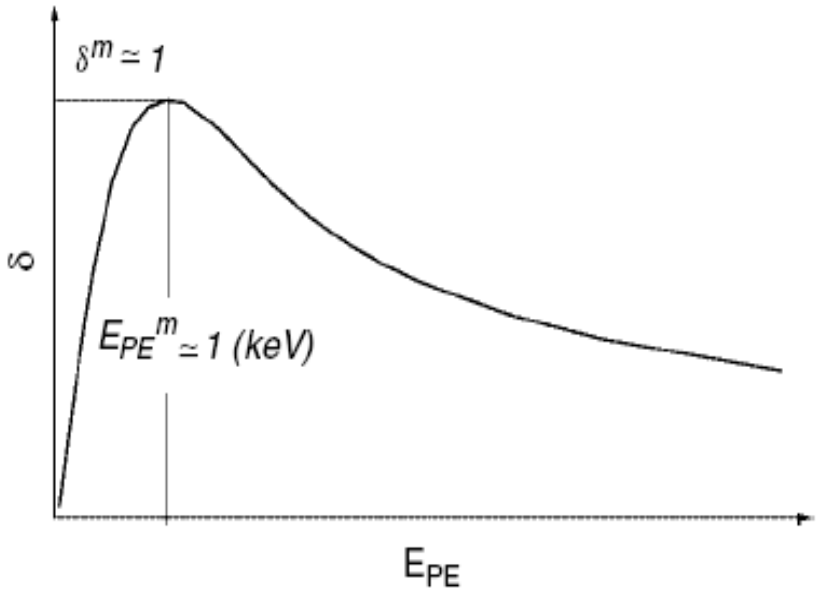

Figure 4.10 Schematic profile of secondary electron yield as a function of primary incident beam energy.[74]

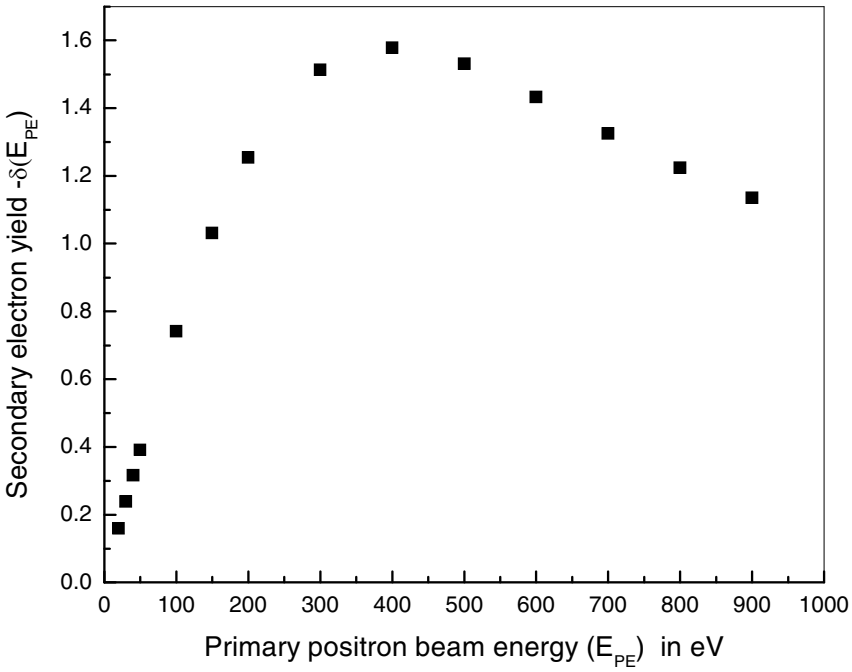

Figure 4.11 The secondary electron yield as a function of primary incident beam energy with $\delta^m = 1.53$ for $E_{PE}^m = 400eV$.

Based on figure 4.10, the secondary electron yield for energy ~58 eV would be 0.45.

The experimental core-hole annihilation probability (ρ) of Cu 3p ($M_{2,3}VV$) was calculated, which is 2.74% using equation (4.10). This result may be compared to the theoretical value of 3.02% calculated by Jensen and Weiss[75] which is close to the value obtained experimentally. However annihilation probability of Cu-3p on oxidized Cu(100) surface is ~0.25% . The core-hole annihilation probability of Cu-3p and O-1s of positrons trapped in the surface state of Cu (100) that has been previously oxidized is plotted as a function of thermal anneal temperature in figure 4.12 (a) and (b) respectively. The core-hole annihilation probabilities of the Cu-3p and O-1s levels for a

Cu (100) surface that has been previously oxidized Cu (100), and sputtered before it is annealed are plotted as a function of thermal anneal temperature in Figure 4.13 (panels (a) and (b) show the annihilation probabilities for the Cu-3p and O-1s levels respectively). In this case Cu-3p annihilation probability is increased by ~250 % while O-1s annihilation probability is decreased by 80% after sputtering previously oxidized sample.

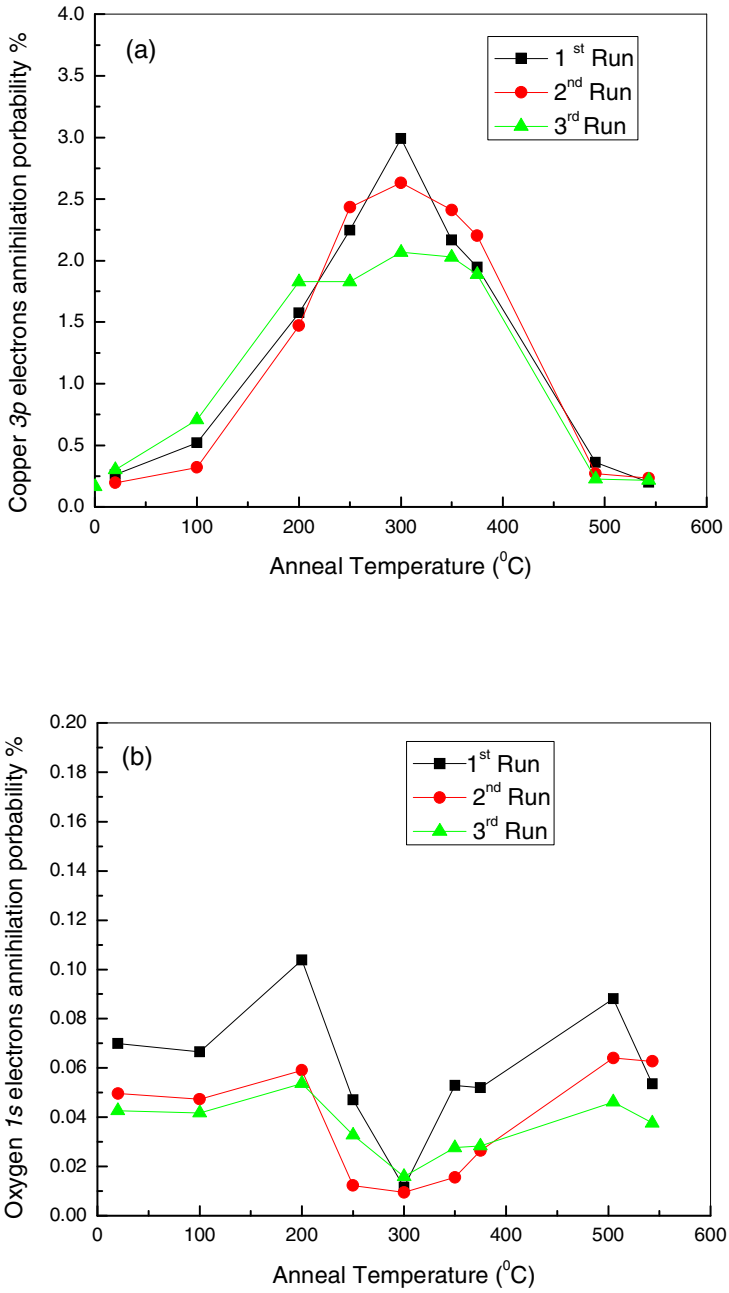

Figure 4.12 Core-hole annihilation probability of (a) Cu-3p and (b) O-1s of positrons trapped in the surface state of Cu (100) that has been previously oxidized as a function of thermal anneal temperature.

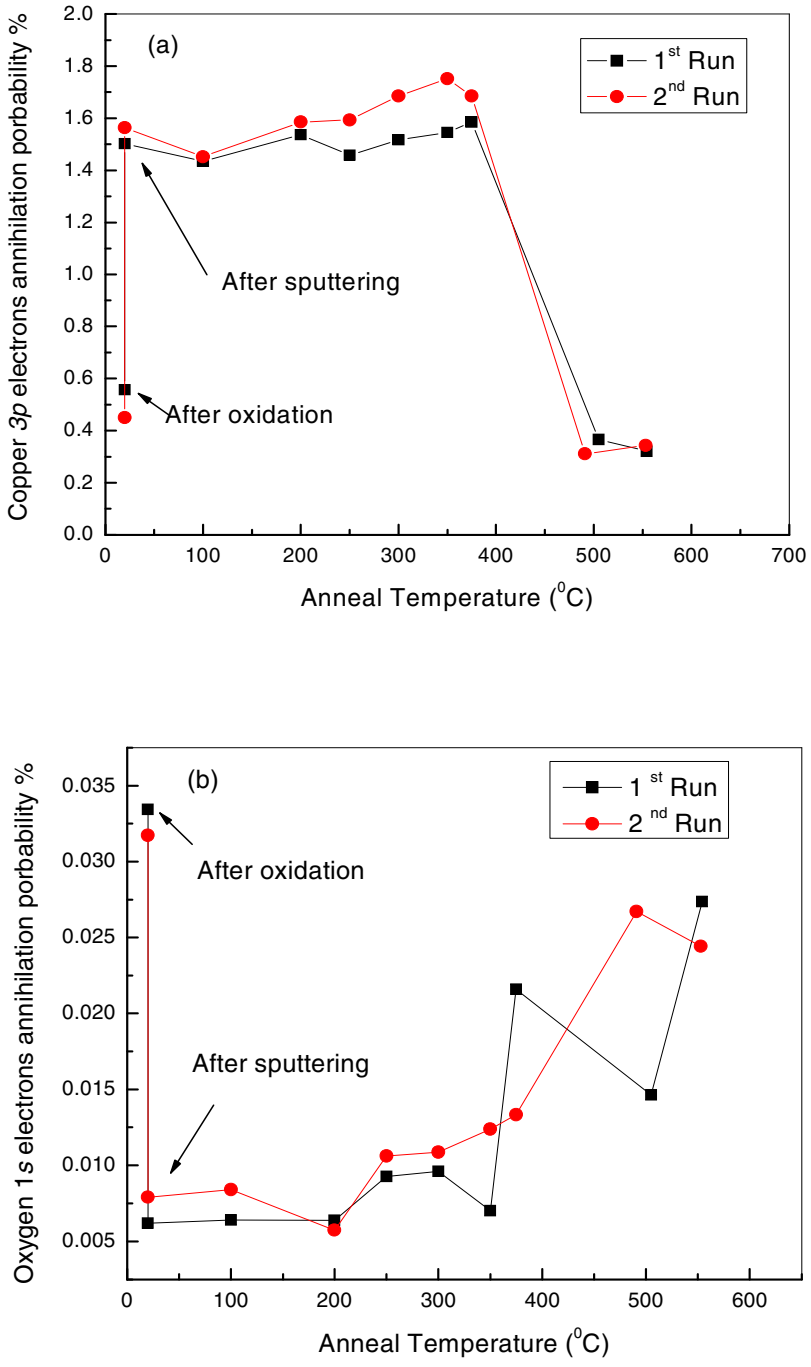

Figure 4.13 Core-hole annihilation probabilities of (a) Cu-3p and (b) O-1s levels for a Cu (100) surface that has been previously oxidized Cu (100), and sputtered before it is annealed as a function of thermal anneal temperature.

CHAPTER 5

DISCUSSION

5.1 Summary

In this dissertation, Time of Flight Positron Annihilation induced Auger Electron Spectroscopy (TOF-PAES) was applied in the study of the top layer of transition metal oxides. This work has yielded detailed information on thermal stability and reduction of Cu_2O layer on different substrate which had not been reported earlier. The experimental results are discussed in chapter 3 and it mainly focused on surface modification of spray coated Cu_2O on Tantalum and electrochemically deposited Cu_2O on TCO (Transparent Conducting Oxide) due to vacuum anneal and low pressure oxygen exposure. The first PAES measurements on Cu_2O on Ta demonstrate the utility of PAES in the study of oxides surfaces. PAES and EAES measurements on vacuum annealed electrochemically deposited Cu_2O clearly showed that the masking effect of the C overlayer on Cu_2O/TCO and Cu. Top layer of Cu_2O is completely covered with carbonaceous layer and was substantially exposed after the thermal anneal process. To get better understanding of the powder and polycrystalline oxide samples, PAES measurements were performed on vacuum annealed thermally oxidized Cu(100) which are described in chapter 4. In comparison to the bulk oxide surfaces, the oxidized

Cu(100) surface also showed an increase in the Cu ($M_{2,3}VV$) Auger intensity with anneal temperature reaching a peak in Cu intensity at ~300 ^{0}C. The Cu Auger signal increased by more than a order of magnitude. Thermal anneal results on Cu_2O/ Ta at 300 ^{0}C for 13 minutes also shows the maximum intensity of Cu ($M_{2,3}$ VV) signal. These results reveal that surface becomes more metallic (reduction of Cu^+ to Cu^0) after annealing and positrons get trapped in vacancies surrounded by Cu atoms. However, further annealing of oxidized Cu(100) at higher temperature leads to decrease in Cu intensity possibly due to either oxygen diffusing from the Cu bulk to the surface or from Oxygen (or other impurity) desorbed from the inner chamber wall as a result of radiant heating by the sample. The experimentally derived annihilation probability of surface trapped positrons with the Cu 3p level (the level that gives rise to Cu($M_{2,3}$ VV) Auger emission) was found to be 2.74% which is close to the theoretical value which is 3.02% In addition to the PAES and EAES measurements on Cu_2O samples, PAES measurements on MgO , TiO_2 and metal on oxide surfaces were obtained. (See appendix B). This was the first application of PAES to study catalytically important oxide surfaces. Finally characterization of ultra thin overlayer can be done by combining PAES and EAES results and this information is useful in understanding the potential real-world catalytic materials.

5.2 Future work

The experimental studies presented on this dissertation have demonstrated that the sensitivity of PAES is the best analytical tool to study the top-most layer of oxide surface. Building a theoretical model is important to better understand the behavior of these oxides.

The surface morphology plays a key role in understanding the behavior of oxide surface during surface modification. The high surface sensitivity (<1 Å) of PAES can be combined with other techniques like Low Energy Electron Diffraction (LEED) and XPS to study surfaces. A high intensity positron beam can be used to study the oxidation state of the surface. We can monitor the growth process of the oxides and generate surfaces for specific needs. The resolution of TOF-PAES for high energy Auger electrons (> 100 eV) is low and should be improved. Hence another system with longer TOF tube is under construction. Mass spectrometer should be added to the system to study the desorbing species during annealing. The PAES measurements on electrochemically deposited Ni on TiO_2 and Pt on TiO_2 (which are important catalytic materials) under UV irradiation confirmed that positrons are a promising tool to study the charge transfer between metal nanoparticles and oxide surface. Further work needs to be done to understand charge transfer between metal nanoparticles on single crystal oxide surfaces.

APPENDIX A

SMOOTHING PROGRAM AND ALGORITHM

SMOOTHING PROGRAM

```
#include<stdio.h>
#include<stdlib.h>
#include<math.h>

//VARIABLE DECLARATION
int NO_OF_DATA = 2048;
float lifeTime;
int AVG_BACKGND_BEGIN = 1798;
int AVG_BACKGND_END = 1897;

float avgBackGnd;
float p1,p2,p3;
float * energy, * countRate, *countRateWOBkGnd, *NE;
int * channel, * count;
float sampleBias ;



//FUNCTION DECLARATION
void inputData(char * inputFile);
void movingAvg( char * output);
void calculateEnergyCountRate( );

int main(int argc, char ** argv)
 {

  int i, j;
  int n;

//INPUT PROMPT
  printf("\nEnter the Live Time: ");
  scanf("%f", &lifeTime);

  printf("\nEnter P1:");
  scanf("%f",&p1);

  printf("\nEnter P2: ");
  scanf("%f",&p2);

  printf("\nEnter P3: ");
  scanf("%f",&p3);

  printf("\nEnter Sample Bias: ");
  scanf("%f",&sampleBias);


//MEMORY ALLOCATION
  energy = (float * ) malloc (sizeof(float)*NO_OF_DATA);
```

```
  countRate = (float * ) malloc( sizeof(float)*NO_OF_DATA);
  countRateWOBkGnd = (float *)malloc(sizeof(float)*NO_OF_DATA);
  NE = (float *)malloc(sizeof(float)*NO_OF_DATA);
  channel = ( int * ) malloc( sizeof(int)*NO_OF_DATA);
  count = (int * )malloc(sizeof(float)*NO_OF_DATA);


  inputData( argv[1] );
  calculateEnergyCountRate();
  movingAvg( argv[2] );

  return 0;
 }

/* Reads data from the input file to arrays */

void inputData( char * inputFile)
 {
  int i;
  float temp;
  char garbage[50];
  FILE * fpr = fopen(inputFile, "r");
  for( i = 0; i < 2; i ++)
   fscanf( fpr, "%s", garbage);

  for( i = 0; i < NO_OF_DATA; i ++)
   {
    fscanf(fpr, "%d", &count[i]);
    fscanf(fpr, "%d", &channel[i]);
   }
  return;
 }


/*Performs calculations for energy, count rate,
    average Back Ground etc*/

void calculateEnergyCountRate( )
 {
  int i;
  float sum = 0;
  double d;
  float temp;
  FILE * fpw=fopen("input7.txt", "w");


//CALCULATE COUNT RATE
  for( i = 0; i < NO_OF_DATA; i ++)
   {
    countRate[i] = count[i] / lifeTime;
```

```
   }

//CALCULATE AVERAGE BACKGROUND
  for( i = 0;i <= NO_OF_DATA ; i ++)
   {
    if(( channel[i] >= AVG_BACKGND_BEGIN )
         &&(channel[i] <= AVG_BACKGND_END) )
     {
      sum += countRate[i];
     }
   }
  avgBackGnd = sum / (AVG_BACKGND_END-AVG_BACKGND_BEGIN+1);


//CALCULATE COUNTRATE W/O BACKGROUND
 for( i=0; i < NO_OF_DATA; i++)
  {
   countRateWOBkGnd[i] = countRate[i] - avgBackGnd;
  }


//CALCULATE NE

  for( i = 0; i < NO_OF_DATA; i ++)
   {

    temp = (p1-channel[i])*(p1-channel[i])*(p1-channel[i]);
    NE[i] = temp*countRateWOBkGnd[i]/(2*p2*p2);
   }


//CALCULATE ENERGY

  for(i = 0; i < NO_OF_DATA; i++)
   {
    temp = (p2/(channel[i]-p1));
    temp = temp * temp;
    energy[i] = temp + p3 + sampleBias;

    fprintf(fpw,"\n%e\t%e\t%e\t%d\t%d", energy[i], NE[i],
                    countRate[i], count[i], channel[i]);
   }

  return;
 }

/*Calculates moving average*/

void movingAvg( char * output)
 {
```

```
 int i,j;
 int  n;
 char garbage[20];
 int number;
 float currEnergy, upperLimit, lowerLimit;
 float totalEnergy, totalNE, averageEnergy=0, averageNE=0;
 float dE;
 float movingDiff;

 FILE *fpw = fopen( output, "w");

 printf("\nEnter the number of samples : ");
 scanf("%d",&n);
 printf("\nEnter the value for dE : ");
 scanf("%e",&dE);
 printf("\nEnter the upper Limit :");
 scanf("%e", &upperLimit);
 printf("\nEnter the lower limit :");
 scanf("%e", &lowerLimit);

 j = 0;
 i = 0;
while( ( energy[i] < upperLimit ))
 {
 j = i;
 totalNE = 0;
 averageNE = 0;
 number = 0;
 while( energy[j] < energy[i] + dE )
  {
   totalNE += NE[j];
   j ++;
   number ++;
  }

if( number != 0 )
 averageNE = totalNE/number;
 fprintf(fpw, "%e\t%e\t%d\n", energy[i], averageNE, number );
 i ++;

if( i >= n-1 )
 break;

 }
 return ;
}
```

Algorithm of the program

The program is based on the following flow chart.

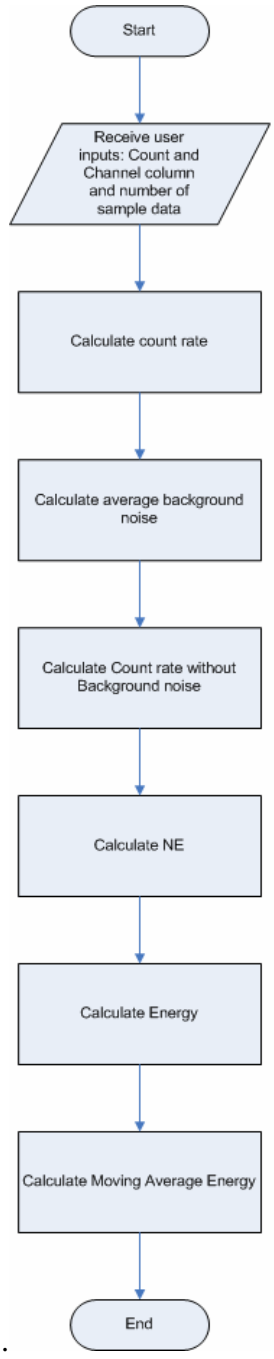

.

Each process of the process is explained in brief details.

1. Receive user inputs: Count and Channel column and number of sample data

The user provides the program with various inputs. The user provides the program with the Count data for every Channel received from the system.

2. Calculate count rate

The program calculates the count rate for data in each channel, using the formula:

$$countRate_i = count_i / lifetime$$

The pseudo code is quite obvious:

for each channel

count rate for that channel ← count of that channel / lifetime

3. Calculate average background noise

The formula for calculating the average background noise is:

$$avgBk_i = \sum_{i=1}^{n} countRate_i / R \quad , R = 1798 - 1897 + 1$$

We know that the data elicited from the channels 1798 to 1897 are noise. So we calculate the average background noise by finding the average count rate in those channels.

The pseudo code for doing so is:

for every count rates calculated in the channels 1798 to 1897

sum ← sum + count rate

average background noise ← sum / (1798 - 1897 + 1)

4. Calculate Count rate without background noise:

In this step the count rate for each channel is subtracted from the background noise.

The formula is:

$countRateWOBk_i = countRate_i - avgBk_i$

The pseudo code is:

for every channel

count rate without noise ← count rate - average background noise

5. Calculate NE:

The formula for calculating the NE is:

$NE_i = [P1 - channel_i)^3 * countRateWOBk_i]/[2*P2]^2$

P1 and P2 are parameters that are dependent of the samples used.

The pseudo code for doing so is:

for every channel

*NE ← ([P1 - channel)^3 * count rate without noise]/[2*P2]^2*

6. Calculate Energy:

The mathematical formulation is:

$E_i = [P2/(channel_i - P1)]^2 + P3 + sampleBias$

P1, P2 and P3 are parameters that are characteristic of the sample used.

SampleBias is user-provided information.

The pseudo code is:

for every channel i

Energy ← [P2/(channel$_i$ - P1)]^2 + P3 + sampleBias

7. Calculate Moving Average Energy:

Since this calculation is not straight forward as the previous ones, perhaps this could be better explained by another flowchart just to calculate that.

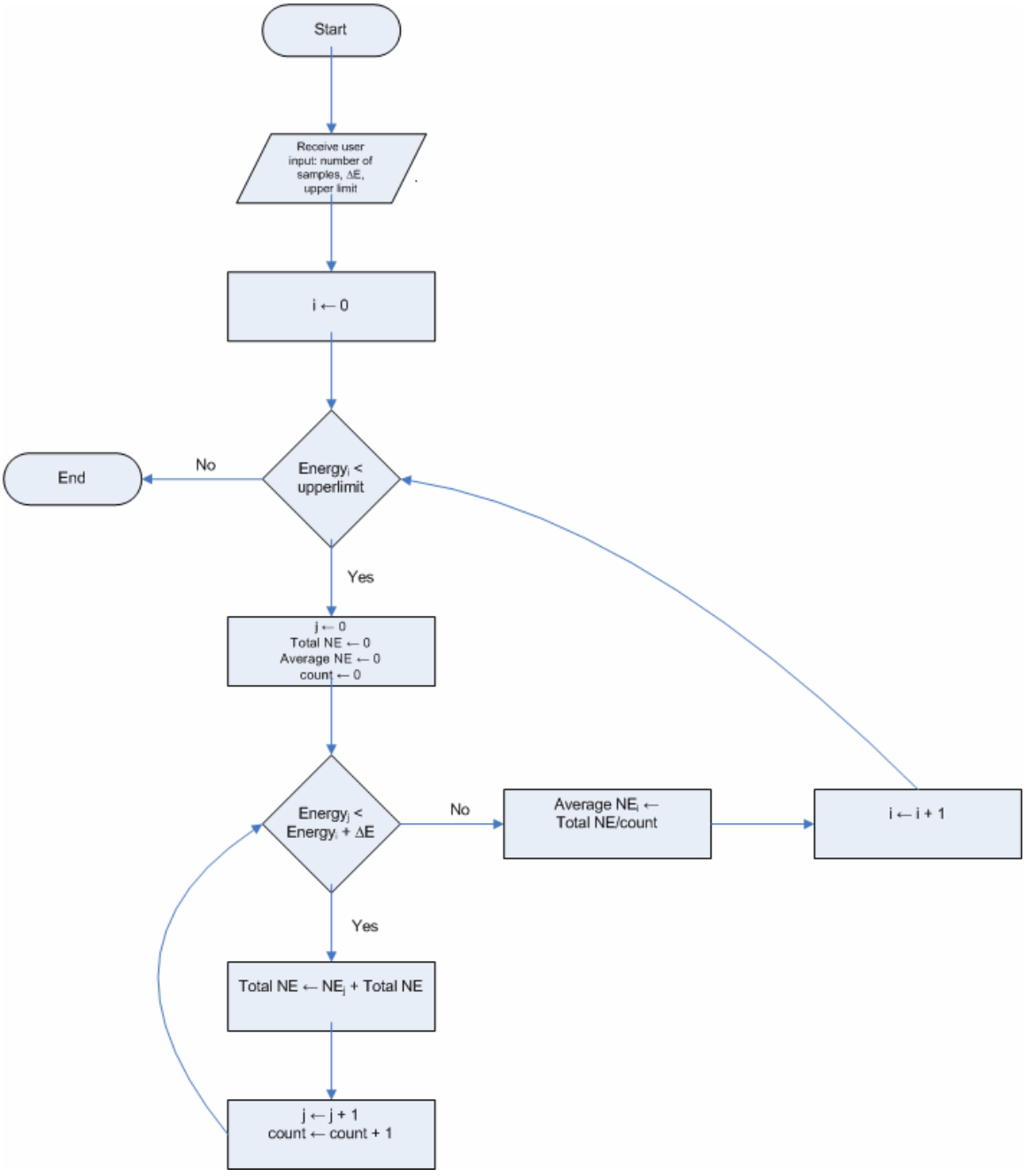

This operation involves, finding a set of channels for each channel in the data. The condition for a channel, C_j to belong to a set corresponding to the channel is that energy corresponding to channel C_j should not exceed the sum of energy corresponding to channel C_i and ΔE, where ΔE is a user defined parameter. The program has limited the channels to be considered by establishing an upper limit on the energy of the channels. This is because, the user may not be confident in the validity of the calculation if he/she uses the energy that exceeds a certain upper bound. The data from the channels with high channel numbers are found to be quite unreliable.

The pseudo code for the operation is:

receive user inputs: number of sample, ΔE, upper limit

i ← 0

for each channel i

while Energyi < upper limit

j ← i

total NE, frequency ← 0

for each channel j such that, $Energy_j < Energy_i + \Delta E$

total NE ← NE_j + total NE

frequency ← frequency + 1

average NE_i ← totalNE / count

APPENDIX B

TOF PAES SPECTRA OF MgO, TiO_2 AND METAL ON TiO_2

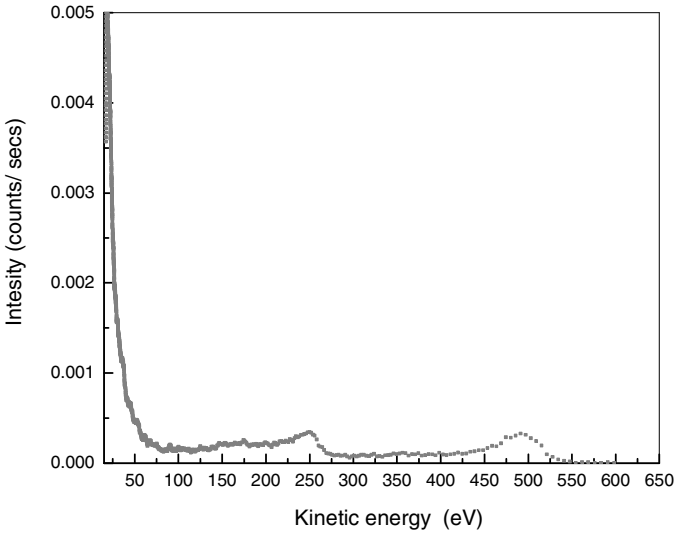

Figure B-1 TOF-PAES energy spectrum of pure Ti

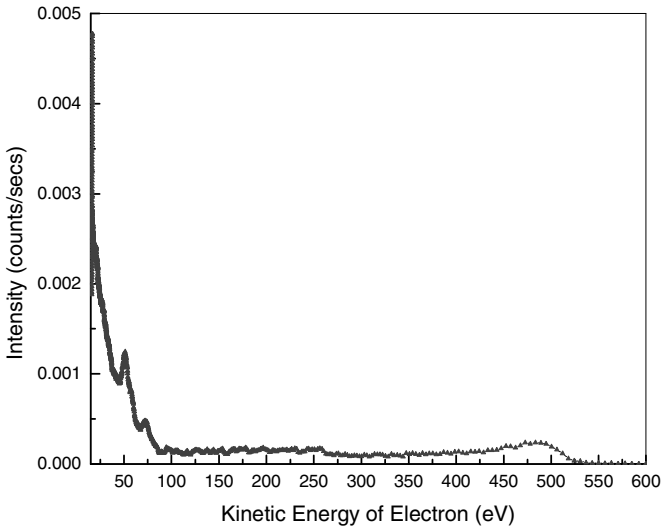

Figure B-2 TOF-PAES energy spectrum of TiO_2 on glass substrate.

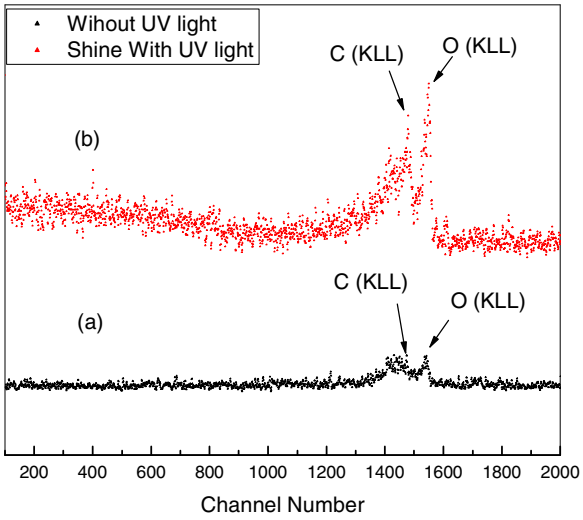

Figure B-3 TOF-PAES channel spectra of MgO (100) (a) without UV (b) under UV irradiation.

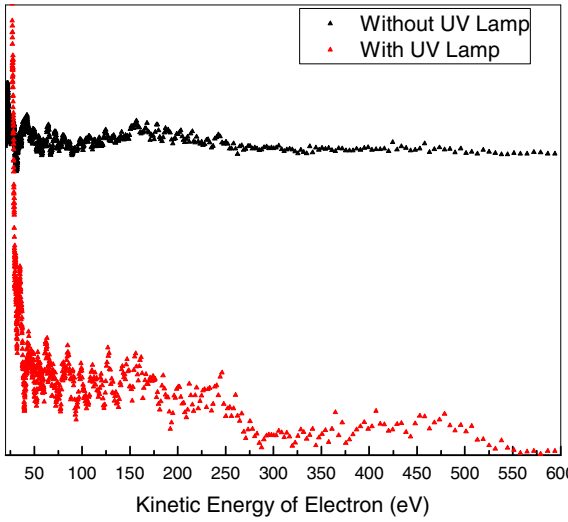

Figure B-4 TOF-PAES energy spectra of MgO (100) (a) without UV (b) under UV irradiation.

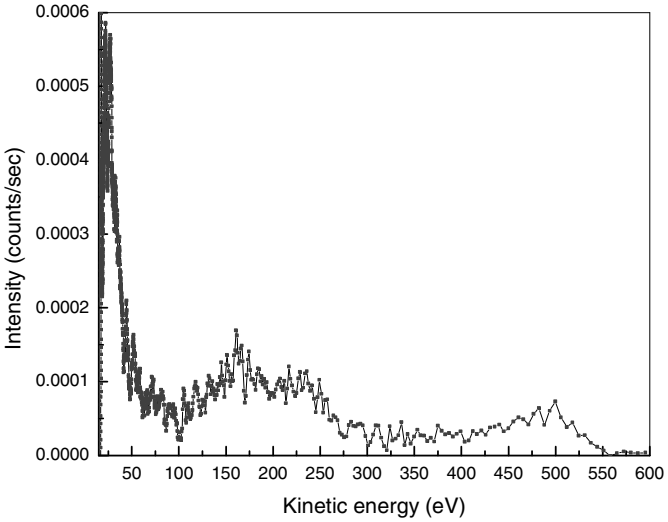

Figure B-5 TOF-PAES energy spectrum of TiO_2/Ta.

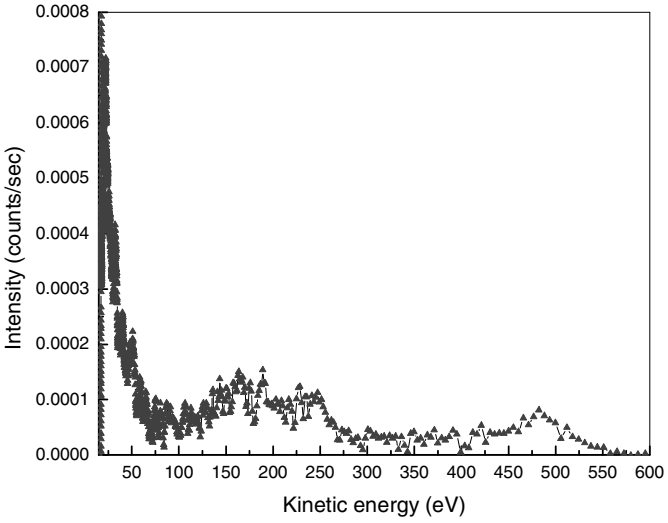

Figure B-6 TOF-PAES energy spectrum of TiO_2/Ta under UV irradiation.

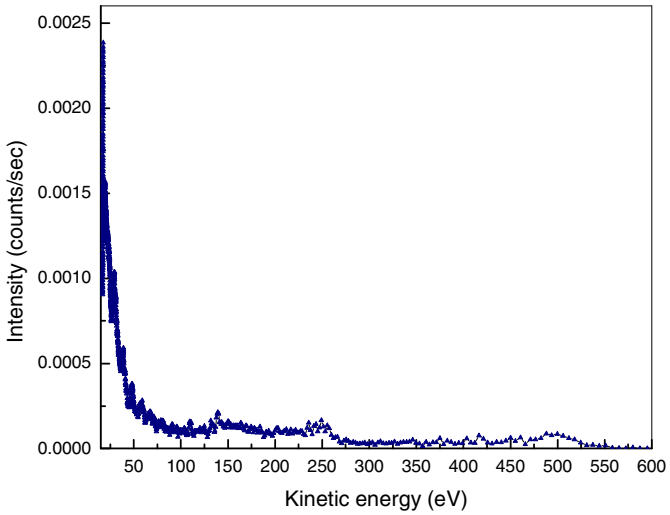

Figure B-7 TOF-PAES energy spectrum of Ni on TiO_2/Ta under UV irradiation.

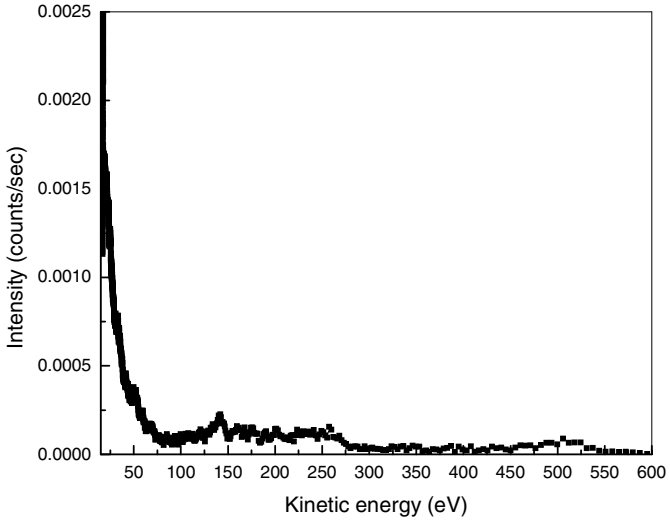

Figure B-8 TOF-PAES energy spectrum of Pt on TiO_2/Ta under UV irradiation.

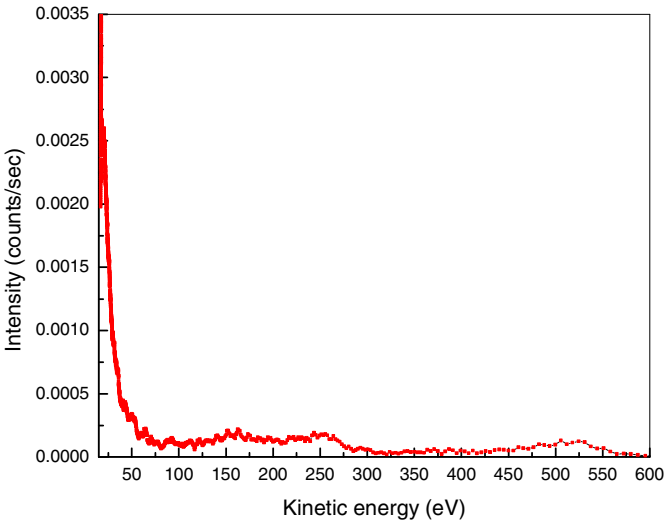

Figure B-9 TOF-PAES energy spectrum of pure Ta.

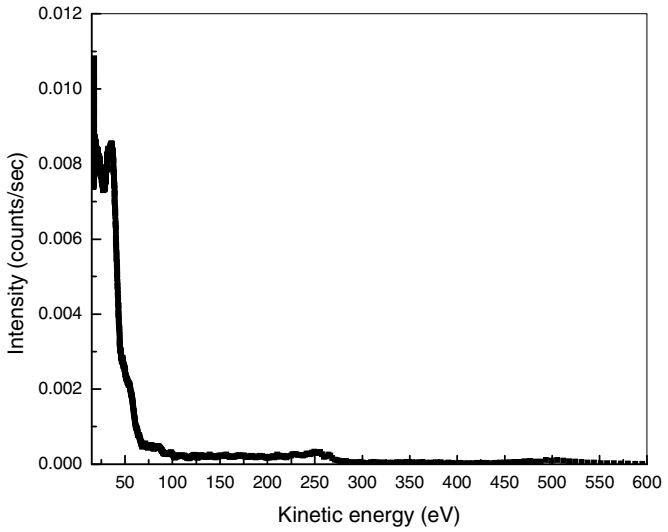

Figure B-10 TOF-PAES energy spectrum of pure Pt.

REFERENCES

(1) L. C. Olsen, R. C. Bohara, M. W. Urie, *Appl. Phys. Lett.* **1979**, *34*, 47.

(2) L. Papadimtriou, N. A. Economou, D. Trivich, *Solar Cells* **1981**, *3*, 73.

(3) J. Heriou, E. A. Niekisch, G. Scharl, *Solar Energy Mater.* **1980**, *4*, 101.

(4) A. E. Rakhshani, *Solid-State Electron.* **1986**, *29*, 7.

(5) B. P. Rai, *Solar Cells* **1988**, *25*, 265.

(6) R. N. Briskman, *Solar Energy Mater. Solar Cells* **1992**, *27*, 361.

(7) A. O. Musa, T. Akomolafe, M. J. Carter, *Solar Energy Mater. Solar Cells* **1998**, *51*, 305.

(8) A. H. MacDonald, *Nature* **2001**, *414*, 409.

(9) W. Wang, O. K. Varghese, C. Ruan, M. Paulose, C. A. Grimes, *J. Mater. Res.* **2003**, *18*, 2756.

(10) K. Mizuno, M. Izaki, K. Murase, T. Shinagawa, M. Chigane, M, M. Inaba, A. Tasaka, Y. Awakura, *J. Electrochem. Soc.* **2005,** *152,* C179.

(11) M. Hara, T. Kondo, M. Komoda,, S. Ikeda, K. Shinohara, A. Tanaka, N. J. Kondo, K. Domen, *Chem. Commun.* **1998**, 357.

(12) P. E. Jongh, D. Vanmaekelbergh, J. J. Kelly, *Chem. Commun*. **1999**, 1069.

(13) G. P. Pollack, D. Trivich, *J. Appl. Phys*. **1975**, 46, 163

(14) P. D. Kirsch, J.G.Ekerdt, *J. Appl. Phy*s. **2001**, 90, 425

(15) S. Poulston, P. M. Parlett, P. Sotne, M. Bowker, *Surf. Interface Anal.***1996,** 38, 811.

(17) P. Coleman, *Positron Beams and their applications*, World Scientific Publishing Co. Pte. Ltd., **2000.**

(18) C. D. Anderson, *Phys. Rev.* **1932**, 41, 405.

(19) P. J. Schultz, K. G. Lynn, *Rev. Mod. Phys.* **1988**, 60, 701

(20) A. B. Walker, K. O. Jensen, J. Szymanski J, D. Neilson, *Phys. Rev. B.* **1992**, 46, 3 1687.

(21) A. Weiss, D. Mehl, A. R. Koymen, K. H. Lee, C. Lei, *J. Vac. Sci. Technol. A*. **1990**, *8*, 2517.

(22) A. R. Koymen, K. H. Lee, D. Mehl, A. Weiss, K. O. Jensen, *Physical Rev. Lett*. **1992**, *68*, 2378.

(23) J. G. Zhu, M. P. Nadesalingam, A. H. Weiss, M. Tao, *J. App. Phys*. **2005**, *97*, 103510.

(24) D. Mehl, A. R. Koymen, K. O. Jensen, F. Gotwald, A. Weiss, *Physical Rev. B*. **1990**, *41*, 799.

(25) C. H. Hodge, M. J. Stott, *Solid State Com.* **1973**, 12, 1153.

(26) R. M. Niemanen, M.J. Pushka, *Rev. Mod. Phys*. **1994**, 66, 841.

(27) N. G. Fazleev, J. L. Fry, A. H. Weiss, *Rad. Phys. Chem*. **2000**, 58, 2000.

(28) N. G. Fazleev, J. L. Fry, K. H. Kuttler, A. R. Koymen, A. H. Weiss, *Phys. Rev. B* **1995**, 52, 5371.

(29) N. G. Fazleev, *Appl. Surf. Sci.* **2006**, 252, 3333.

(30) A. P. Mills, *Solid. State Comm*. **1979**, 31, 623.

(31) X. Shuping, *Dissertation* **2002**.

(32) Dupont Na-22 source report, **1990**.

(33) J. E. Martin, *Physics for Radiation Protection*, John Wiley and Sons N.Y. **2000.**

(34) M. Laval M, M. Moszynski, R. Allemand, E. Cormoreche, P. Guinet, R. Odru, J. Vacher, *Nuclear Instruments and Methods*, **1983**,206, 169.

(35) E. Dafni, *Nuclear instruments in Physics Research A* **1987**, 254, 54.

(36) W. L. Josheph, *Nuclear instruments and methods* **1979**,162, 587.

(37) P. Kruit, F. H. Read, *J. Phys. E: Sci Instrum.* **1983**, 16, 313.

(38) G. A. Harrower, *Phys Rev*, **1956**, 102, 340.

(39) T. Koshikawa, R. Shimizu, *J. Phys. D: Appl. Phys*. **1973**, 6, 1369.

(40) G. Zhou, Dissertation **2003**.

(41) W. Siripala, A. Ivanovskaya, T. F. Jaramillo, S. H. Baeck, E. W. McFarland, *Solar Energy Mater. Solar Cells* **2003**, *77*, 229.

(42) J. Katayama, K. Ito, M. Matsuoka, J. Tamaki, *J. Appl. Electrochem.* **2004**, *34*, 687.

(43) J. Oh, Y. Tak, J. Lee, *Electrochem. Solid-State Lett.* **2005**, *8*, C81.

(44) I. Lyubinetsky, S. Thevuthasan, D. E. McCready, A. S. Lea, D. R. Baer, *Nanotechnology*; **2003**, Vol 2, 667.

(45) A. E. Rakhshani, J. Varghese, *J. Mater. Sci.* **1988**, *23*, 3847.

(46) A. E. Rakhshani, J. Varghese, *Solar Energy Mater.* **1987**, *15*, 237.

(47) A. K. Mukhopadhyay, A. K. Chakraborty, A. P. Chatterjee, S. K. Lahiri, *Thin Solid Films* **1992**, *209*, 92.

(48) Y. Zhou, J. A. Switzer, *Mater. Res. Innovations* **1998**, *2*, 1731.

(49) Y. Zhou, J. A. Switzer, *Scr. Mater.* **1998**, *38*, 1731.

(50) V. Georgieva, M. Ristov, *Solar Energy Mater. Solar Cells* **2002**, *73*, 67.

(51) K. Nakaoka, J. Ueyama, K. Ogura, *J. Elerctrochem. Soc.* **2004**, *151*, C661.

(52) J. Oh, Y. Tak, J. Lee, *Electrochem. Solid-State Lett.* **2004**, *7*, C27.

(53) J. Morales, L. Sánchez, S. Bijani, L. Martínez, M. Gabas, J. R. Ramos-Barrado, *Electrochem. Solid-State Lett.* **2005**, *8*, A159.

(54) F. Oba, F. Ernst, Y. Yu, R. Liu, H. M. Kothari, J. A. Switzer, *J. Am. Ceram. Soc.* **2005**, *88*, 253.

(55) L. C. Wang, N. R. de Tacconi, C. R. Chenthamarakshan, K. Rajeshwar, M. Tao, *Thin Solid Films* **2007,** 515, 3090.

(56) V. F. Drobny, L. L. Pulfrey, *Thin Solid Films* **1979**, *61*, 89.

(57) G. Beensh-Marchwicka, L. Krol-Stepniewska, M. Slaby, *Thin Solid Films* **1982**, *88*, 33.

(58) E. D. Lawrence, N. C. Macknonald, P. W. Palmberg, G. E. Riach, R. E. Weber, *Handbook of Auger Electron Spectroscopy*, Perkin-Elmer Corporation: Eden Prairie, Minnesota, 1976.

(59) D. Briggs, M. P. Seah, *Practical Surface Analysis;* Wiley: New York, **1990**, 1, 183-186.

(60) K. H. Schulz, D. F. Cox, *Phys. Rev. B* **1991**, *43*, 1610.

(61) P. D. Kirch, J. G. Ekerdt, *J. of App. Phys*. **2001**, 90, 4256.

(62) T. Kangas, K. Laasonen, A. Puisto, H. Pitkanen, M. Alatalo, *Surf. Sci.* **2005**, 584, 62.

(63) A. Soon. M. Todorova, B. Delley, C. Stampfl, *Phys. Rev. B* **2006**, 73, 165424.

(64) A. Soon, M. Todorova, B. Delley, C. Stampfl, *Phys. Rev. B* **2007**, 75,125420.

(65) A. Chen, C. Lu, Z. Chen, Y. Li, J. Li, Chinese *J. of Chem. Phys*. **2006**,19, 54.

(66) E. Ruiz, S. Alvarez, P. Alemany, R. Evarestov, *Phys. Rev. B* **1997**, 56, 12, 7189.

(67) A. Atkinson, *Rev. Mod. Phys*. **1985**, 5, 2, 437.

(68) J. C. Yang, M. Yeadon, B. Kolasa, J. M. Gibson, *Scripta Mat.* **1998**, 38, 8, 1237.

(69) M. W. A. Johnson, K. F. Mehl, *Trans. Am. Inst. Min. Metal Pet. Eng.* **1939**, 135 416.

(70) J. C. Yang, D. Evan, L. Tropia, *Appl. Phys. Lett*. **2002**, 81, 2, 241

(71) G. Honjo, *Soc Of Japan Jour.* **1949**, 4, 330.

(72) G. Zhou, J. C. Yang, *Appl. Surf. Sci*. **2004**, 222, 357.

(73) A. P. Mills, *Solid. State Comm.* **1979**, 31, 623.

(74) D. C. Joy, Y. Lin, *Surf. Interface Anal.* **2005**, 37**,** 895.

(75) K. Jensen, A. H. Weiss, *Phys. Rev. B* **1990**, 41, 3928.

BIOGRAPHICAL INFORMATION

The author of this dissertation was born in Tangalle, Sri Lanka. She received a Bachelor of Science (Hons.) in Physics at the University of Kelaniya, Sri Lanka in 1998. Then she worked in the same department as an Assistant Lecturer for nearly one year before moving to USA for higher education.

Manori joined the University of Texas at Arlington in fall 2000 to complete M. S. in Physics. She joined positron surface group in 2001 and completed M. S. in Physics in 2003. Her thesis title was "study of positron trapping at quantum-dot like Cu particles on the surface of Fe using positron annihilation induced Auger electron spectroscopy. She started Ph. D. in Physics in June 2003 and completed her Ph. D. in applied physics in May 2007.